SELECTIVE ELECTRO-MAGNETIC ABSORBERS BASED ON
METAL-DIELECTRIC-METAL THIN-FILM CAVITIES

by

JANARDAN NATH
M. S. University of Central Florida, 2011

A dissertation submitted in partial fulfilment of the requirements
for the degree of Doctor of Philosophy
in the Department of Physics
in the College of Sciences
at the University of Central Florida
Orlando, Florida

Summer Term
2015

Major Professor: Robert E. Peale

ABSTRACT

Efficient absorption of light is required for a large number of applications such as thermo-photovoltaics, thermal imaging, bio-sensing, thermal emitters, astronomy, and stealth technology. Strong light absorbers found in nature with high intrinsic losses such as carbon black, metal-black, and carbon nano-tubes etc. are bulky, not design-tunable and are hard to pattern for micro- and nano- devices. We developed thin-film, high performance absorbers in the visible, near-, mid-, long-wave - and far-IR region based on a 3 layer metal-dielectric-metal (MDM) structure.

We fabricated a 3-layer MDM absorber with large band-widths in the visible and near IR spectral range without any lithographic patterning. This was the first demonstration in the optical range of the *Salisbury Screen*, which was originally invented for radar absorption. A Fabry-Perot cavity model depending on the thickness of the dielectric, but also the effective permittivity of the semi-transparent top metal gives calculated spectra that agree well with experiment.

Secondly, we fabricated long-wave IR and far-IR MDM absorbers comprising surface patterns of periodic metal squares on the dielectric layer. Strong absorption in multiple bands were obtained, and these depended weakly on polarization and angle of incidence. Though such absorbers had been extensively studied by electrodynamic simulations and experiment in the visible to far- R regions, there existed no analytic model that could accurately predict the wavelengths of the multiple resonances. We developed a theoretical model for these absorbers based on standing-wave resonances, which accurately predicts resonance wavelengths for experiment and simulation for the first time. Unlike metamaterial theories our model does not depend on the periodicity of the squares but only on their lateral dimension and the thickness of the dielectric. This feature is confirmed by synchrotron-based IR spectral imaging microscopy of single isolated squares.

I dedicate this work to my parents, my sisters, my nephew and my wife.

ACKNOWLEDGMENTS

First of all I acknowledge my supervisor Prof. Robert Peale for accepting me in his group and supporting me through out my PhD. He has given me a lot of freedom with my research. He believed in my ideas and guided me with valuable suggestions. He worked hard in funding me and my lab mates. He has maintained a wonderful environment in the lab by being kind and patient. I thank Prof. Robert Peale for his wonderful advising in my PhD.

I would like to thank my committee Dr. Masahiro Ishigami, Prof. Leonid Chernyak, and Prof. Konstantin L. Vodopyanov for accepting to help and guide me for my dissertation.

I acknowledge my lab-mates for their support, love and inspiration. Especially, I thank Mr. Farnood Rezaie, Dr. Deep Panjwani, Dr. Monas Shahzad, Mr. Pedro Figueiredo, Dr. Gautam Medhi, Mr. Imen Razadad, Ms. Javaneh Boroumand, Mr. Evan Smith, and Dr. Tatyana Brusentsova for their help with various projects. I thank Mr. Sushrut Modak for always helping me with FDTD simulations. I thank Dr. Ryuichi Tsuchikawa for assistance with the AFM measurements. I am very grateful to Mr. Douglas Maukonen for his help with the spectroscopic measurements. I thank Dr. Walter R Buchwald, Dr. Justin Cleary, Dr. Nima Nader, Dr. Josh Hendrickson and Dr. Kurt G. Eyink of Air Force Research Laboratory, Dayton for helping us with various experiments. I would like to thank Prof. Leonid Chernyak, Dr. Elena Flitsiyan and Dr. Casey Schwarz for the help with the cathodoluminescence experiments.

I thank Dr. Mehmet Yeslitas for the measurements with synchrotron microscopy. I thank Mr. Chris Fedrickson, Dr. Isaiah Oladeji, Dr. A. V. Muravjov and Mr. Guy Zummo for the help and guidance with different instruments. I would also like to thank Physics department faculty members and office staff, who helped me through out my academic program.

TABLE OF CONTENTS

LIST OF FIGURES

LIST OF TABLES

CHAPTER 1: INTRODUCTION

Absorption of light or electro-magnetic (EM) radiation is highly desired for several applications. Light is a form of energy. The energy of light is quantized and each quantum is called a photon. The energy of a photon is given by $E = h\nu$, where h and ν are Planck's constant and frequency of light, respectively. The photon-energy in taken up by the absorber in the form of electronic-excitations and eventually transformed into thermal energy. Efficient absorbption of light is essential for several applications such as solar photovoltaics [1, 2] and thermovoltaics [3, 4], thermal imaging [5, 6], radar-absorbent material (RAM) used in stealth technology [7, 8], sensing [9, 10], and IR emitters [11, 12]. Strong light absorbers found in nature with high intrinsic losses such as carbon black, metal-black, and carbon nano-tubes etc. are bulky, and are hard to pattern for micro- and nano- devices. Also, their applications are limited because of lack of tunability [13]. In lower wavelength regions of EM spectrum, (long-wave-IR and terahertz (THz)) there is no effiecient EM absorber materials. Especially, imaging in terahertz is tricky because of lack of easily accessible electromagnetic responses from naturally occurring materials. Therefore, there is a great demand for thin-film, high performance absorbers for advanced micro/nano level detectors and sensors.

The attenuation of light in an absorbing medium is related to the thickness and attenuation constant, α of the medium according to Beer Lambart's law is given by,

$$T = e^{-\alpha t}, \tag{1.1}$$

where T is the normalized transmission, and t is the thickness of the medium, and $\alpha = 4\pi\kappa/\lambda_0$, where κ is the imaginary part of the refractive index of the absorbing medium and λ_0 is the free space wavelength of light. To find the absorption in the medium it is important to know the re-

flection of light from the surface of the medium. Reflectance of light from a absorbing medium of complex refractive index $\tilde{n}_2 = n_2 + ik_2$ on normal incidence from another medium $\tilde{n}_1 = n_1 + ik_1$ is given by Freshnel's law,

$$R = \left| \frac{\tilde{n}_1 - \tilde{n}_2}{\tilde{n}_1 + \tilde{n}_2} \right|^2 \tag{1.2}$$

Thus, normalized absorption or absorptance from a medium is given by,

$$A = 1 - R - T, \tag{1.3}$$

assuming that scattering is negligible for the medium. Eq.(1.3) shows that it is important to reduce reflection to achieve perfect absorption. Eq.(1.1) suggests that, for a material, the higher the extinction coefficient (k), the higher the absorption. But, at the same time, higher value of κ increases the Freshnel's reflection(Eq.1.2) which reduces the absorption of light.

1.1   Plasmonic Absorbers

Absorption of light involves excitation of electrons to higher energy states. Metals have large number of free electrons, and hence, can be highly lossy. In normal conditions (e.q. simple case of incidence from a smooth surface), absorption of metal is limited by it's high reflectance (Eq.(1.3)). In 1902, Wood reported the anomalous dips in the reflectance spectra of metallic gratings under illumination of visible light [14]. It was demonstrated later that such absorptions are mainly due to excitation of surface plasmon polaritons (SPP). SPPs are coherent delocalized electron oscillations on the interface of a dielectric and a metal which travel along the interface. The dispersion relation of SPP is given by [15],

$$k_{SPP} = k_0\sqrt{\frac{\varepsilon_d\varepsilon_m}{\varepsilon_d + \varepsilon_m}}, \tag{1.4}$$

where $k_0 = 2\pi/\lambda_0$ is the free space wave-vector of light, ε_d and ε_m are dielectric permittivity of the dielectric and the metal, respectively. Absorbed energy in this case dissipates into heat if otherwise channeled-out or out-coupled. SPPs cannot be excited directly by incidence of light; it requires a prism, or a grating. In case of excitation by gratings, wavelength of absorption depends on the period of the gratings and angle of incidence [15] as given by,

$$k_{SPP} = k_0 sin\theta \pm m\frac{2\pi}{a}, m = 1, 2, 3.. \tag{1.5}$$

, where θ is the angle of incidence and a is the period of gratings. One can show that, such modes can only be excited in case of TM polarization [16]. Periodic plasmonic structures show sharp and strong resonance absorption because of excitation of SPP modes and has been widely studied both theoretically and experimentally in metallic gratings [17–21]. But the problem with these absorbers is that they are highly sensitive to angle of incidence and highly polarization dependent(Eq.1.5).

1.2 Fabry-Perot Type Absorbers

In 1952, W. W. Salisbury invented a triple-layer structure composed of conductor-dielectric-conductor at radio wavelengths which absorbs EM radiation in multiple bands [22]. Also known as *Salisbury Screen*, it has been used to reduce radar cross-sections for military applications [22, 23]. The resonant absorption in such absorber occurs in multiple bands because of light trapping in the Fabry-Perot cavity formed in the conductor-dielectric-conductor structure. The resonance wavelength depends on the thicknesses of the dielectric spacer. The condition of destructive interference of light from the top and the bottom conductor gives rise to zero reflection. This is the same con-

dition as for resonant light trapping with multiple reflections inside the dielectric of a Fabry-Perot cavity. The trapped energy is consumed by losses in the three media, where the dissipated energy density is proportional to the frequency, to the imaginary part of the permittivity, and to the square of the amplitude of the electric field [24]. For such structures, the fundamental absorption band occurs at $\lambda = 4nt$, where n and t are the refractive index and the thickness of the dielectric, respectively. This mechanism has been investigated theoretially by Shu et. al. in the visible and near-IR regions [25]. However, the absorption band obtained by this mechanism is angle dependent and structures are limited to a minimal thickness of one-quarter wavelength.

1.3   Metamaterial Absorbers

Artificially engineered materials or metamaterials have exotic properties not yet been found in nature [26–29]. A repeating patterns of conducting structures of sub-wavelength size can act as an effective medium with effective permittivity, ε_{eff} and effective permeability, μ_{eff} not seen in ordinary materials. In conventional materials, material properties derive from their constituent atoms. Metamaterials acquire it's properties from their constituent units. Structure size, geometry and periodicity mainly determines the properties of the metamaterials.

One of the most interesting of such material is negative index metamaterials (NIM) [26, 28–30]. NIMs have potential use in creation of superlens which can significantly improve the optical resolution beyond diffraction limit [31]. The idea of negative refractive index, $-n$ was first introduced in 1968 by Victor Veselago with simultaneous negative values of permittivity, ε and permeability, μ [26]. He showed that if ε and μ are negative simultaneously, Maxwell's equations forces us to choose a negative square root for n,

$$n = -\sqrt{\mu\varepsilon}, \qquad \varepsilon < 0, \mu < 0. \tag{1.6}$$

In metals, $\text{Real}(\varepsilon) < 0$. It was shown that the effective permittivity can be obtained in the form of Drude model in arrays of wires in much lower frequency regions than the plasma frequency of the metal as [29, 32, 33],

$$\varepsilon(\omega) = 1 - \frac{\omega_{ep}^2 - \omega_{e0}^2}{\omega^2 - \omega_{e0}^2 + i\gamma_{e0}\omega}, \tag{1.7}$$

where ω_{ep} is the electric plasma frequency, ω_{e0} is the restoring or binding frequency and γ is the damping constant. In 2000 Smith *et al.*, experimentally demonstrated that it is possible to obtain negative effective permeability [28] in artificially structures materials. Periodic split ring resonator (SRR) structures much smaller than the wavelength was used to achieve negative μ_{eff}. Similar to the dielectric permitivity in metals, effective magnetic permeability can be obtained in form of Drude model [28, 29, 33],

$$\mu(\omega) = 1 - \frac{\omega_{mp}^2 - \omega_{m0}^2}{\omega^2 - \omega_{m0}^2 + i\gamma_{m0}\omega}, \tag{1.8}$$

where ω_{mp} is the magnetic plasma frequency, ω_{m0} is the restoring or binding frequency and γ is the damping constant. By carefully choosing periodic structure parameters it is possible to achieve simultaneous negative permittivity and permeability for metamaterials to give negative refractive index [28]. Currently, metamaterial is a very popular topic of research for potentail use in diverse applications including antenas [34], absorbers [35], cloaking devices [36, 37], superlens [31], spoof plasmons [38, 39], and with many more to be surely discovered in the future.

Metamaterials are lossy because of the complex permittivity and permeability. This lossy nature of metamaterial has been exploited to achieve near perfect absorption. Landy *et al.*, in 2008 demonstrated that by tailoring independent electric and magnetic response in engineered materials, perfect absorption can be achieved [35]. In their work, periodic arrays of ring resonators and cut wires were used to achieve an effective medium characterized by $\tilde{\varepsilon} = \varepsilon' + i\varepsilon''$ and $\tilde{\mu} = \mu' + i\mu''$ so that perfect absorption can be achieved when relative impedance, $z = \sqrt{\mu/\varepsilon}$ is equal to unity (free space impedance). By this mechanism of impedance matching it is possible to obtain zero reflection which is not easily achieved with naturally occuring materials. These type of absorbers are commonly called as metamaterial perfect absorbers (MPA). Motivated by work of Landy *et al.*, MPAs were demonstrated with up to 99% absorption in the UV [40], visible [33], near-IR [9, 41, 42], mid-IR [11, 12, 43], LWIR [40], terahertz [5, 35, 44] and gigahertz frequencies [45, 46]. One of the most interesting characteristics of metamaterial absorber is that it is much thinner than the resonance wavelength. For example, MPAs have been shown as thin as $\lambda/40$ [45], $\lambda/67$ [43] and $\lambda/69$ [46]. Polarization independent and wide-angle absorption bands are achieved for such absorbers [9, 11, 33, 41, 42]. Such properties make metamaterial absorbers useful for many applications such as solar photovoltaics [1, 2] and thermovoltaics [3, 4], thermal imaging [5, 6], radar-absorbent material (RAM) used in stealth technology [7, 8], sensing [9, 10], and IR emitters [11, 12].
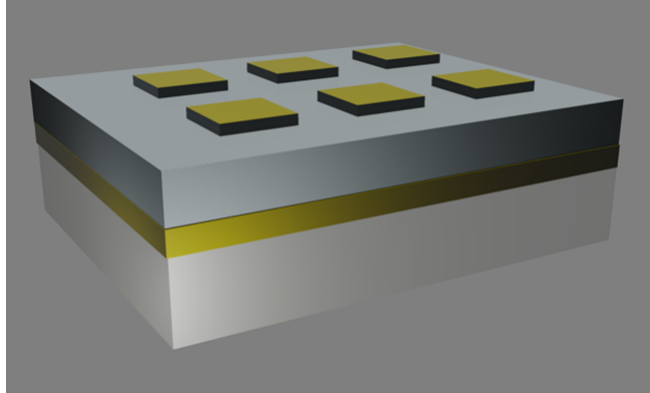
Figure 1.1: Metamaterial absorber with FSS of periodic squares of metal at the top, a dielectric spacer in the middle and a optically thick metal ground plane on a Si or glass substrate.

MPAs typically consists of 3 layers which are a frequency selective surface (FSS) of periodic sub-wavelength structues made of metal on the top, a dielectric spacer in the middle and a metallic ground plane on a suitable substrate. MPAs can be divided in to two categories on basis of FSS structures; 1) MPA with FSS of split ring resonators (SRR), and 2) MPA with FSS of squares/rectangles/circles. FSS of MPA with SRR has been popular mainly in the gigahertz(GHz) and terahertz (THz) range. However, in the visible, near- and far-IR, fabrication of SRR structures by lithography becomes difficult. Hence, simpler FSS structures like period squares/rectangles/circles have been adopted in higher frequency regions. Fig.1.3 shows a MPA with FSS of periodic squares.

1.4 Motivation

One of the main objective of our research is fabrication of CMOS compatible absorbers which can be used for applications such as uncooled thermal detectors. Uncooled thermal detectors sense

heat in form of change in resistivity (bolometric detector) or electric polarization (pyroelectric detector) of the detector element because of heat induced by radiation. Since, MPAs strongly absorp radiation, sensitivity of such detectors can be greatly improved by using MPA as coating for the detector elements.

Uncooled infrared detectors have recently gained wide attention for infrared imaging application, due to their several advantages such as low costs of fabrication, low weight, low power consumption, extended spectral response, and long-lasting operating capacity [47–49]. Microbolometers are most extensively used in uncooled infrared detectors because of their CMOS compatible processing. They are easy to be monolithically integrated with CMOS circuitry which has advantage of lower manufacturing costs. Thus, for using MPAs as the coating for such detector, it has to be CMOS compatible. Since, time constant of a thermal camera is greatly effected by the thermal mass of the detector element, the absorber needs to be thin.

MPAs absorb radiation on basis of resonance which typically has bandwidth less than 12% of the center frequency [50]. For extended spectral response for thermal detectors wide-band absorption is required. Although thin MPAs are demonstrated with strong absorption, success in experimental realization of wide-band absorption is not significant.

We work on developement of a CMOS compatible highly efficient thin absorbers in the near-, long-wave- and far-IR (THz) region which produce wide-band, polarization and angle independent absorption bands.

It is found that the physics of MPA is much challenging as it involves sub-wavelength structures. Although effective medium theory of MPA based on magnetic resonances is commonly known in the scientific community, alternative theories exist such as interference theory and planar wave-guide model which deny magnetic resonances. On the other hand, most of the theoretical work in MPA is based on numerical simulations [5, 11, 35, 44, 51, 52]. There is hardy any report

8

with analytical theory to calculate dependence of resonance on size, periodicity of FSS or thickness of dielectric spacer. We work on development of an analytical model of such absorbers to quantitatively calculate resonance characteristics such as resonance wavelengths and line-shapes for the absorption bands.

CHAPTER 2: THEORETICAL BACKGROUND

In this chapter, we briefly present theories involved in our work. We discuss different models of effective medium theory such as Maxwell-Garnett approach and Bruggeman approach. Bruggeman approach is used in our work for calculation of effective dielectric permittivity of discontinuous nano-structured gold thin films. Since we work on development of a theoretical model to explain absorption mechanism of metamaterial absorbers, we also discuss here some of the existing models of such absorbption. Since geometrical optics does not work well for sub-wavelength structures, computational electrodynamics is used widely. Finite difference time domain (FDTD) method is commonly used for study of electrodynamics of metamaterial absorbers. FDTD simulations are performed in our work using commercially available software FDTD Solutions 8.9 - Lumerical Solutions, Inc. We also briefly discuss the basic principles of FDTD method in this chapter.

2.1   Effective Medium Theory

Effective medium theory (EMT) (or effective medium approximation (EMA)) is the theory to find macroscopic properties of a mixture of materials. A composite medium can be considered to be homogeneous when the observation scale is sufficiently large (homogeneity is much smaller than the wavelength of light). EMT calculates macroscopic behavior such as conductivity, permittivity, and permeability of heterogeneous materials (composites) from the information of the properties of each medium composing the mixture as well as proportions, and shapes. Maxwell-Garnett (MG) [53] and Bruggeman theory [54, 55] are two widely used effective medium formalisms for calculating effective permittivity. Below we discus derivation of both the models starting with a first order approximation using classical Clausius-Mossotti eqaution.

2.1.1 2-Phase Media

A first order approximation of effective permittivity for a two component medium can be derived from classical Clausius-Mossotti equation. Clausius-Mossotti equation describes the dielctic constant of an isotropic and homogenous medium as,

$$\frac{\varepsilon(\omega) - 1}{\varepsilon(\omega) + 2} = \frac{4\pi}{3} N\alpha(\omega), \tag{2.1}$$

where $\alpha(\omega)$ is the polarizability and N is the number of dipoles per unit volume of a single microscopic constituent. For a two phase medium with polarizabilities (α_a, α_b) and volume dipole densities, (N_a, N_b) the effective dielectric constant can be derived from eq.(2.1) as,

$$\frac{\varepsilon_{eff}(\omega) - 1}{\varepsilon_{eff}(\omega) + 2} = \frac{4\pi}{3}[N_a\alpha_a(\omega) + N_b\alpha_b(\omega)] \tag{2.2}$$

Now, using eq.(2.1) in eq.(2.2), we get the effective medium of a two component system given by,

$$\frac{\varepsilon_{eff}(\omega) - 1}{\varepsilon_{eff}(\omega) + 2} = f_a\frac{\varepsilon_a(\omega) - 1}{\varepsilon_a(\omega) + 2} + f_b\frac{\varepsilon_b(\omega) - 1}{\varepsilon_b(\omega) + 2}, \tag{2.3}$$

where $f_i = N_i/(N_a + N_b)$ denotes the volume fraction of ith component. Eq.(2.3) can be used to calculate effective permittivity of a composite medium of nano-structured material.
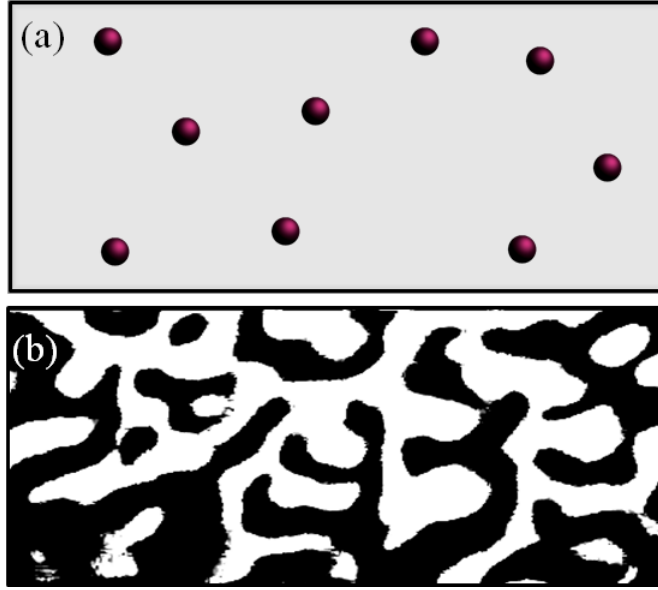
Figure 2.1: Schematic diagrams of 2-pahse (a) dilute system of spherical nano-particles embedded in a host material (Maxwell Garnett system), (b) connected nano-structures (Bruggeman system)

2.1.2   Maxwell-Garnet Theory

Fig. 2.1.a represents a two phase medium with spherical nano-particles dispersed in a host medium. The ideal case for Maxwell-Garnett (MG) theory is such a system of spherical nanoparticles of metal, insulator or semiconductor of sizes much smaller than the wavelength of light [53]. MG approximation regime is limited to a relatively dilute system, i.e., the volume fraction of the nano-particles is relatively low $f \ll 1$. For such a medium of spherical nano-particles of permittivity, ε_i with volume fraction, f_i in a host medium of permittivity, ε_h , the effective permittivity of can be derived from eq. 2.3 by replacing vacuum permittivity by the host permittivity as given below,

$$\frac{\varepsilon_{eff}(\omega) - \varepsilon_h(\omega)}{\varepsilon_{eff}(\omega) + 2\varepsilon_h(\omega)} = f_i \frac{\varepsilon_i(\omega) - \varepsilon_h(\omega)}{\varepsilon_i(\omega) + 2\varepsilon_h(\omega).} \tag{2.4}$$

Eq. 2.4 can be further simplified to get,

$$\varepsilon_{eff}(\omega) = \varepsilon_h(\omega) + 3f_i\varepsilon_h(\omega)\frac{\varepsilon_i(\omega) - \varepsilon_h(\omega)}{\varepsilon_i(\omega) + 2\varepsilon_h(\omega) - f_i(\varepsilon_i(\omega) - \varepsilon_h(\omega))}. \tag{2.5}$$

MG model is successful in explaining colors seen in liquids or glasses when metal nano-particles are dispersed in it [53]. It is reported that the upper limit of f for good agreement of theory and experiments is $f \approx 0.1$ [56]. When the volume fraction is high, the system behaves non-linearly because of interactions of nearby nano-particles. MG model fails for such system as it assumes that the nano-particles are non interacting.

2.1.3   Bruggeman Theory

The disadvantage of MG formalism is that it does not work for systems with higher volume fractions. This is because with increase in volume fraction, the near-field interactions of adjacent electric dipoles in the nano-particles becomes stronger. That is, the dipoles can not be considered as isolated anymore. Bruggeman solved this problem by assuming that for a two phase effective medium both the host and the inclusions are embedded in the effective medium itself [54]. Eq. 2.3 can be used to derive the effective permittivity (ε_{eff}) for this condition by replacing the vacuum permittivity (which is =1) with ε_{eff} itself. This gives a symmetric function for the effective permittivity which is given by,

$$f_a\frac{\varepsilon_a(\omega) - \varepsilon_{eff}(\omega)}{\varepsilon_a(\omega) + 2\varepsilon_{eff}(\omega)} + f_b\frac{\varepsilon_b(\omega) - \varepsilon_{eff}(\omega)}{\varepsilon_b(\omega) + 2\varepsilon_{eff}(\omega)} = 0. \tag{2.6}$$

where index a, b denotes the two components in the medium. The effective permittivity of the medium is invariant with interchange in the components. One major advangatge of Bruggeman

13

theory is that it can be applied to randomly oriented nano-structures unlike MG formalism (Fig. 2.1.b). Zeng et al. [55], further generalized MG formalism to different shapes of inclusion given by,

$$f_a \frac{\varepsilon_a(\omega) - \varepsilon_{eff}(\omega)}{\varepsilon_a(\omega) + g[\varepsilon_a(\omega) - \varepsilon_{eff}(\omega)]} + f_b \frac{\varepsilon_b(\omega) - \varepsilon_{eff}(\omega)}{\varepsilon_b(\omega) + g[\varepsilon_b(\omega) - \varepsilon_{eff}(\omega)]} = 0; \qquad (2.7)$$

where g is a geometric factor which is 1/3 for spherical particles and 1/2 for circular discs. Eq.(2.7) has two roots for $\varepsilon_{eff}(\omega)$ given by,

$$\varepsilon_{eff} = \frac{-s(\omega) \pm \sqrt{s(\omega) + 4g(1g)\varepsilon_a(\omega)\varepsilon_b(\omega)}}{2(1-g)} \qquad (2.8)$$

The sign of the roots depend on f_i, frequency (ω) and ε_i of the system. Positive or negative root can be chosen based on physically reasonable conditions. We use Bruggeman theory to find the effective permittivity of thin discontinuous gold films similar to fig. 2.1.b used in fabrication of our devices.

2.2 Metamaterial Absorbers

Explanations for the resonant absorption in MPA are varied. Some adopt a metamaterials approach, where as usual for macroscopic electromagnetics permeablility describes the spatially averaged surface, and strong dispersion due to magnetic resonances creates a surface impedance to match that of free space [35, 50, 57–62]. Both permittivity and permeability are complex with strong dispersion that depends on geometry. The design can be tuned such that the surface impedance matches that of free space at any desired wavelength for minimum reflectivity. This occurs when permittivity equals permeability. Frequency selective surface (FSS) structure of the absorber can be designed to achieve polarization independent resonance bands.

However, alternative descriptions exist, such as the interference approach [51] which assumes that the anti-parallel currents in the metal layers are a result of interference and superposition, rather than excited by the magnetic component of the incident electromagnetic fields [51]. Planar wave-guide model given by Peng *et al.* [52] assumes that light diffracted through the periodic gaps in the top surface of the MA forms resonant standing waves inside the MDM structure which results in multi-band near unity absorptions. Below we concisely discuss some of the reported theoretical models of metamaterial absorbers such as magnetic resonance theory, interference theory and planar wave-guide model.

However, all the reported theories only shows numerical simulation results without an analytical model to quantitatively calculate the resonance characteristics such as resonance wavelengths or strength of absorption.
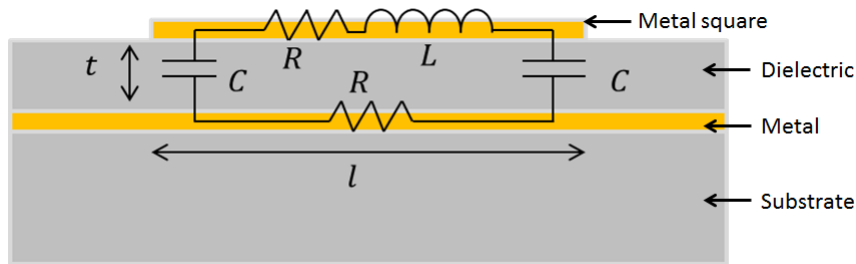
Figure 2.2: Schematic diagrams of a unit cell of a MPA with formation of LCR circuit

2.2.1   *Magnetic Resonance Theory*

Metamaterials are characterized by their magnetic behavior. Metamaterials shows non-unity magnetic permeability which arise due to presence of magnetic resonances. Pendry $etal.$, first calculated the effective permeability for periodic split-ring resonators [27]. Soon efforts were made for

experimental realization of such materials. Smith *et al.* first experimentally demostrated a meta-material constructed of copper split-ring-resonators with simultaneous negative permittivity and permeability in the microwave region. It was soon proposed that metamaterials can be fabricated to achieve perfect absorption using ultra-thin film structures [5,35,44,57]. Most of these absorbers were designed in the THz and microwave region. However, for absorbers in the visible and IR regions, slpit-ring-resonator structures were complicated for fabrication and FSS which are easier for fabrication such as squares [33] [41,50], crosses [60] or circular discs [9] were used showing strong absorption of incident light. However, none tried to explain the results with a quantitative theoretical model.

Ye *et al.* explained resonance mechanism in MPA using simple electro-dynamics [60]. In a MPA with FSS of squares/rectangles as shown in fig.2.2 magnetic resonance happens due to an electric dipole and the image dipole in the ground plane. Electrodynamic simulations of field distribution in MPA has shown such dipoles and image dipoles [41,50,60,62]. Simulations demonstrate excitation of fundamental and higher order resonances and corresponding absorption of the driving fields. In the case of the fundamental resonance, the incident electric field excites an electric dipole in the gold square. An image dipole is excited in the gold film under the spacer material. The driven current sloshing back and forth between the ends of the square, with opposite polarity in the ground plane, can be considered as charging and discharging capacitors located at the ends of the square. The resonant frequency is given by [60],

$$\omega = \frac{1}{\sqrt{LC}},\qquad(2.9)$$

where L is the mutual parallel plate inductance and C is the capacitance, which depend on the thickness of dielectric t and size of the absorber l, permeability, and dielectric permittivity according to $L = \mu_0\mu_r t$ and $C = \varepsilon_0\varepsilon_r l^2/2t$. The relative permeability has the value unity. From eq. 2.9

16

and the expressions for L and C, we find the fundamental resonance wavelength to be,

$$\lambda_0 = \pi n(\lambda) l \qquad (2.10)$$

LC resonance theory is simple and has been applied to calculate resonances for metamaterial absorbers in the IR regions [40,60]. However, LC theory can not explain multiple resonances seen in MPA and it can not explain dependence of resonance wavelenth on thickness of dielectric [40]. Also, the calculated resonance wavelength is 20% higher than experimental results [40].

2.2.2   Interference Theory

In interference theory, Chen *et al.*, assumes that the unity absorbption is because of multiple reflections and interference. In this model the anti-parallel currents in the two metal layers are assumed to arise from multiple reflections between the metal layers Chen et al shows that resonance strength and wavelength depends on thickness of the dielectric. This is also seen in our experiments. Such approach is similar to Fabry-Perot cavity absorbers [25, 63]. Interference model does not consider the fact that resonance wavelength depends on the size of the FSS structures such as size of the squares, length of wire-loop in split-ring-resonators. However, it has been shown that the resonance wavelength of MPAs linearly depends on the size of the FSS structures [33, 41, 60]. Thus, interference theory fails to explain the observed dependence of resonance wavelength on FSS structure.

2.2.3 Planar Wave-guide Theory

Planar waveguide model given by Peng *et al.,* [52] assumes that light diffracted through the periodic gaps in the top surface of the MPA forms resonant standing waves inside the MDM structure which results in multi-band near unity absorptions. According to planar waveguide model resonance wavelength is proportional to the periodicity of the FSS structure. However, in the case of a periodic array of squares, experiments show that the resonance wavelength is proportional to the size of the squares rather than the period [33, 50, 60]. Although, it is shown that in case of periodic arrays with much smaller gaps as compared to the metallic structures of the FSS, resonance wavelength is proportional to the size of the FSS structure for most of the reports the gaps are as big as the metal squares [11, 33, 40, 41, 50]. Thus planar wave-guide model fails to establish a connection between the size of the square and the resonance wavelength. Also, this model neglects the thickness dependence nature of the resonance wavelength. Planar waveguide model is not able to explain incident angle independent nature of the absorbption bands.

2.2.4 Metal-dielectric-metal (MDM) Cavity Theory

To explain the absorption mechanism of MPAs, we adapted a model similar to the planar wave-guide model proposed by Peng *et al.* [52]. The main assumptions of the MDM cavity theory are,

- Each unit cell in the metamaterial absorber is independent i. e., the cells are non-interacting.

- Each unit cell is considered as a MDM cavity where light is trapped in forms of standing waves.

MDM cavity model is an alternative way of explaining the physics of metametarial absorbers with FSS of squares, and rectangles without involving magnetic resonances. The in detailed analytical

18

derivations for this model is presented in chapter 3. Successes of the model include prediction of the fundamental and higher order resonance wavelengths, the dependence of these resonances on square size and dielectric thickness, the independence of the resonances on the period of the structure, and the insensitivity to polarization or incidence angle.

2.3   Finite Difference Time Domain (FDTD) Method

When characteristic size of the domain of interest is somewhat of the order of wavelength, ray-optics based methods of solving electrodynamic problems become difficult. That is where numerical methods come in. The FDTD method first introduced by Yee in 1966 [64], has become the most popular computational method for many scientific and engineering problems involving electromagnetic waves. FDTD method has applications ranging from microwave antennas, radar technology, wireless communication devices, MRI imaging, metamaterials, photonic crystals, plasmonics, solitons and biophotonics [65]. The absorbers fabricated in our work have sub-wavelength structures, FDTD simulations are performed for supporting development of theory and optimization of design parameters for the absorbers used.

2.3.1   Finite Difference Method

FDTD involves solving the time dependent Maxwell's equations using finitie difference method. In finite difference method differential equations are solved by approximating it to difference equations. Taylor's series expansion of $f(x_0 \pm \frac{h}{2})$ gives us,

$$f\left(x_0 \pm \frac{h}{2}\right) = f(x_0) \pm \frac{f'(x_0)}{1!}\left(\frac{h}{2}\right) + \frac{f''(x_0)}{2!}\left(\frac{h}{2}\right)^2 \pm \frac{f'''(x_0)}{3!}\left(\frac{h}{2}\right)^3 ... \qquad (2.11)$$

19

Using eq.(2.11) we can write,

$$\frac{f(x_0 + \frac{h}{2}) - f(x_0 - \frac{h}{2})}{h} = f'(x_0) + \frac{f'''(x_0)}{3!}\left(\frac{h}{2}\right)^2 + \dots \tag{2.12}$$

If h is sufficiently small, h^2 and subsequent higher order terms can be neglected. After rearranging eq.(2.12) we get,

$$f'(x_0) = \left.\frac{df(x)}{dx}\right|_{x=0} \approx \frac{f(x_0 + \frac{h}{2}) - f(x_0 - \frac{h}{2})}{h} \tag{2.13}$$

The central difference is calculated at neighboring points, $f(x_0 + \frac{h}{2})$ and $f(x_0 - \frac{h}{2})$ to give an approximation of the derivative of the function at x_0. Since the lowest power of h being neglected is second order, it is called a second order approximation. This is how a differential equation is converted in to a difference equation in finite difference method.

2.3.2   Derivation of FDTD Equations

The method begins with solving Faraday's law and Ampere's law given by,

$$\nabla \times \vec{E} = -\mu\frac{\partial \vec{H}}{\partial t} \quad \text{(Faraday's Law)} \tag{2.14}$$

and

$$\nabla \times \vec{H} = \varepsilon\frac{\partial \vec{E}}{\partial t} \quad \text{(Ampere's Law)}, \tag{2.15}$$

respectively. For a 1-dimensional case where the electric field varies only in the x direction, assume that the electric field has component only in the z direction. In this case eq.(2.14) and eq.(2.15)

can be solved to get two scalar equations given by,

$$-\mu\frac{\partial H_y}{\partial t} = \frac{\partial E_z}{\partial x}, \tag{2.16}$$

$$\varepsilon\frac{\partial E_z}{\partial t} = \frac{\partial H_y}{\partial x} \tag{2.17}$$

Eqs (2.16 & 2.17) are now converted to difference equations using finite difference method for solving numerically. In FDTD method, the electric and magnetic fields are calculated where one field is advanced then the other. Eq.(2.16) is used to calculate the future magnetic field in time while Eq.(2.17) is used to calculate the future electric field. This process is repeatedly done in a leap-frog manner until a steady-state electromagnetic behavior is obtained.

Since FDTD is a time domain method, by using a braod-band pulse as a source, results can be produced from a wide-range of frequencies which is useful when resonance wavelengths are not exactly known for a system. In FDTD, electric and magnetic fields are calculated over all the domain which is useful for creating visual representation of near-field distributions over sub-wavelength structures. Such features help examine the polarization and field distributions in metamaterial structures used in our experiments.

CHAPTER 3: FAR INFRA-RED ABSORBER BASED ON STANDING-WAVE RESONANCES IN METAL-DIELECTRIC-METAL CAVITY

In this chaper thin-film resonant absorbers for the far-IR spectral range were fabricated, characterized, and modeled. The 3-microns-thick CMOS-compatible structure comprises a periodic surface array of metal squares, a dielectric spacer and a metallic ground plane. Up to 95% absorption for the fundamental band at 53.5 microns wavelength (5.6 THz) is achieved experimentally. Absorption bands are independent of the structure period and only weakly dependent on polarization and incident angle. The results are well explained in terms of metal-dielectric-metal (MDM) cavity resonances. The structure has application as a wavelength selective coating for far-IR bolometers.

3.1 Introduction

In the microwave region and lower, electrons are the main particles of ineraction. On the other hand, at infrared and optical / UV wavelengths, the photon is the main particle for choice of device. However, in the terahertz (0.1-10 THz, λ=3mm-30μm) regime both electron and photon tend to interact very weakly with material. This makes THz imaging challenging due to lack of proper absorber materials. However, THz imaging has wide range of applications such as biomedical imaging [66], environmental remote sensing [67] , explosives detection [68], materials characterization [69, 70], and astronomy [71].

Bolometric or pyroelectric detection, in which the heat generated by far-infrared absorption is sensed, is usual in this wavelength range. Sensitivity depends on having efficient absorbers. Confinement of the absorption to specific wavelengths of interest improves signal-

22

to-noise ratios. Far-infrared metamaterial absorbers are studied as potential coatings for bolometers because of their high performance, thinness, and selectivity [5, 11, 35, 44, 57–62, 72]. Thin MAs are reported with polarization independent and omnidirectional absorption bands [2, 5, 11, 33, 35, 40, 41, 44, 50, 57–62, 72]. Typical MAs comprise 3 layers. A periodically patterned metallic top layer, together with a middle dielectric spacer layer and a conducting base layer, create resonances that achieve a frequency selective absorption. Reported patterns include split ring resonators (SRR) [5, 35, 44, 57–62, 72], crosses [60], squares and rectangles [2, 11, 33, 40, 41, 50]. The absorption band width, polarization dependence, and spectral line shape depend on design.

We present results for a far-IR absorber with a surface pattern comprising a periodic pattern of squares, which follows known near- [50] and mid-IR designs [41]. There are few prior reports of periodic square (or rectangular patterns) designed for far-IR absorption beyond ∼10 micron wavelengths [2, 11, 33, 40, 72]. We observe multiple absorption bands, which are attributed to fundamental and harmonic resonances. Up to 95% absorption was achieved in the fundamental band at 53.5 μm wavelength. A strong harmonic band with 98% absorption occurs at 30 μm. The absorption bands are independent of polarization and incident angle. One distinction between our device and previously-reported far-IR absorbers, which used polyimide as the dielectric spacer [5, 44, 57–62], our device employs only CMOS-compatible materials.

To interpret the experimental far-infrared reflectivity spectra, we adapted a model proposed by Peng et al. [52] based on standing wave resonances in a finite metal-dielectric-metal (MDM) waveguide. A number of modifications were implemented to improve the accuracy of this theory. Successes of the model include prediction of the fundamental and higher order resonance wavelengths, the dependence of these resonances on square size and dielectric thickness, the independence of the resonances on the period of the structure, and the insensitivity to polarization or incidence angle. Finite difference time domain (FDTD) simulations support the interpretation.
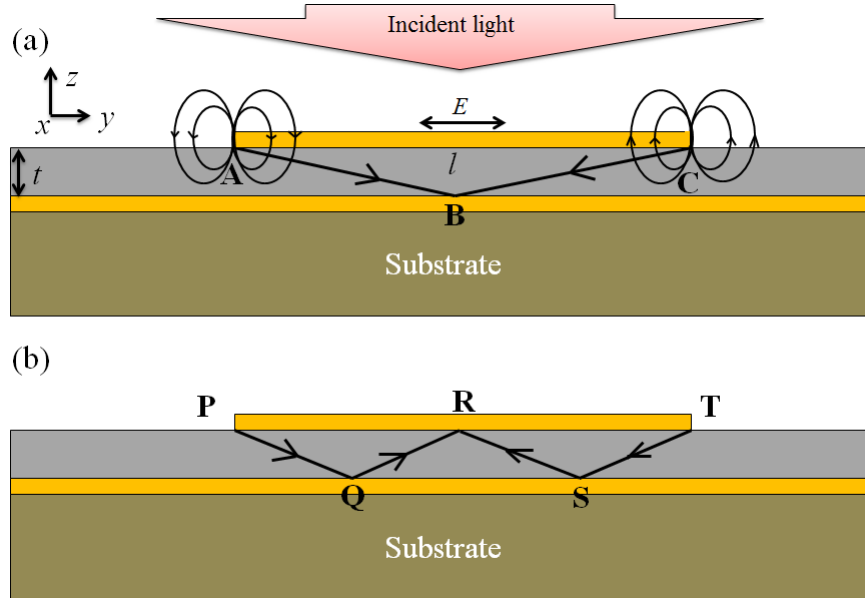
Figure 3.1: (a) Schematic of one unit cell of the structure. The edges of the metal stripes are sources of isotropically emitted radiation induced by the incident wave. Standing waves are formed under the stripe with different odd numbers b of reflections from the metal. Such resonances correspond to odd integer numbers of half-wavelengths along the different paths,(b) 2nd order resonance (b=3).

Fig.(3.1) presents a schematic side view of one unit cell of the structure. For simplicity we consider a 2D model with translational invariance normal to the plane of the figure, so that the top metallization consists of metal stripes of width l separated by gaps. The stripes are supported by a thin dielectric layer of thickness t. Underlying the dielectric is an optically thick plane of metal. Success of this model requires consideration only of one unit cell, and it is independent of the period of the strip array or the size of the gap between the stripes. Hence, Fig.(3.1) presents a schematic of just a single unit cell. Far-infrared radiation incident from above, and polarized with the electric

field in the plane of the figure (transverse magnetic TM), drives a periodic polarization along the top surface of the metal stripe. An opposite polarization appears along the bottom surface. The fields are strongly intensified at the edges of the stripes, creating a vertically-oriented oscillating dipole. These polarized edges comprise line-dipole sources of radiation, as suggested by the ray stars. This interpretation of the polarization and resulting field distribution was informed by the electrodynamics simulations of [52] and as shown below.

That width of the gaps between neighboring stripes is unimportant is supported by agreement of the theory with our reflectivity experiments on a single metal feature, where there are only edges while gaps are infinite [43]. In experiments reported here, the gaps are just a few microns wide, i.e. much smaller than the incident wavelengths. Nevertheless, the radiating edge dipoles assure that electromagnetic energy will appear in the dielectric layer. Existence proof of such an effect is the phenomenon of "extraordinary transmission" [73–76] through an array of sub-wavelength slits.

For our structures, the fundamental absorption resonance occurs at a wavelength (55 μm) that is much larger than the lateral dimension l (12 μm). The thickness of the dielectric (1-5 μm) in all our structures is also much less than the wavelength, so that we are beyond the cut-off for TM planar waveguide modes. Thus, the wave that penetrates under the squares is evanescent and should be strongly damped. However, the propagation distance required for the wave to interfere with a wave originating from the opposite edge is itself subwavelength. Thus, waves from neighboring gaps may interfere to form standing waves under the stripes. Waves at these resonances will experience extra loss due to enhanced interaction with the lossy metals.

Peng et al. [52] presented a model based on multiple reflections of rays and standing waves within similar sub-wavelength planar waveguides to interpret numerically-simulated absorption resonances. Methods based on propagation of rays, which hold in the limit of geometrical

optics, are of questionable validity for subwavelength structures such as those under consideration. Nevertheless, the ray picture has known pedagogical value in understanding the modes of planar waveguides even near cutoff when the wavelength is comparable to spacing between the conducting plates [77], even though this situation is similarly outside the regime of geometrical optics. Thus, we withhold doubt for the time being until we see how theory compares with experiment.

By symmetry, only an odd number of reflections b (for *bounces*) is possible from the top and bottom metals of the waveguide. Fig.(3.1b) present ray diagrams that illustrate resonances with one and three bounces, respectively. The optical path lengths of the indicated resonances are different, so that we expect corresponding absorptions to occur at different wavelengths, and for each closed path defined by odd values of b, we might expect a series of harmonics corresponding to different numbers of half wavelengths between the end points.

We have assumed negligible contributions from next-nearest neighbor edges and beyond, which is reasonable considering the strong attenuation for wavelengths beyond cut-off. Thus, resonance wavelengths are expected to depend primarily on two critical cavity dimensions, namely the lateral dimension l of the stripe and the thickness of the dielectric t, but not significantly on the period (or gap dimension). Ref. [52] ignored the possibility of a dependence on t by considering resonances based only on the horizontal dimension l, but predictions based on this assumption agree poorly with experiment.

For rays as indicated in Fig.(3.1a) the optical path length is

$$\Delta = (b+1)n(\lambda)\sqrt{t^2 + l^2/(b+1)^2} \tag{3.1}$$

where $n(\lambda)$ is the wavelength dependent refractive index of the dielectric (SiO_2 in our devices), and b is the odd number of reflections. The total phase difference for rays traveling from one edge

26

to the opposite edge, including a $-\pi$ phase shift at each reflection is

$$\phi = \frac{2\pi\Delta}{\lambda} - b\pi. \tag{3.2}$$

Standing-wave resonances occur when ϕ is an integral multiple m of 2π, so that the mth order standing-wave resonance occurs at wavelength

$$\lambda(b,m) = \frac{2(b+1)n(\lambda)}{b+2m}\sqrt{t^2 + l^2/(b+1)^2} \tag{3.3}$$

where $m = 0, 1, 2, 3$. The number of half wavelengths along the optical path at resonance is the odd number $2m + b$. The fundamental resonance $m = 0$ for $b = 1$ is

$$\lambda(1,0) = 4n(\lambda)\sqrt{t^2 + l^2/4} \tag{3.4}$$

For $b = 3$, the fundamental $m = 0$ occurs at

$$\lambda(3,0) = \frac{8n(\lambda)}{3}\sqrt{t^2 + l^2/16} \tag{3.5}$$

The first harmonic $m = 1$ for $b = 1$ is

$$\lambda(1,1) = \frac{4n(\lambda)}{3}\sqrt{t^2 + l^2/4} \tag{3.6}$$

For the range of t and l values in our device, we anticipate the three resonances Eqs. (3.4) in the wavelength range of our experiment with magnitudes $\lambda(1,0) > \lambda(3,0) > \lambda(1,1)$ Generally, the wavelength dependence of $n(\lambda)$ means that equations for the resonance wavelengths $\lambda(b,m)$ must be solved graphically or numerically.
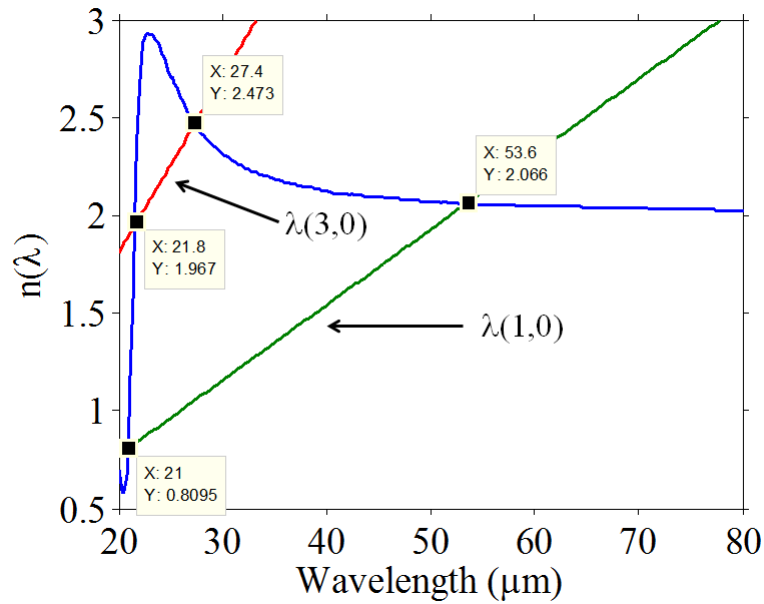
Figure 3.2: Calculation of resonance wavelength by graphical method. Blue curve represents refractive index of SiO_2. Green and red lines represents calculated $n(\lambda)$s for $\lambda(1, 0)$ and $\lambda(3, 0)$, respectively. Intersections of these straight lines with SiO_2 refractive index gives solutions to resonance wavelengths.

Fig. 3.2 represents graphical method of calculation of resonance wavelength. Blue curve represents refractive index of SiO_2 from ref [78] which shows dispersive nature 20 microns. Green straight line indicated as $\lambda(1, 0)$ is obtained from eq. 3.4 which can be used to calculate $n(\lambda) = \lambda/(4\sqrt{t^2 + l^2/4})$. Intersection of this line with the SiO_2 refractive index is the solution to the resonance wavelength for $\lambda(1, 0)$. For $\lambda(1, 0)$ two solutions are obtained at wavelengths 53.6 and 21 microns for a sample with parameters l=11.7 microns and t=3 microns. Similarly, for $\lambda(3, 0)$ resonances are obtained at 27.4 and 21.8 microns (intersection of red-straight line and SiO_2 refractive index). Solutions for $\lambda(1, 1)$ are calculated similarly at 26.8 microns and 20.5

microns(not shown in fig. 3.2).

Since the edge polarization is the source of the waves in the waveguide, the theory predicts that the resonance wavelengths are independent of the angle of the incident light that excites the polarization. The theory assumed translational invariance out of the plane of the page, forming a 1D grating of metal stripes, for which edge polarization can be excited only by TM polarized light. In the actual device, there are two orthogonal arrays of slits, creating a 2D array of metal squares. Thus, we expect that optical response of the actual devices to be polarization independent.

The analytic theory predicts the wavelengths of expected resonance absorptions but not the strengths or widths of the resonances. To obtain these, finite difference time domain (FDTD) electro-dynamic numerical simulations were performed using Lumerical FDTD solutions (Version 8.9). The optical constants for gold were determined from the Drude model using with parameters from [79]. SiO_2 optical constants were taken from [78] for fused silica. In contrast to the analytic theory, the numerical calculations considered a fully 3D model corresponding to the actual experimental structures. The infinite array of surface squares was treated by considering a single unit cell with periodic boundary conditions in x and y directions. Perfectly matched layers (PML) – which absorb plane waves of arbitrary incidence angle, polarization, and frequency – are used to create perfectly absorbing boundary walls above and below the structure [80]. These PMLs are required to make sure that the reflected and transmitted light from the sample does not get back in by reflection from the walls above and below. A normally incident plane wave is considered with electric field polarized in y-direction, i.e. perpendicular to the edges of the gaps. A frequency domain field and power monitor is used to measure the specular reflection. The reflectivity was measured using a 2D field monitor at 0 deg and spanning the unit cell. Transmittance is zero due to the metal ground plane.

The corners on the squares were not accounted for in the analytic theory. Furthermore, the numerical calculations differ from the actual devices by having perfectly sharp corners and ideal metal. These may be sources of the small disagreements between theoretical, numerical, and experimental results.

3.3 Experimental Details
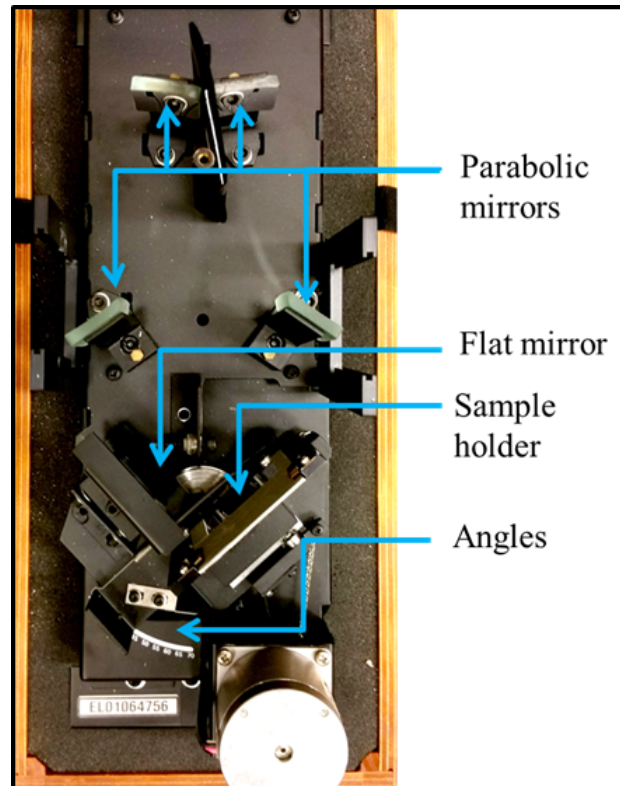
Figure 3.3: Setup for angle dependent specular reflectance measurements

The ground plain and dielectric were deposited using a multi-pocket electron beam evaporator without breaking vacuum. First, a 10 nm Cr sticking layer followed by 200 nm of gold were

deposited on glass or Si substrate. A second 10 nm Cr sticking layer was then deposited followed by evaporation of the SiO_2 dielectric spacer. Square patterns of gold were fabricated on the SiO_2 film by standard photolithography, DC sputtering, and lift-off. The sputtered gold sticks well to SiO_2 without a sticking layer. Square dimensions and array period were determined by scanning electron microscopy (SEM). Their nominal values were 10 and 20 μm, respectively. The thickness of the top gold squares is 200 nm as determined from SEM of a cleaved and polished cross-section.

Reflectance was measured using a BOMEM DA8 Fourier spectrometer with globar source, 6 micron Mylar pellicle beam splitter, and room-temperature DTGS detector. Two different reflectivity accessories were used within the evacuated sample compartment. The first was at fixed angle for near-normal incidence, where the initially focused incident beam of the spectrometer was collimated by a concave mirror and was incident on the sample at an angle of 8 deg using a mirror assembly. The reflected light was diverged at the proper acceptance angle for the spectrometers detector module. The second reflectance accessory enabled variable-angle specular reflectance measurements for incidence angles of 20, 40, and 60 deg (Fig. 3.3). Reflectance R was obtained by dividing the raw reflected power spectrum with that of an optically thick smooth gold film. Transmittance through the sample is zero because the underlying gold film is optically thick. Thus, absorptance $A = 1 - R$. We assume negligible scattering because the squares are much smaller than the wavelength.

3.4   Results

Absorptance $A = 1 - R$ was determined from the numerically calculated specular reflectance R as a function of geometrical parameters for the device. Fig. 3.4.a presents a color-map of A for square dimension $l = 11.7$ μm as a function of wavelength and dielectric thickness t, which is varied from 1 to 4 μm. Two strong absorption bands are observed to redshift with increasing t in the considered

wavelength range 20 to 80 μm. The longer wave band is identified as the $\lambda(1,0)$ resonance, while the shorter wave band is $\lambda(3,0)$. There is also a weak absorption band with weaker t dependence that emerges below the lowest strong band at about 25 mum, and this we identify as the $\lambda(1,1)$ resonance.
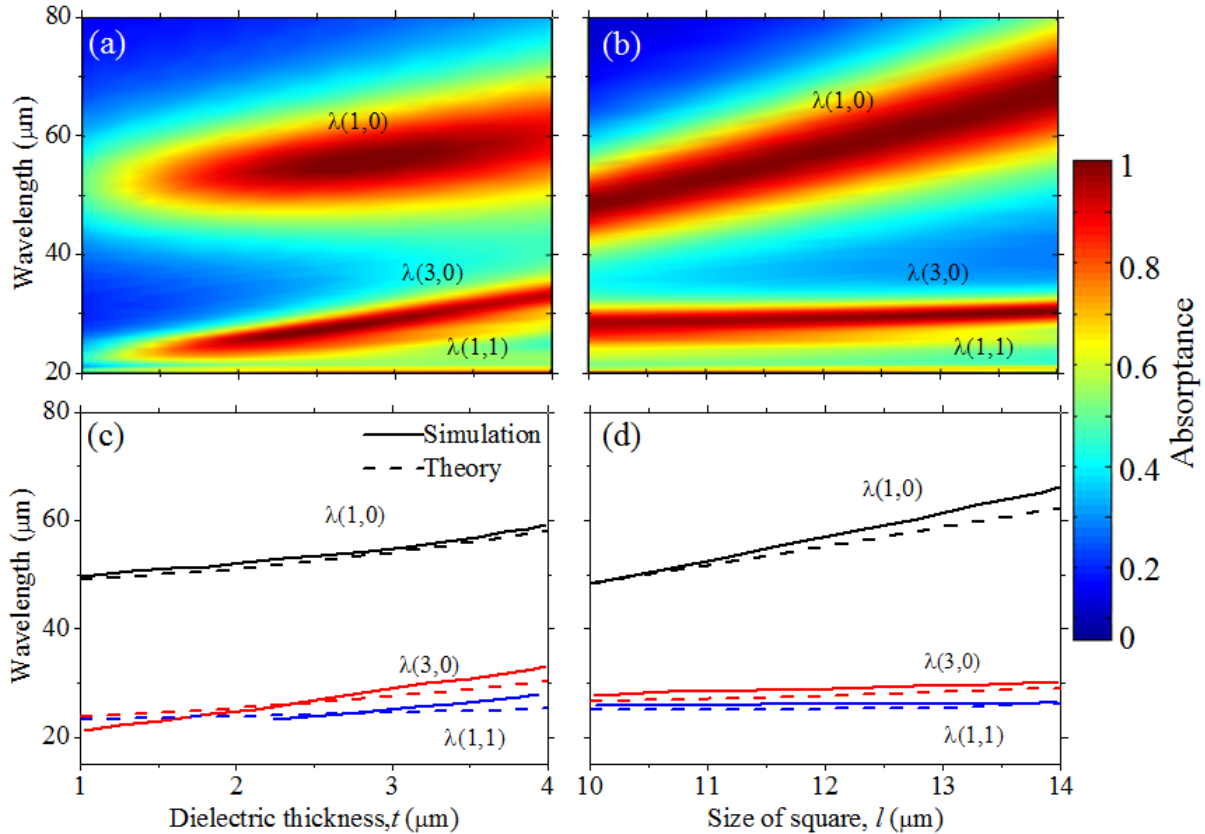
Figure 3.4: Colormap of absorptance as a function of wavelength and (a) dielectric thickness or (b) size of squares. Analytically (dashed line) and numerically (solid line) calculated resonance wavelengths as a function of (c) dielectric thickness, (d) size of squares.

Additionally, Fig. 3.4 shows evidence of another absorption which stays at 20 μm

wavelength along the bottom edge for the complete ranges of t and l. This is attributed to secondary and coincident solutions for $\lambda(1,0)$, $\lambda(3,0)$, and $\lambda(1,1)$, which appear because of strong dispersion of SiO_2 near 20 microns wavelength. These identifications were determined from the graphical intersection of the refractive index spectrum $n(\lambda)$ for SiO_2 and the linear curve for $n(\lambda)$ given by Eqs.(3.4-6), as was done in [40].

Fig. 3.4.b presents A as a function of λ and l for $t = 3\mu m$. The identification of the bands is the same as in Fig. 3.4.a. Comparison of the two parts of Fig. 3.4 shows that the dependence of $1,0)$ on l is stronger than it is on t, but for $\lambda(3,0)$ the opposite is true. Moreover, the strengths of the absorptions are sensitive to the value of t, but not to the value of l.

Fig. 3.4(c-d) compares the analytically and numerically calculated resonance wavelengths. The analytic and numerical calculations used the same values of $n(\lambda)$ from [78]. The curves calculated from Eqs. (3.4-6) agree sufficiently well with the numerically-determined bands to confirm the mechanism of the absorption and the identity of the resonances. The small differences may be due to the different assumptions in the analytic and numerical calculations already mentioned.
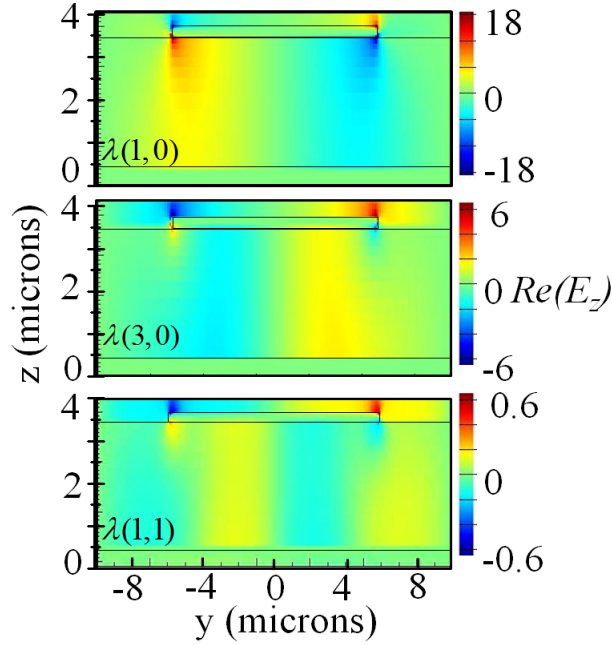
Figure 3.5: Colormap shows Re(Ez) for $\lambda(1,0)$, $\lambda(3,0)$, and $\lambda(1,1)$ for absorber with $l = 11.7$ μm and $t = 3$ μm.

3.4.1   FDTD Simulation Results

Fig. 3.5 presents color-maps of real part of the electric field component Ez, i.e. the component normal to the plane of the device, for the $\lambda(1,0)$, $\lambda(3,0)$, and $\lambda(1,1)$ resonances. The images are side views of one period of the structure. The ground plane occupies the bottom of each frame. One of the squares appears centered horizontally near the top of the frame. The normally incident light is polarized in the plane of the figure, and this causes a polarization along the top surface of the square. Along the bottom surface, an opposite polarization appears. With charge piling up at the edges of the squares, a strong vertical polarization appears at each edge. This oscillating dipole

is responsible for radiation that appears in the subwavelength cavity under the square. The plotted Ez component appears only because of this edge dipole, since the incident wave had no vertical component. A similar qualitative picture is evident in the simulations presented by [52].

Fig. 3.5 shows that for the $\lambda(1,0)$ resonance, Ez changes sign once in going from the left edge to the right edge, which is consistent with the observation already made that for this resonance one-half wavelength should fit along line ABC (Fig. 3.1).

For $\lambda(3,0)$ Ez changes sign thrice from the left edge to right, with a node at the center line, as expected if 3 half-wavelengths fit along line PQRST in Fig. 3.1. The regions of a particular sign of the field are unevenly distributed under the square, being high localized near the edge and more diffuse away from the edge. Note that the color scale is reduced 3x for $\lambda(3,0)$ in comparison with $\lambda(1,0)$. Since power loss goes as the square of the field, we expect this shorter-wave absorption to be correspondingly weaker. This is confirmed in Fig. 3.1, where since the two strong peaks are both saturated at unity absorbance, the weaker absorption manifests as a decrease in width.

The color scale for $\lambda(1,1)$ is 30 x smaller than for $\lambda(1,0)$ so that this band should be much weaker than the others, in agreement with Fig. 3.4. In Fig. 3.5, considerable intensity for $\lambda(1,1)$ is found beyond the edges of the square, and it is more difficult to deduce that the expected 3 half wavelengths between the edges. Following the horizontal centerline, Ez clearly changes sign twice, consistent with 3 half wavelengths from left to right. On the other hand, following a horizontal slice just below the square, it appears that the field changes sign 4 times, suggesting 7 half wavelengths.
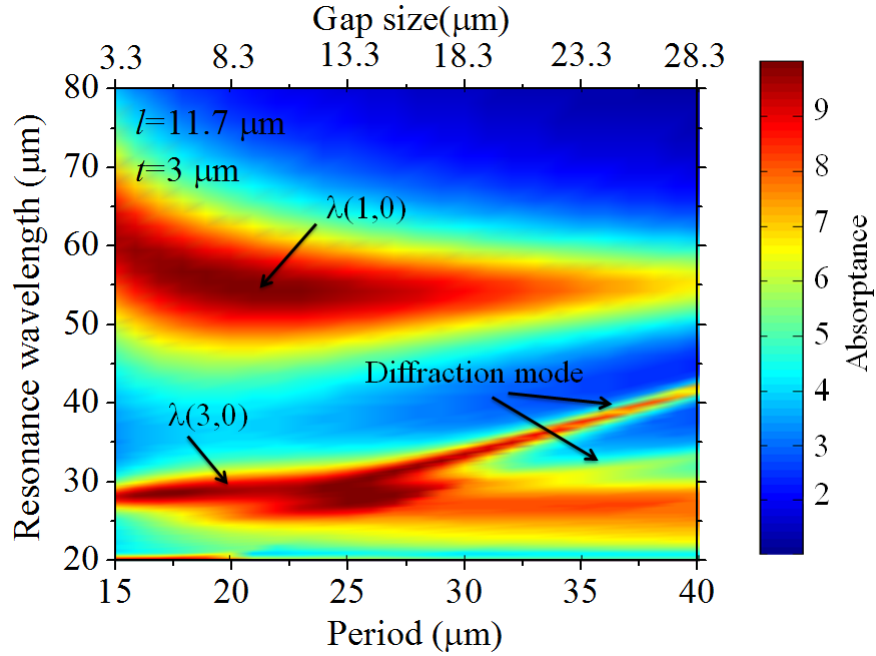
Figure 3.6: Simulated absorptance as a function of wavelength and period of the squares. The size of the squares and thickness of the dielectric are l=11.7 microns and t=3 microns, respectively. l and t remains constant as period varies from 15-40 microns.

The analytical formulas Eqs. 3.4-6 for the resonance wavelengths are independent of the period of the surface structures. To investigate, we performed simulations as a function of period. Fig. 3.6.4 presents absorptance $A = 1 - R$ found from the numerically calculated R for normal incidence specular reflectance as function of wavelength and period of the surface structures. The size of the squares and the thickness of the dielectric were fixed at $l = 11.7$ m and $t = 3$ m. Between 20 and 40 micron period, i.e. for gaps of $\sim$8-28 μm, there is no change in the position of the $\lambda(1,0)$ resonance, in agreement with the analytic theory. Below 20 μm period, for gaps between squares decreasing from 8 to 3 μm, the fundamental resonances red-shifts and slowly weakens. From Fig. 3.5, it is clear that the Ez component extends at least 2 microns beyond the edge of each square, so

it is reasonable to expect that neighboring opposite dipoles begin to load and destructively interfere with each other at gaps smaller than 8 microns, thus red-shifting and weakening the resonance.
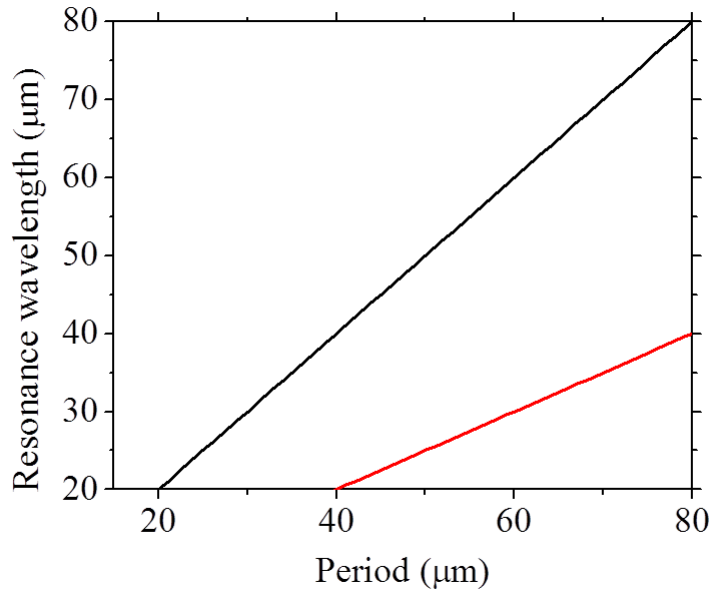
Figure 3.7: Woods Anomolies of Rayleigh type, where emergence of the pth diffracted orders into the air above the grating removes intensity from the specularly reflected beam. Black and red lines represent 1 and 2nd diffracted orders, respectively. Since the simulation was over 15-40 microns period, 2nd order was not seen in the simulations.

The resonance near 28 microns wavelength shows considerable structure. A branch with little period dependence we identify as the resonance. At about 27 μm period, a strong mode with linear period dependence emerges at reaches 42 μm wavelength by 40 μm period. A second weaker mode emerges near 30 μm period and reaches 33 μm wavelength by 40 μm period. These two modes represent the loss of specular reflected power due to diffraction, where diffracted wavelengths depend on period a and resonance order m according to $\lambda = asin\theta/m$. Since, angle of

incidence is 0 deg and R is measured for specular reflection, any diffracted light at angles different than zero will not be collected by the detector in the simulation.
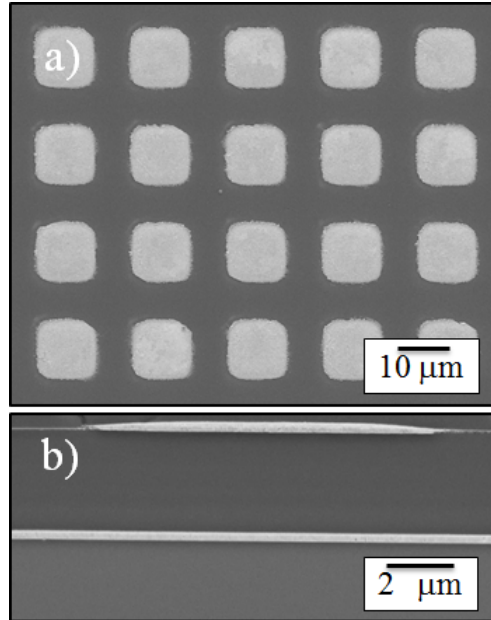
Figure 3.8: SEM image of a) sample surface, b) cross-section view of a cleaved sample.

The behavior of the band formed by the partially overlapping $\lambda(3,0)$ and weaker $\lambda(1,1)$ is more difficult to interpret. Most obviously, the redshift observed for $\lambda(1,0)$ at the smallest period is missing, presumably due to less interaction between neighboring dipoles for these shorter-wavelength and weaker fields. Next, at periods greater than or equal to the wavelength, two branches split off and shift linearly to increasing wavelength with increasing period. These are diffraction orders, which appear as absorption only because they are not collected by the detector for specular reflection.

The band at 20 microns wavelength, which corresponds to secondary solutions for the $\lambda(b,m)$ due to the strong dispersion of SiO_2, exists only for periods between 15 and 20 μm, before

evidently blue-shifting out of the frame. This might be explained by a reduction in the effective index of the dielectric as proportion of metal is decreased [63], which would decrease the resonance wavelength according to Eq. 3.4.

Fig. 3.8 presents an SEM images of a) the sample surface and b) a cleaved and polished cross-section. Such surface images were used to determine the size of the squares and the period, which are inputs for the analytical and numerical calculations. The latter also depend on the degree to which the corners were rounded, which was also determined from the images. The cross section was used primarily to confirm the thickness of the oxide.
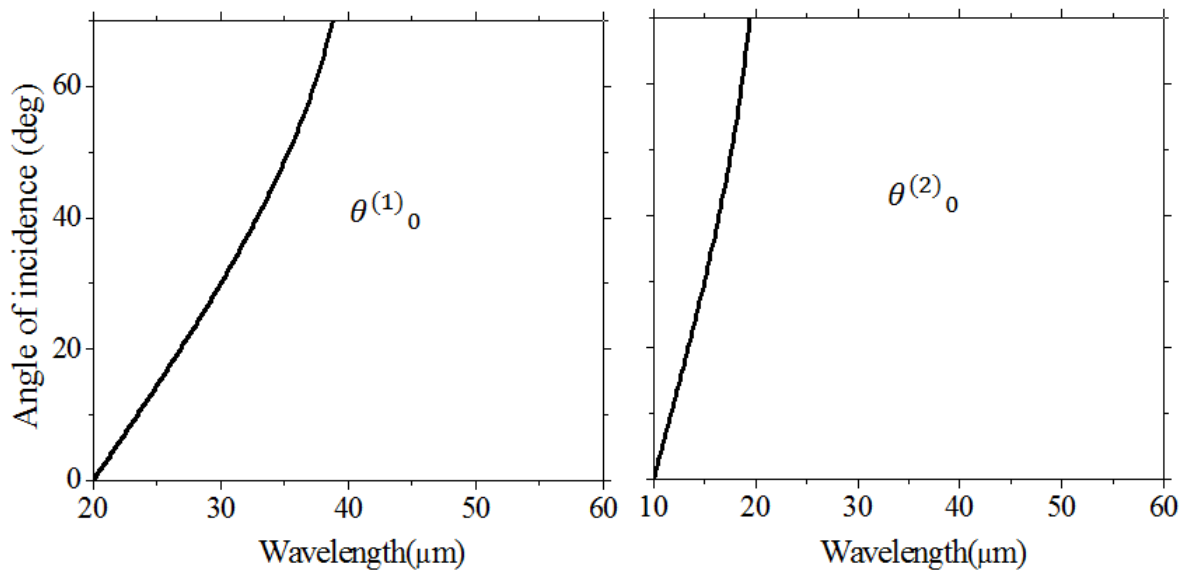
Figure 3.9: Woods anomaly as discussed already in fig. 3.7. Angle dependence of two of the modes are calculated according to $\theta = sin^{-1}(1 - \lambda/a)$.

Fig. 3.10 presents reflectance spectra for samples with different SiO_2 thicknesses (t).

The nominally identical l values in fact vary from sample to sample by up to 15%, due to experimental processing uncertainties such as baking time, UV light intensity, development time, etc. With increasing t the peak of the absorption shifts to longer wavelength, as predicted by Eq. (3.4) for the fundamental $\lambda(1,0)$. The strength of the fundamental $\lambda(1,0)$ absorption varies between 62 and 95% for the different values to t. The deepest absorption is achieved at 53.5 microns wavelength (5.6 THz) when $t = 3$ microns. This is in agreement with numerical results plotted in Fig. 3.4a. The dashed line represents numerical results for $t = 3.5$ and $l = 11.7$ microns sample at normal incidence, showing good agreement with experiment.
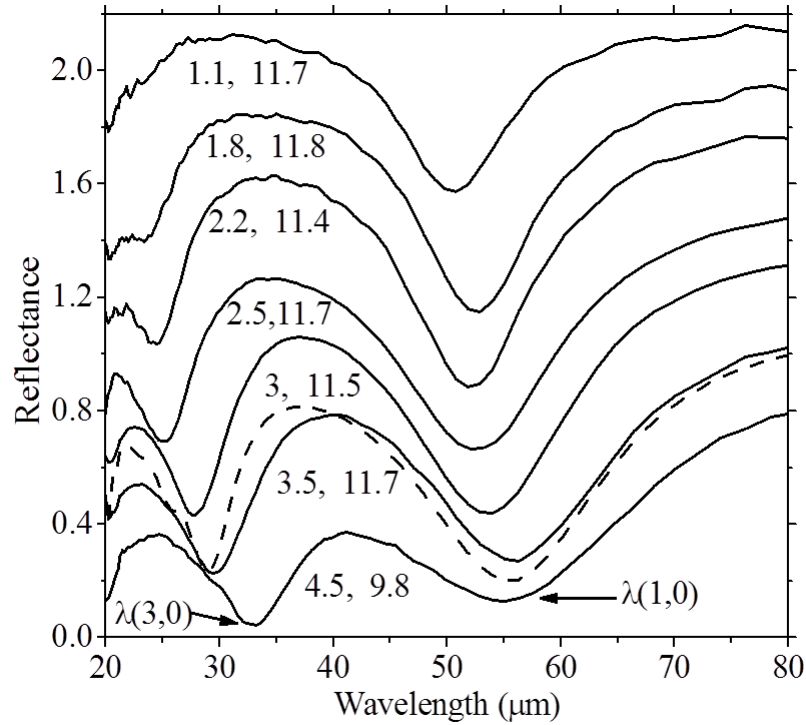
Figure 3.10: Experimental reflectance spectra at 8 deg angle of incidence for different samples with numerical labels indicating SiO_2 thickness and square size, (t, l), respectively. Spectra for successively smaller t values are offset vertically by 0.2 units for clarity. The dashed line is the result of numerical calculation for structure values (3.5, 11.7) at normal incidence.

The $\lambda(3,0)$ mode emerges into the frame Fig. 3.10 at 25 microns when t= 1.8 microns, and it redshifts finally to 33 microns with increasing t as predicted. Evidence for the expected but weak $\lambda(1,1)$ absorption may be the asymmetry of the band due to a short-wave shoulder near 30 microns wavelength when t = 4.5 microns. There is evidence for the secondary solutions of $\lambda(b, m)$ due to the strong dispersion of SiO_2 at the short wave edge of the frame, as mentioned in the discussion of Fig. 3.4a.

Fig. 3.11 plots the experimental peak wavelengths of modes $\lambda(1,0)$ and $\lambda(3,0)$ from Fig. 3.10 as a function of theoretical resonance wavelengths according to Eqs. (5.4) and (5.5). The straight line is $\lambda(b,m) = \lambda(\text{exp})$. The agreement between observed resonance wavelengths and analytic theory is excellent.
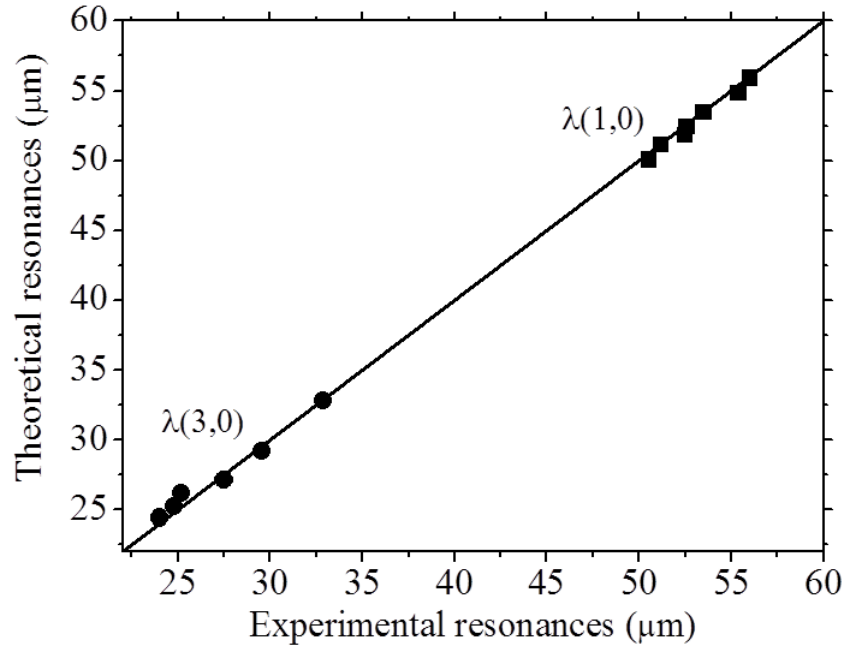
Figure 3.11: Theoretical resonance wavelengths $\lambda(b,m)$ vs. experimental resonance wavelengths $\lambda(\text{exp})$ The symbols are the $\lambda(1,0)$ and $\lambda(3,0)$ experimental data for different structure dimensions l and t.

Fig. 3.12 presents numerical absorptance spectra as a function of angle of incidence and wavelength for TM and TE light for a structure with $l = 11.7$ and $t = 3$ microns. At normal incidence there is no distinction between TM and TE modes, and the calculated spectra are reassuringly identical. For TM polarization, the strength of the fundamental $\lambda(1,0)$ remains constant up to 70 deg angle of incidence, with the main effect being a 4% blueshift beyond 60 deg. The behavior

of the $\lambda(3,0)$ band is more complicated. A strong satellite emerges at about 20 deg and redshifts linearly with angle. This is interpreted as a Woods anomaly as discussed already in regard to Fig. 3.9. This is confirmed using the diffraction equation with the angle of the first diffraction mode θ_1 = 90, namely $\theta = sin^{-1}(1 - \lambda/a)$. Otherwise the $\lambda(3,0)$ band shows mainly a small blue shift and intensity variation with angle.
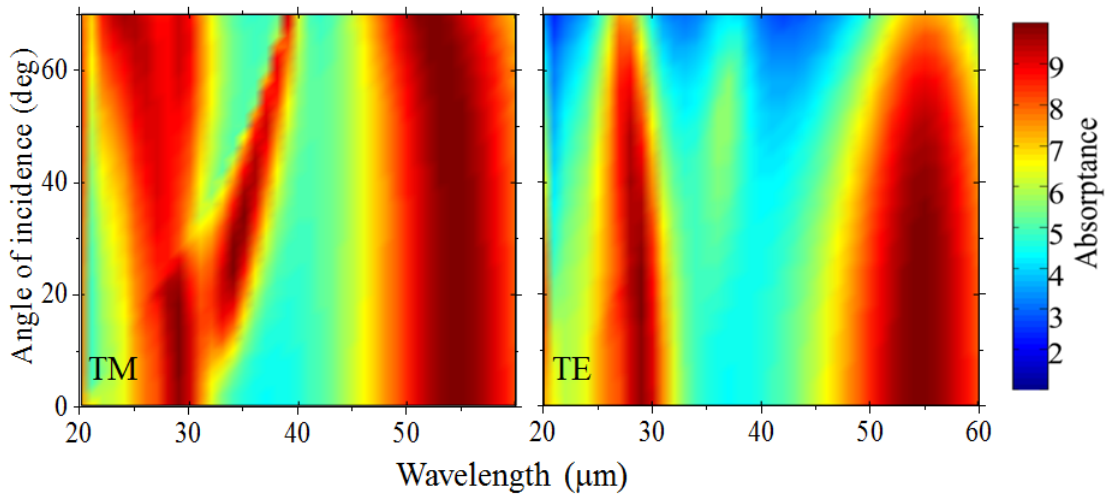
Figure 3.12: Numerically calculated absorptance as a function of angle of incidence and wavelength for (a) TM and (b) TE polarization.

For TE polarization, the position of the modes is almost independent of angle, and the main effect is a weakening that appears only beyond 40 deg. Interestingly, the strength of the absorption falls off much more slowly than the projected area of the square on the propagation direction ($cos\theta$), showing that the incidence light remains effective at driving the surface polarization that leads to the edge dipoles even at large angles. The diffraction mode that appears for TM shows up only weakly in TE polarization.

Fig. 3.13 compares experimental and numerical reflectance spectra for TM and TE

polarization at angles of incidence 20, 40 and 60 degrees. Experimental data match well with simulations, particularly for the fundamental absorption at 55 microns. The Woods anomaly also appears in the experimental data, appearing most prominently in TM polarization moving from 30 to 40 microns wavelength with increasing angle.
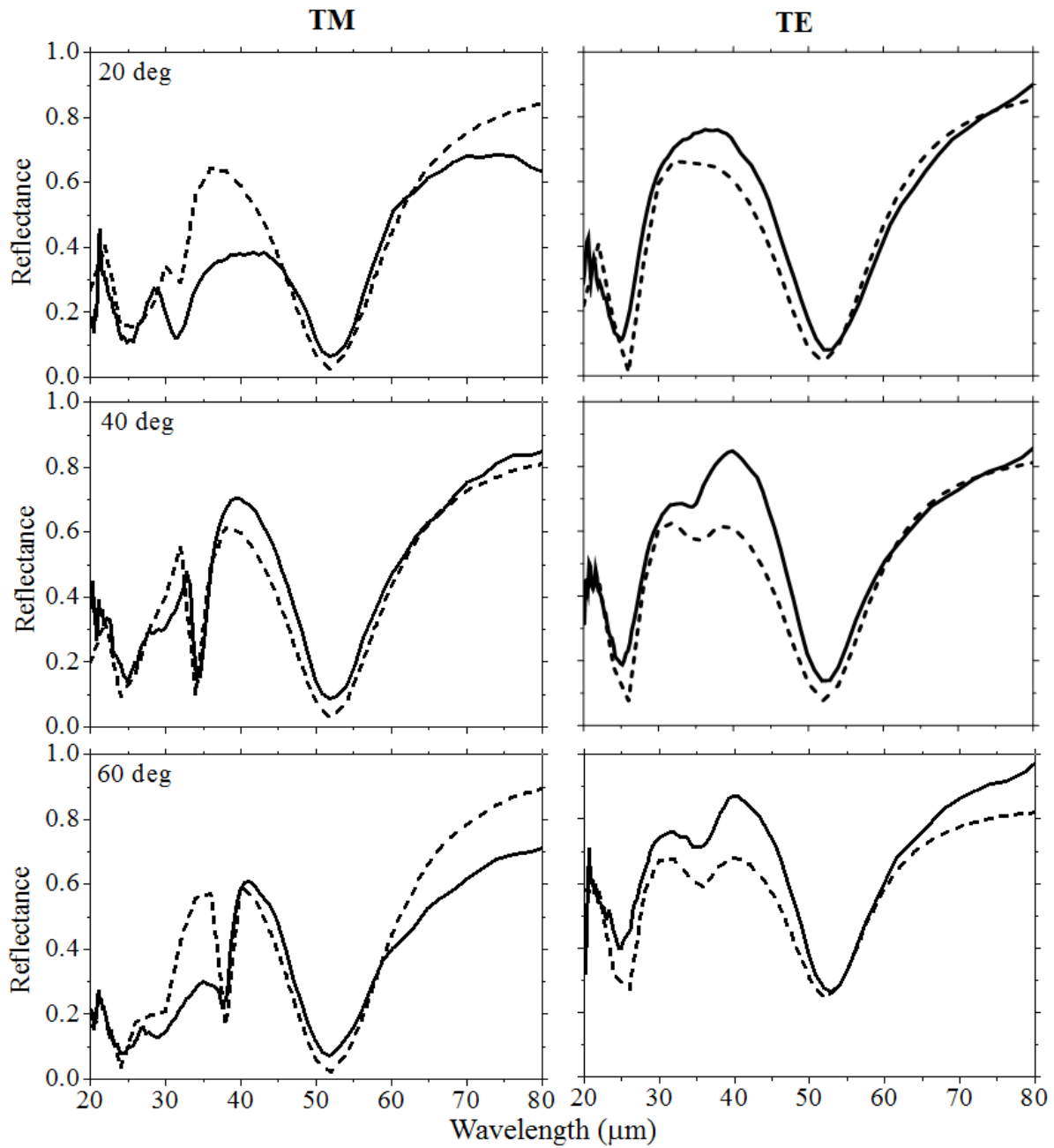
Figure 3.13: Angle and polarization dependence of experimental (solid lines) and numerically calculated (dashed lines) reflectance spectra. Device parameters were $l = 11.4$ and $t = 2.5$ microns. Polarization is TM (left column) and TE (right column). Angle of incidence is indicated.

3.5   Discussion

The analytical formulas Eqs. (3.4-3.6) for the resonance wavelengths are independent of the period of the surface structures. For fixed square size, as the period gets smaller, the gaps become smaller. As the edges get closer, the fields from one edge dipole may begin to interact with the neighboring dipole, and since neighboring dipoles are oppositely oriented, their fields would tend to cancel. The closing of the gaps should eventually cause the absorption to disappear. As the gaps close, a weakening and red-shift are expected due to superposition of opposite dipoles and increased inertia from coupled charge oscillations. Both weakening and red-shift were observed for the fundamental $\lambda(1,0)$ with reduction in period in the numerical calculations presented in Fig. 3.6.

On the other hand, as the period is increased, different effects would come into play. For periods comparable to the wavelength, diffraction orders would emerge into the space above the device, taking some of the power from the specularly reflected beam, an effect known as Woods anomaly of Rayleigh type [81]. Since both experiment and numerical calculations determine the intensity of the specularly reflected beam, these diffraction features appear in the reflectance spectrum artificially as absorptions, as in Figs. 3.6, 3.12 and 3.13.

For periods much larger than the square size, the absorption for wide beams would be weakened by the decrease in fill factor, but the strength of the absorption at each square should remain about the same. Indeed, diffraction-limited reflection spectral microscopy on isolated squares shows resonance wavelength and line shape to be the same, though apparently 1.4 times weaker, than for a measurement on our periodic array with same spot size [43]. Diffraction diffuses the apparent absorption at the center of an isolated square, explaining the weakness compared to the period array as a measurement artifact. That the absorption depends only weakly on angle of incidence is explained by the proposed mechanism, in which the incident light polarizes the squares, leading to oscillating dipoles, which are the sources of new waves that propagate into the dielectric

and form lossy standing waves under the squares. The existence of such dipoles is supported by the electrodynamic simulations (Fig. 3.5). The standing wave model is supported by the agreement with the dependence on geometrical parameters, including dependence on the dielectric thickness, which had been previously ignored in [52].

We next contrast our results and interpretation with those of other authors for nominally similar absorber structures. Hao et al. [33] present numerical results for a periodic array of Ag squares on Al_2O_3 on Ag ground plane, which are scaled to have absorption resonances at visible wavelengths. This group presented experimental demonstration of resonant absorption for one set of geometrical parameters at one angle of incidence in [50]. Notable similarities to our work include the appearance of higher order resonances, transmission through the subwavelength gaps between the squares, and standing-wave field distributions in the sub-wavelength space in the dielectric beneath the squares. A notable difference is that their calculated resonance wavelengths increase with decreasing dielectric thickness, opposite to our analytic, numerical, and experimental results. A second notable difference is that Hao et al.s simulations show horizontal polarizations on the top and underside of the surface square have the same sign, so that no vertically-oriented oscillating edge dipoles appear as in our simulations. A hypothesis for the differences is that the visible spectral regime of [50] is closer to the plasma resonances of their metal squares, and these lie closer to the ground plane relative to their lateral dimensions. The dependence on dielectric thickness in [50] is qualitatively similar to the redshift observed in high-electron mobility transistors when the separation of between two-dimensional electron gas and the metal surface gate is decreased [82–85]. In other words, for the dimensions and wavelengths of [33], a microscopic model based on plasmons (as indeed suggested in [50]), rather than standing waves, seems required. Since no comparison of numerical or experimental resonance wavelengths to predictions of an analytic theory was made in [33, 50], the absorption mechanism remains somewhat speculative. However, our Eq. (3.33) gives resonance wavelengths for the structures in [33] that are

a factor of 2 too small, even when account is taken for dispersion that causes reflection phase shifts with magnitudes somewhat smaller than π in the considered spectral range. Thus, there are apparently dimensional and wavelength regimes where the standing wave model works poorly.

Diem et al. [11] presented numerical calculations of an absorber comprising tungsten stripes on silicon nitride on tungsten ground plane. The structure is nominally similar to the model structure used for our analytic theory derivations. For the assumed dimensions, the resonance appeared at 4.28 microns in the mid-IR. As in our device all dimensions are subwavelength, and all the materials used are compatible with standard silicon processing. In contrast to our device, the width of their stripes was less than the gaps between them and less than the dielectric thickness. Unlike our device, their simulated field distribution does not show standing waves under the stripes. No analytic formula is given for the resonance wavelength and no comparison to experiment is provided. Our Eq. 3.3 predicts the higher order resonance $\lambda(3,0)$ at 4.21 microns, but the near agreement is probably coincidence given the dissimilar field distributions. Since only the magnitude of the field is given in the field distribution plot, it is impossible to know the nature of the polarization in the squares.

Chen proposed a theory based on interference between rays reflected from a periodic metal surfaced pattern and rays reflected from a metal ground plane separated by a dielectric spacer [51]. Due to the complex permittivity of the metal and dielectric, there are phase shifts on reflection and transmission that vary strongly with wavelength, allowing destructive interference between the partial front-surface reflection and multiply reflected waves in the dielectric, even though the dielectric thickness is much smaller than the wavelength. This results in a resonance with near-zero total reflectance and correspondingly strong absorption. The phase shifts and wave amplitudes needed in the Fresnel Equation analysis were determined from numerical simulations. No analytical formula was presented to predict the resonance wavelength, which for their simulation parameters was 306 microns, and there was no comparison to experiment. Chens

model does not depend on the size of the front-surface metal features, in strong contrast to what we and others report. Chens resonance wavelengths red-shift by about the same amount as we observe with increasing dielectric spacer thickness (10% with 4-fold change in thickness). Chens condition for destructive interference should depend strongly on angle of incidence, which was not considered in [51], and this is strongly at variance with the omni-directional nature of the absorption seen in Fig. 3.13 and widely reported by others. The mechanism proposed by Chen is similar to that used to describe Fabry-Perot type absorbers [25], such as the optical Salisbury screen [63].

Paper	Operating wavelength	Materials	Square thickness	Optical skin depth $\frac{1}{\mathrm{Im}(n)\omega/c}$	Quasi-static skin depth $\sqrt{\frac{2\rho}{\mu_0\omega}}$	Cross-section of polarization
Hao	0.7 microns	Ag $\rho = 1.6 \times 10^{-8}\Omega.m$ $n= 0.2+i4.4$	30nm	25nm	N/A	
Peng	5 microns	Au $\rho = 2.4 \times 10^{-8}\Omega.m$ $n=21.4+i27.9$	200nm	31nm	N/A	
Peng	33 microns	Al $\rho = 2.8 \times 10^{-8}\Omega.m$ $n= 75.4+i217.6$	200nm	24nm	26nm	
Nath	55 microns	Au $\rho = 2.4 \times 10^{-8}\Omega.m$ $n= 41+i224.5$	200nm	39nm	34nm	
Ye	60 microns	Au $\rho = 2.4 \times 10^{-8}\Omega.m$ $n= 42.3+i226.8$	200nm	42nm	36nm	

Figure 3.14: Comparison of polarization on the square

Ye et al. [60] present an LC resonance model, in which the self-inductance L for each

unit cell in the periodic array is determined by the magnetic energy stored between surface structure and ground plane, and where parallel capacitors are formed between each half of the surface plate and ground plane. The resonance wavelength is proportional to the dimension of the surface structure only, but uncertainty in estimating L and C values causes the resulting analytic formula for resonance wavelength to have only order-of-magnitude accuracy when compared to experiment [40]. Furthermore, the lack of a dependence on dielectric thickness for the resonance wavelength so estimated, and the absence of higher order resonances, contradict results presented here and by others. No field distribution in cross section is presented, so it is impossible to compare the nature of the polarization in the surface structure.

Although the standing wave model proposed by Peng et al. [52] and elaborated here seems to work well, those authors asserted that resonance wavelengths depend on periodicity. In fact, it appears that resonance wavelength depends not on period but on the dimension of the metal squares, which is supported in [33, 40, 41, 43, 50, 60]. Peng *et al.,* also ignored the dependence on dielectric thickness, which has been shown to be significant here and by many authors already cited.

Fig. 3.14 compares polarization of the top square edges for several reports mentioned in the table. It is found that when the top film is much thicker than the skin depth, the polarization of the electric field at each edge are opposite. When the thickness of the square is close to that of the skin depth similar polarity of the field is obtained. Hao *et al.* [33], reported simulation results for films with thickness close to the skin depth which showed similar polarity for the square edge. It is interesting to see that for this case, MDM theory calculates resonances at much lower wavelength than the simulation results.

3.6   Summary

A 3-micron-thick CMOS-compatible structured film comprising an array of metal squares, a dielectric spacer, and a metallic ground plane was demonstrated to provide 95% absorption for the fundamental band at 53.5 micron wavelength, with additional resonances appearing at shorter wavelength. These bands were observed to be only weakly dependent on polarization and incident angle. The number, center frequency, dependence on square dimension and dielectric thickness, and lack of dependence on period of the array are all well explained by a model in which the incident beam excites oscillating dipoles at the edges of the squares, which are sources for standing waves that occur in the sub-wavelength space beneath individual squares. The analytic model and physical interpretation of edge dipoles and standing waves are supported by numerical calculations, which give field visualization and spectral line shapes in agreement with experiment. These structures have application as a wavelength selective coatings for far-IR bolometers.

CHAPTER 4: OPTICAL SALISBURY SCREEN WITH DESIGN-TUNABLE RESONANT ABSORPTION BANDS

Wavelength-selective plasmonic and metamaterial perfect absorbers have been studied extensively for various applications. However, the emphasis has been on three-dimensional structures, which depend on numerical design and sophisticated fabrication techniques, such as electron beam lithography for in-plane patterning. Particularly in the visible and near-IR, nanoscale structures such as periodic nano-discs [9], squares [41, 42, 50], metallic gratings and trapezoids [86], and split ring resonators [87] have been investigated. However, for visible and near-IR region the structures sizes are too small for low cost fabrication. This work presents experimental characterization of an efficient selective absorber formed by three simple layers without any in-plane patterning at all.

4.1   Introduction

Triple-layer structure composed of conductor-dielectric-conductor also known as a *Salisbury screen* at radio wavelengths has been used to reduce radar cross-sections for military applications [22,23]. The Salisbury screen was invented by Winfield Salisbury in 1952. It was used in sleath technology as a radar absorbing material. High absorption of radar prevents detection of the object because of reduced intensity of the reflected light. A salisbury screen absorber consists of 3 layers such as a partially reflecting material at the top, a quarter-wavelength-thick ($\lambda/4$) lossless dielectric, and a perfectly reflecting ground plane. The working principle of salisbury screen is similar to the concept of a Fabry-perot cavity. Up on incidence of coherent light on the absorber, the top layer partially reflects while the transmitted light travels through the dielectric. The gound plane reflects the transmitted light back thought the dielectric which again partially transmits through the top layer. Thus reflected light from the top surface and the ground plane interfere. A destructive

52

interence will force light to be trapped inside the dielectric in multiple reflections and eventually be absorbed due to dissipation. By carefully choosing the reflectivity of the top layer perfect absorption can be achieved. The absorption can be tuned by adjusting the thickness of the dielectric.

Adaptation of this technology to visible and near-IR wavelengths has been investigated theoretically by Shu et al. [25]. Unlike metamaterial absorbers, the device consists of unpatterned thin metal and dielectric films, which can be fabricated by any suitable means of blanket deposition. On the other hand, a possible disadvantage is that this type of absorber is 3 to 10 times thicker than previously reported metamaterial absorbers [9, 41, 42, 50]. In principle, freedom from lithographic patterning enables application to arbitrarily large areas by wet chemical methods. The resonant absorption occurs in multiple bands because of light trapping in the Fabry-Perot cavity. The resonance wavelength depends on the thicknesses of the dielectric spacer and the top metal, while the deposited thickness of the latter strongly controls the resonance width without significantly affecting the absorption strength.

For applications, there has been significant effort to broaden the absorption in resonant plasmonic/metamaterial nano-structures [41, 86, 87]. Ref. [41] used a multiplexed periodic checkerboard of metal squares to achieve 200 nm absorption band width at 3.45 μm wavelength. Ref [87] employed crossed gratings and trapezoid structure to achieve 250 nm band width in the visible. Ref [86] investigated split ring resonators (SRR) to realize 800 nm band width at 1.3 μm wavelength. All structures required electron beam lithography, which is unsuited for large areas or mass production.

A non-lithographic approach to broad absorption was presented in [88], where nano-composite SiO_2 / Au films were co-evaporated. Strong absorption was achieved from 400 to 800 nm wavelength. However, the design-tuning range realized by changing the volume fraction of metal was only 100 nm.

In contrast to the metamaterial and composite approaches, the simple three-layer Salisbury screen presented here provides a wide range of possible center wavelengths and absorption widths, simply by changing the thicknesses of the depositions. Yet all investigated variations maintain a peak fundamental absorption of at least 93% and up to 97%. No sophisticated lithography is required. In principle, low-cost wet chemical deposition could replace vacuum methods to achieve large area coverage.
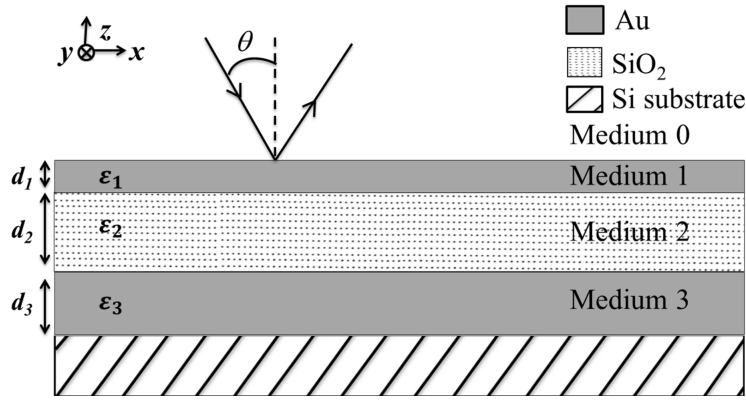
Figure 4.1: Schematic diagram of the triple-layer metal-dielectric-metal absorber.

4.2 Theory

Fig. 4.1 represents a schematic of the 3-layered metal-dielectric-metal absorber, whose reflectance is [25]

$$R = |\frac{1}{r_{01}} + \frac{r_{01} - \frac{1}{r_{01}}}{\frac{r_{01}}{\phi} + 1}|^2 \tag{4.1}$$

where

$$\phi = \frac{1 - r_{12}^2 e^{2ik_{2z}d_2}}{r_{12}(1 - e^{2ik_{2z}d_2})e^{2ik_{1z}d_1}} \tag{4.2}$$

and $r_{i,i+1}$ are the angle- and polarization-dependent Fresnel amplitude reflection coefficients for light travelling from medium i to medium $i+1$. Thicknesses d_i and relative permittivities ε_i are as indicated in fig. 4.1. The normal component of the wave vector in medium i is,

$$k_{iz} = \frac{2\pi}{\lambda}\sqrt{\varepsilon_i - sin^2\theta} \tag{4.3}$$

where θ is the angle of incidence on the top layer and λ the free-space wavelength. Light that is partially reflected at the semitransparent medium 1 interferes with light that makes a round trip through medium 2 and is again transmitted by medium 1. The condition of destructive interference places a node at medium 1, which is the same condition as for resonant light trapping with multiple reflections inside the dielectric of a Fabry-Perot cavity. The trapped energy is consumed by losses in the three media, where the dissipated energy density is proportional to the frequency, to the imaginary part of the permittivity, and to the square of the amplitude of the electric field [89]. This absorption mechanism for Fabry-Perot type metamaterial absorbers has also been described by Hao et al. [33].
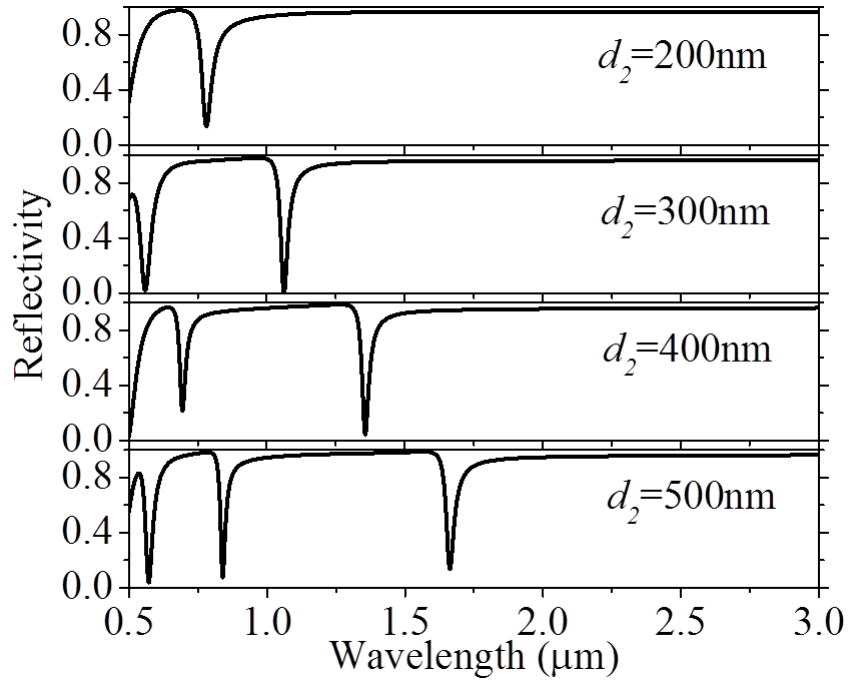
Figure 4.2: Calculated reflectivity (R) as a function of dielectric thickness d_2 for d_1 = 20nm.

Fig. 4.2 presents calculated reflectivity spectra at normal incidence according to Eq.4.1. The relative permittivity of bulk Au and SiO_2 are taken from reference [79, 90]. As the oxide thickness is increased, the fundamental resonance red shifts, and higher order resonances enter the spectral range. The resonance line width is independent of the oxide thickness, but the depth of the fundamental is dependent. The highest absorption of 99.99% occurs for d_2 = 300 nm.
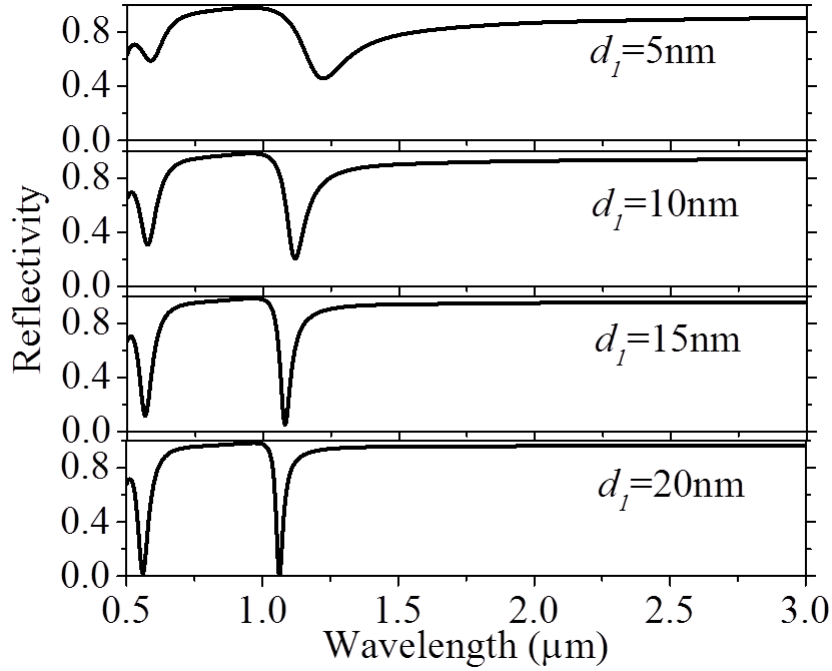
Figure 4.3: Calculated reflectivity (R) as a function of top metal thickness d_1 for dielectric thickness $d_2 = 300$ nm.

Fig. 4.3 presents the dependence of calculated reflectivity spectra on the thickness of the top gold layer (d_1). As d_1 decreases, the resonance red shifts and broadens and strength of absorption decreases. However, much larger red shifts and broadening are experimentally observed than predicted by these calculations. And, interestingly in the experiments there is little change in the absorption strength for change of top gold layer (d_1) from 20-10nm on contrary to these calculations (Fig. 4.3). The reason for the large red shift and strong broadening in experiments than theory is that the bulk permittivity values used here for the top gold films are inaccurate for very thin films, which are discontinuous. The observed length scale of the discontinuities is much less than our shortest wavelength (Fig. 4.4), so that macroscopic electrodynamics holds with an

appropriately averaged permittivity, and we may neglect scattering.
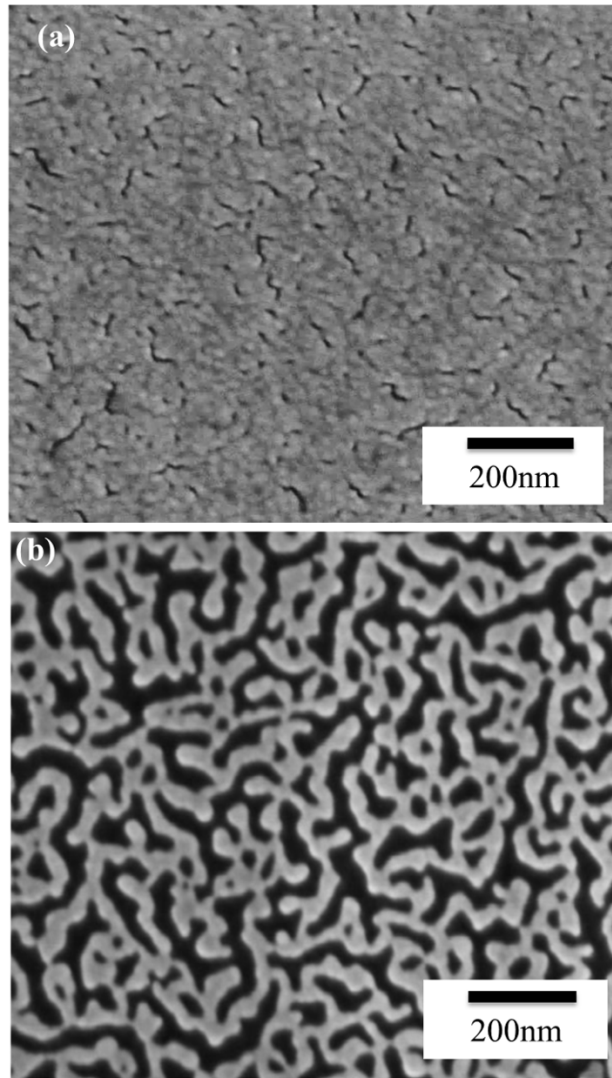
Figure 4.4: SEM images of (a) 20- and (b) 10-nm-thick gold films.

The averaged permittivity is found by effective medium theory [53, 54], where the Maxwell-Garnett approximation (MGA) [53] and Bruggeman effective medium approximation (EMA) [54] are the most commonly used formalisms. The latter is preferred for our films since

MGA assumes a dilute system of non-interacting isolated nanoparticles [54, 55]. For normal incidence, we approximate our system as a 2-dimensional array of flat circular plates. Using eq. 2.8 the effective permittivity is [55]

$$\varepsilon_{eff} = s \pm \sqrt{s^2 + \varepsilon_{Au}} \qquad (4.4)$$

where, $s = (1 + \varepsilon_{Au})/2 + f(1 - \varepsilon_{Au}) - 1$, f is the volume fraction of gold, ε_{Au} is the complex frequency-dependent permittivity of bulk gold, and the permittivity of air has been taken to have the value unity [55]. Positive or negative roots in Eq. (4.4) are chosen based on the physical requirement that $\text{Im}(\varepsilon_{eff}) > 0$ always. For $f > 0.5$, $\text{Re}(\varepsilon_{eff}) < 0$, though its magnitude is smaller than that of the bulk metal. For the films with f = 0.85 and 0.54 studied here, over our spectral range, the $\text{Re}(\varepsilon_{eff})$ is smaller than for bulk by factors of 1.4 and 25 at 2.5 microns wavelength, respectively. The $\text{Im}(\varepsilon_{eff})$ is smaller than for bulk by factors of 1.5 and 3 respectively, except in the short wave part of the spectrum where it is actually larger than for bulk when f = 0.54.

Fig. 4.5 presents real and imaginary parts of the effective permittivity for gold-air composite films having gold area fractions f = 0.54 and 0.84 calculated according to Eq. 4.4. These values are close to those determined for the discontinuous gold films used in our experiments (Fig.4.4). For the smaller area fraction, the real part reaches a value of only about -20 at 3 microns wavelength, and it's magnitude is everywhere smaller than the imaginary part. For the higher area fraction, the imaginary part has a minimum value at about 700 nm wavelength.
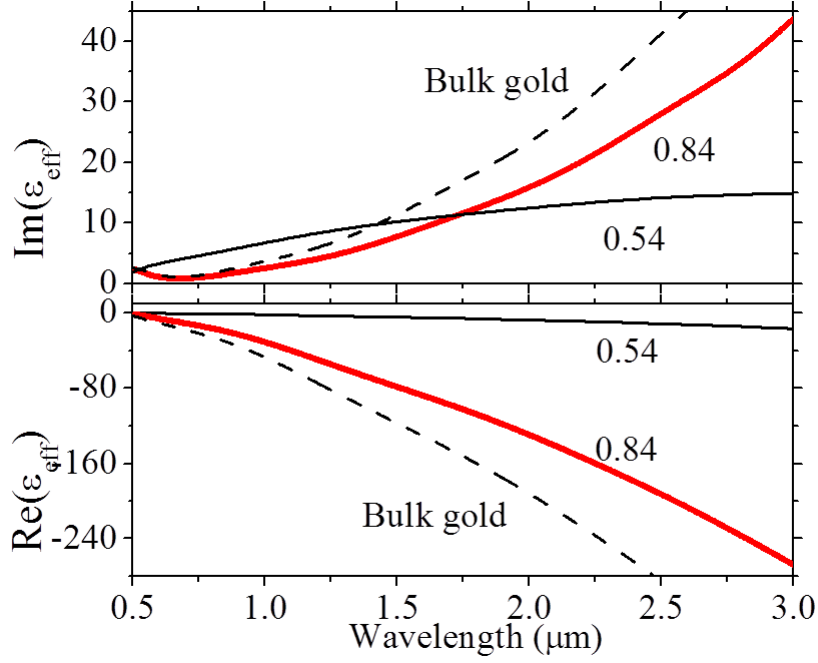
Figure 4.5: Calculated effective permittivity of the discontinuous gold films for d_1=10nm (black-line) and d_1=20nm (red-line)

For non-normal incidence, the thickness of the metal becomes important due to shadowing of the open gaps in the film. This effect can be accounted for by increasing the gold fraction f in the calculations. This is clear if one considers grazing incidence where the beam skims the top surface of the gold while the open spaces remain hidden (fig. 4.6). A very simple 1D model of the decrease for rectangular gaps in their apparent volume caused by hard shadowing, which ignores the semi-transparency of gold at the thicknesses considered, gives

$$f(\theta) = f_0 + \frac{d_1(1-f_0)tan\theta}{2a}(tan\theta < a/d_1) \tag{4.5}$$

$$= 1 - \frac{a(1-f_0)}{2d_1 tan\theta}(tan\theta > a/d_1) \tag{4.6}$$

where f_0 is the apparent volume fraction at normal incidence, and a is the characteristic size of the gaps.
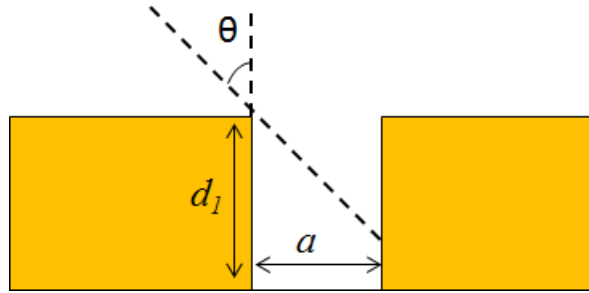
Figure 4.6: Schematic model of angle dependent porosity. $f(\theta)$ changes with angle because of the decrease in rectangular gaps in their apparent volume caused by hard shadowing.

4.3   Experimental Details

To fabricate devices, a 150 nm layer of gold was deposited by electron-beam evaporation on a Si substrate with a 10 nm Cr sticking layer. SiO_2 dielectric was deposited by plasma enhanced chemical vapor deposition (PECVD) from a liquid Tetraethyl-orthosilicate (TEOS) source. PECVD oxide and gold stick well without Cr. The thickness of the PECVD oxide film is determined from interference fringes measured in reflectance using a UV-Vis-NIR Cary500i spectrometer before the top metal deposition. The thin top layer of gold was deposited by DC sputtering, with thickness determined from the sputtering time, which was calibrated by step profilometry. Atomic Force Microscopy (Digital Instruments Dimension 5000U) was used to characterize the final surface roughness of the structures (fig. 4.7, 4.8). Specular reflectance at near normal incidence was measured using a BOMEM DA8 Fourier spectrometer with Si (visible) or InSb (near IR) detectors, quartz or KBr beam splitters, and quartz-halogen or globar sources, respectively. Angle dependent

specular reflectance was measured using the Cary500i UV-Vis-NIR spectrometer. Reflectance (R) is obtained by dividing the raw reflected power spectrum from the sample with that from a freshly-evaporated, optically-thick silver film on an optically-polished flat. The initially focused incident beam of the spectrometer is collimated by a concave mirror and is incident on the sample at an angle of 8 deg using a mirror assembly. Reflected light is finally diverged at the appropriate acceptance angle to the detector collection optic by another concave mirror. The absorptance $A = 1 - R$, since transmittance $T = 0$, and we neglect scattering. The volume fraction of gold for the films, and characteristic dimension of the inhomogenities, are determined from scanning electron microscope images using imageJ software [91].
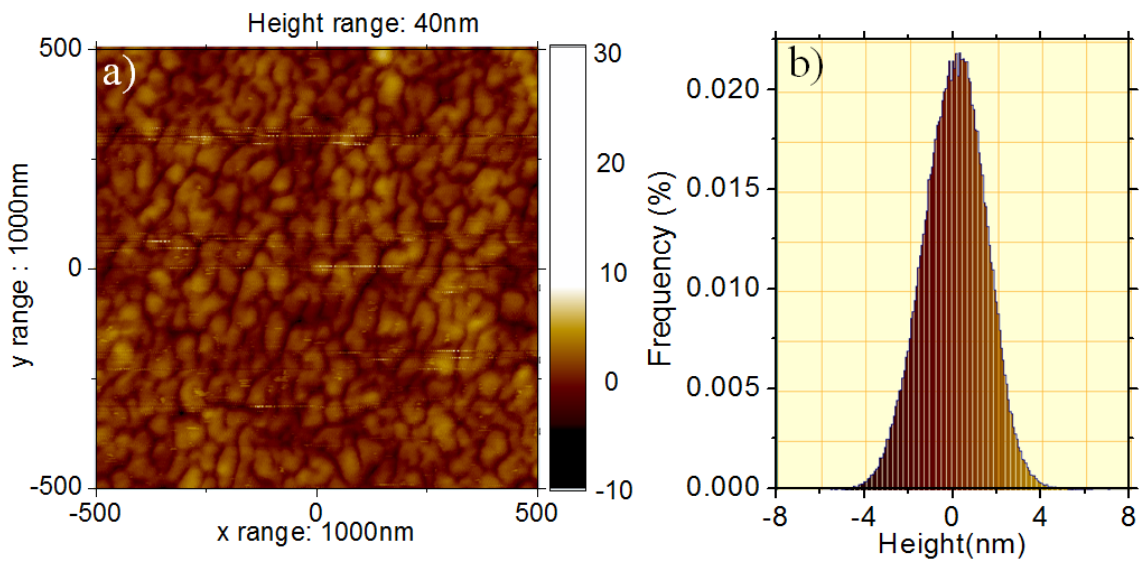
Figure 4.7: AFM image of sample with d_1=10nm a) topographical image, b) height histogram

4.4   Results and Discussion

Fig. 4.4 presents SEM images of two different preparations of the top gold film. Bright parts of the image are gold and dark parts are subsurface SiO_2. As thickness decreases, the film becomes more and more discontinuous. ImageJ analysis of 20 nm thick gold films gives a value for the gold volume fraction $f = 0.85 \pm 0.05$, where f is determined by the ratio of extreme dark and bright areas of the image and the uncertainty comes from setting thresholds for brightness and contrast. For the 10 nm film, we find the area fraction $f = 0.54 \pm 0.01$. The uncertainty is smaller here due to higher image contrast. Atomic force microscopy images collected over a 1 micron x 1 mocron area reveal similar characteristics of the films. Fig. 4.3 represents height profile of a 10nm thick Au film which is discontinuous.

Fig. 4.9 compares experimental and theoretical (Eq. 4.1) reflectance spectra, both for 8 deg angle of incidence. Calculations performed at 0 and 8 deg angle of incidence are indistinguishable in comparison to the measurement uncertainties. Resonance peaks at these two angles differ by less than 0.003 μm wavelength, or 0.27%, for all sample conditions. The experimental spectrum was measured for an unpolarized beam, and the calculations plotted are an equally weighted average of TE and TM polarizations.

A number of trends are clear for calculated spectra that assume bulk permittivity values (dotted curves) [90]. As the oxide thickness d_2 is increased, the fundamental resonance red shifts, and a higher order resonance enters the spectral range. The resonance line width is independent of the oxide thickness, but the depth of the fundamental is dependent. As top metal thickness d_1 decreases, the resonance red shifts and broadens modestly, and strength of absorption decreases significantly.

Fig. 4.9(a) and (b) compare reflectance spectra for absorbers with $d_1 = 20$ nm and $d_2 = $

203 or 320 nm, respectively. The positions and widths of the resonances calculated without EMA (black dotted line) agree poorly with experiment. The agreement is much better when the EMA permittivity is used (gray dotted lines) with $f = 0.84$ and 0.81 for samples with $d_2 = 203$ nm and $d_2 = 320$ nm, respectively. The f values that gave best fit to the experimental reflectance spectra agree with the f value determined from the SEM image (Fig.4.4) within the uncertainty.
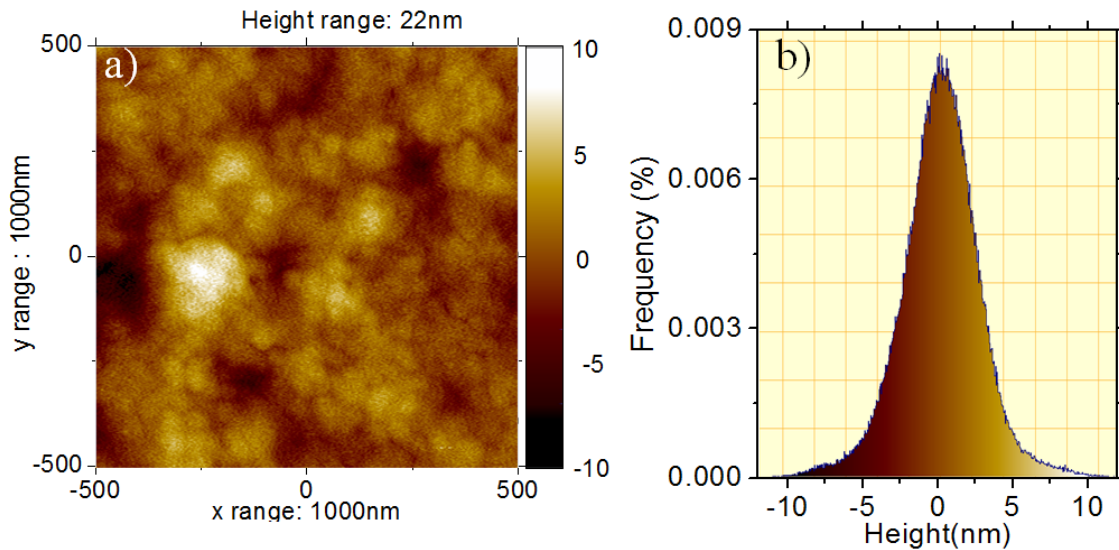
Figure 4.8: AFM image of sample with d_1=20nm, a) topographical image, b) height histogram

Fig. 4.9(c) and (d) present reflectance spectra from samples with $d_1 = 10$ nm and $d_2 = 172$ and 320 nm, respectively. Peaks are significantly broadened and red-shifted compared to the $d_1 = 20$ nm data by much more than predicted by theory based on bulk permittivity, while the decrease in peak absorption is much less. However, EMA permittivity values from Eq. 4.4 with f values as indicated in the plots give good match between theory and experiment. These fit values for f agree with the value determined from image analysis (Fig. 4.4.b) within the uncertainty, even though this uncertainty is smaller for this film. For the sample with $d_1 = 20$ nm and $d_2 = 320$ nm,

the fundamental is at $1.14 \mu m$. Its 93% peak absorption is maintained when d_1 is halved, but the wavelength range over which the fundamental absorption exceeds 90% becomes 50 broader. For the sample with $d_1 = 20$ nm and $d_2 = 203$ nm, the experimental fundamental absorption at 0.81 μm wavelength is 97% deep.
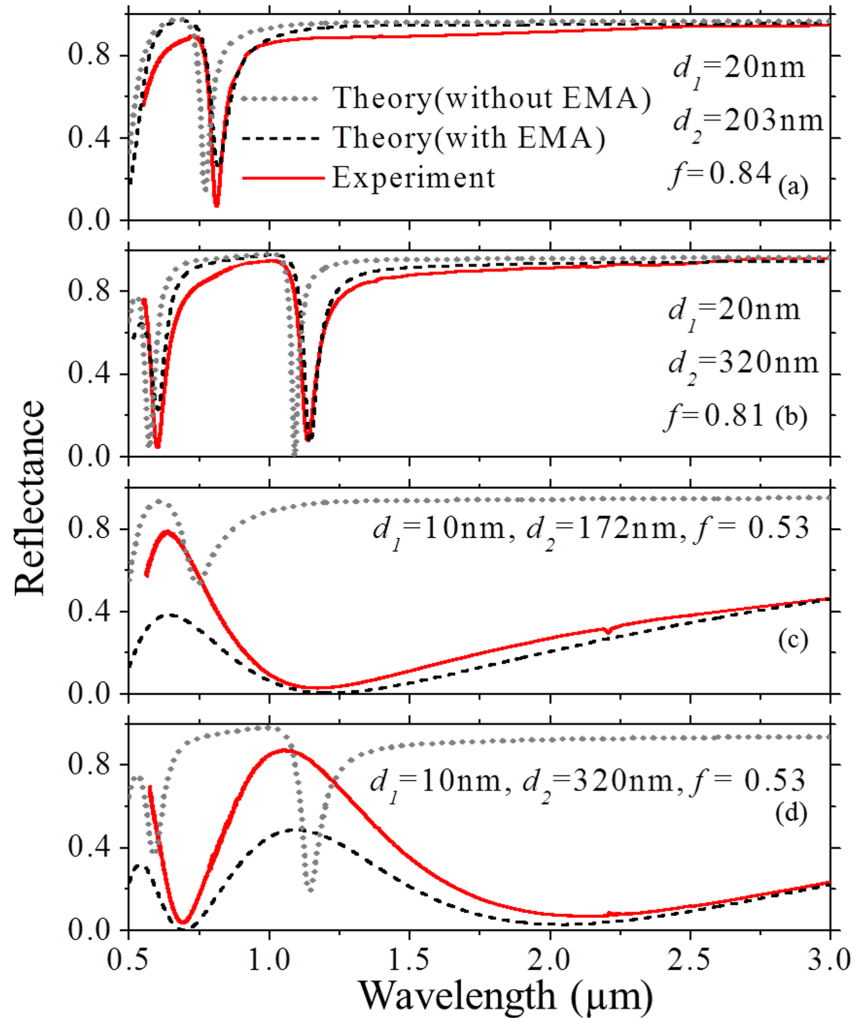
Figure 4.9: Reflectance spectra for samples with d_1 and d_2 values as indicated. Calculations based on bulk or EMA permittivity values are compared to experiment for 8 deg angle of incidence.

Fig. 4.10 presents angle dependent reflectance spectra with TM and TE polarizations for two of our samples. In comparison with Fig. 4.9, the spectral range is somewhat shorter on the long wave side due to the limitations of the different spectrometer used. Resonances are observed to red shift with increasing angle. The degree of agreement between theory and experiment is comparable to that in Fig. 4.9. As in that case, the single parameter used to match the theory to the experiment was the gold volume fraction f. It was necessary to treat the apparent gold fraction f as being angle dependent. This parameter is varied manually until the shape and position of the resonances simultaneously agreed as closely as possible to the experimental result, as judged by eye.

The f values that gave the best fit are plotted vs angle in Fig. 4.11 and compared to curves obtained from Eq. 4.6. The gap sizes a were determined from ImageJ to be 37 and 13 nm for $d_1 = 10$ and 20 nm, respectively. The normal-incidence f_0 values used in Eq. 4.6 were those determined from the SEM image, namely 0.54 and 0.85, respectively. For the 20 nm thick top-layer, the very simple model for apparent gold fraction appears to work fairly well. At the highest angle of incidence, the apparent volume fraction is nearly unity, so that the permittivity approaches that of bulk gold.

For the 10 nm thick top-layer, the model curve is 2-10% higher than the best-fit values. Perhaps here the neglected semitransparency of the gold becomes more important. Alternatively, the difference might be attributed to uncertainty in measured film parameters. For instance, by increasing the experimental value of the gap size a by just a few percent, the curve shifts downward sufficiently to considerably improve the agreement.

66
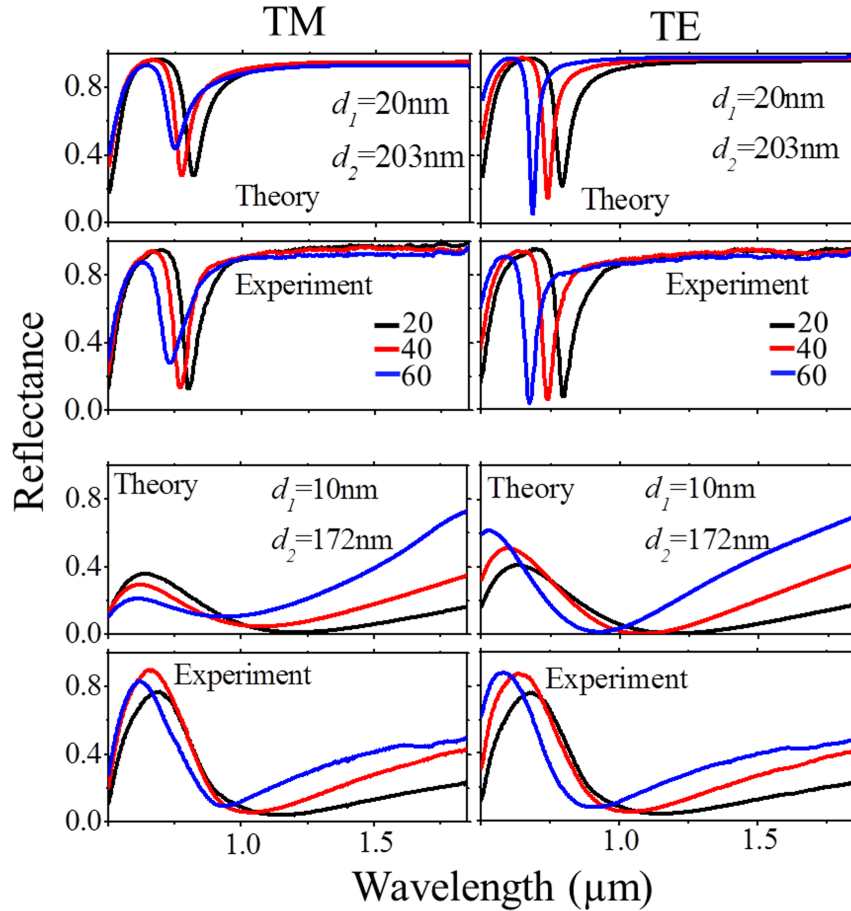
Figure 4.10: Angle- and polarization-dependent reflectance spectra. The top (bottom) four plots correspond to thicknesses d_1=20 nm and d_2=203 nm (d_1=10 nm, d_2=172 nm). The left (right) column of plots is for TM (TE) polarization. Theory and experiment are as indicated. All resonances shift to longer wavelength as angle of incidence is increased in the sequence 20, 40, and 60 deg.

Numerical finite element time domain (FDTD) method, informed by 3D microstructure from Atomic Force Microscopy (AFM), might possibly provide a more accurate agreement with experiment and improved intuitive understanding. However, typical AFM tips would have difficulty navigating the deep narrow gaps in our surface films [92], so that obtaining accurate 3D

morphology would be a challenge. Indeed, AFM measurements on our samples show height histograms with a single peak having a width that indicates a surface roughness of 2 nm, which is the same as that of the commercial polished Si substrate.
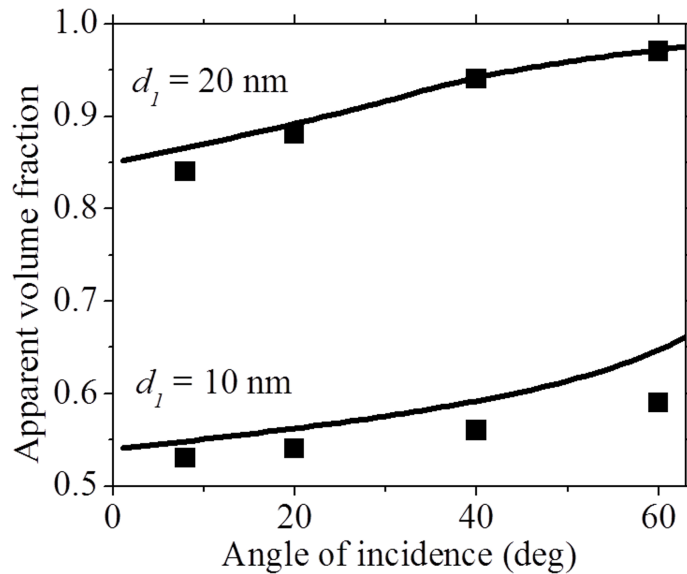
Figure 4.11: Apparent gold volume fraction as function of incidence angle. Calculated values are presented by solid lines. Values used to fit the experimental reflectance spectra are given as symbols.

Rapid design is well served by simple analytic models. All wavelengths considered are at least 10x longer than any microstructure, so we are clearly in the regime of macroscopic electrodynamics, in which optical properties are determined by an appropriately-averaged permittivity. The simple effective permittivity described here, with the resonance theory of Shu et al., predicts with remarkable accuracy the positions, widths, and peak strengths of the absorption resonances. However, the model tends to over-estimate the absorption between the resonances.
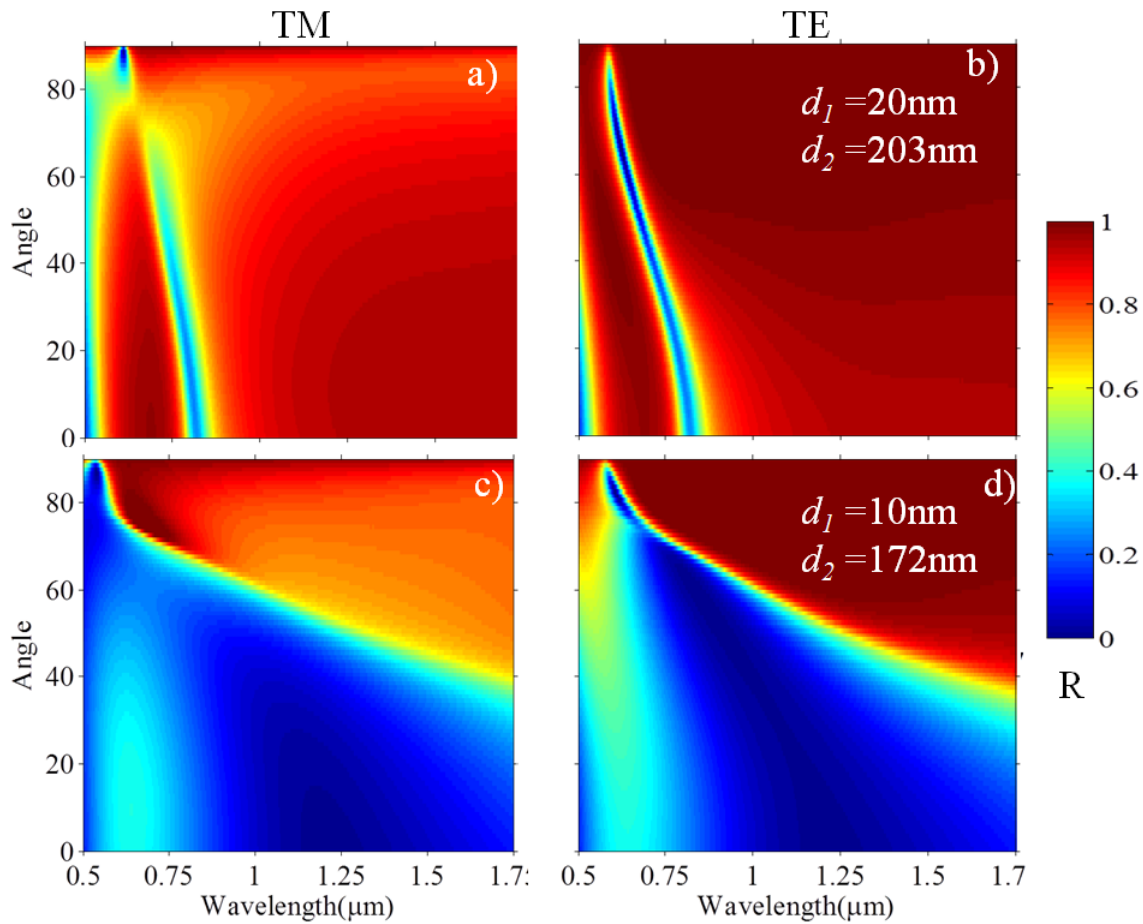
Figure 4.12: Reflectance as a function of angle modeled according to eq. 4.1, 4.4 and 4.6. Sample parameters are indicated in the right side of the figures.

Fig. 4.12 represents numerically calculated reflectance spectra as a function of angle of incidence both for TE and TM polarization. The calculation is performed using eq. 4.1, 4.4 and 4.6. Theory takes care of angle dependent roughness of a realistic sample and calculated reflectance using effective medium approach. The top (bottom) four plots correspond to thicknesses d_1=20 nm and d_2=203 nm (d_1=10 nm, d_2=172 nm) similar to fig. 4.10. With increase in angle of incidence,

the resonance wavelength blue-shifts and the bands become sharper for both samples.

For sample with d_1=20 nm and d_2=203 nm, there is 33% of blue shift in the resonance wavelength. For TE polarization the resonance strength weakens with increase of angle, at 70 degrees there is little absorption. At 90 degrees, there is a mode at 600nm. For the TM mode, the fundamental mode at 800nm blue shifts by 33% while the resonance strength increases and becomes maximum at 70 degrees and reduces to zero strength at 90 degrees.

Fig. 4.12(c-d) represents angle dependent reflectance for TE (c) and TM (d) polarization with sample parameters of d_1=10 nm and d_2=172 nm. The resonances blue-shift, and change in band-with is more dramatic as compared to the previous sample (4.12(a-b)). Resonance wavelength blue shifts from 1250nm to 600nm for change in angle of incidence from 0 to 90 degrees. The blue-shift is more than 50%. The resonance bandwith decreases by more than 90% for the same change in angle. The resonance strength remains strong up to 70 degrees for both polarization. Both TE and TM polarization produces similar absorption bands for this sample. The trend of reduction in absorption band width can be explained from dependence of gold fraction in the top on angle of incidence. With increase in angle of incidence, fraction increases because of shadowing effect and becomes unity at 90. Thus for higher incidence angle, the top gold film behaves more like a continuous film and produces sharper resonances.

4.4.1   Metal Nano-discs

Au nano-discs

SiO$_2$

Au

Subsrate
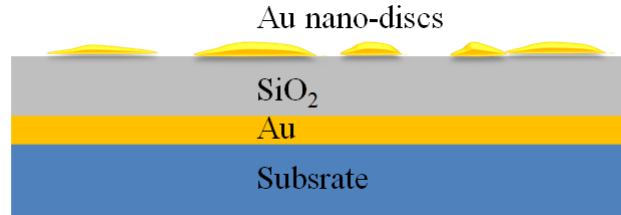
Figure 4.13: Schematic diagram of triple layer absorbers with Au nano-discs

Experiments were also done using Au nano-discs instead of thin films on top for such 3-layer absorbers which produce similar absorption bands. Such absorbers with metal nano-particles and nano-discs were reported with triple layer metamatertial structure producing perfect absorption in the visible [88, 93, 94]. Fig. 4.13 represents an absorber with metal-dielectric-metal-nano-discs structure. These absorbers are reported for lithography free, large area producible and thermally stable visible/ near -IR absorber for potential use in solar energy harvesting. The absorption mechanism is explained to be plasmonic enhancements and magnetic resonances [88, 93, 94]. We show that these absorption bands are simple fabry-perot cavity resonances. We explain such absorption using eq. 4.1 and effective medium approaximation. Although plasmonic resonances might be present in the Au nano-discs, we show that the main effect responsible for such absorption is Fabry-perot cavity.
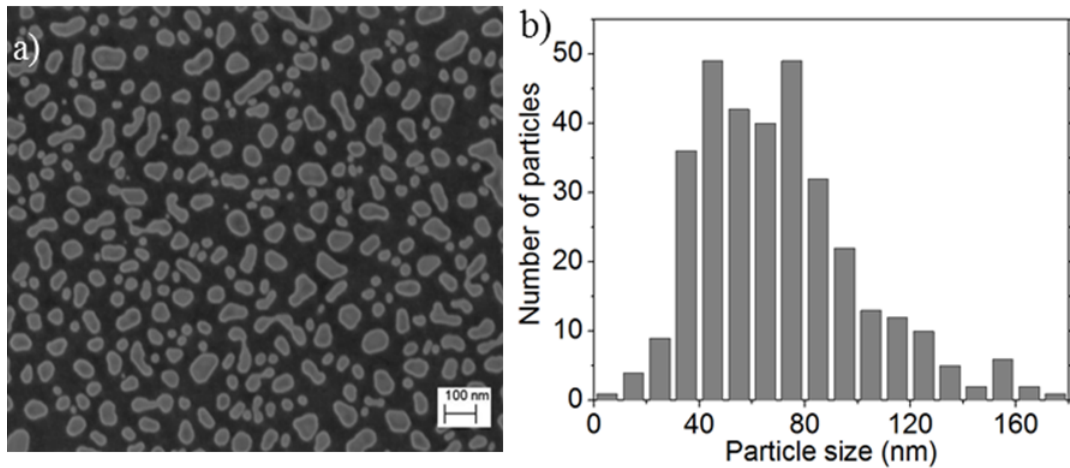
Figure 4.14: Scanning microscope images of gold nano-islands on oxide for a sputtered gold film d_1= 10 nm. The films was annealed at 300^0C for 24 hours. Particle size distributions are plotted adjacent to the SEM image.

Fig.(4.14.a) presents an SEM image of the gold nano-discs film. Such nano-discs are formed by annealing thin gold films. The films are deposited by DC sputtering with thickness of 10 to 30nm. The bar graph in Fig.(4.14.b) represent the island size distribution which is estimated by ImageJ analysis. The peak of the distribution depends on the initial thickness of the gold film before annealing to form islands. Size of the nano-discs depends on thickness of the films. Annealing is done at 300^0C for 24 hours. When the thickness of Au film is 10 nm, the average particle size is 71.5 nm. When the film thickness was 30 nm, the average particle size is 282.3 nm. When the film thickness is more than 30 nm, annealing does not produce such nano-discs.

Fig. 4.15 shows reflectivity spectra from a 3-layer sample with Au nano-discs in the top surface. Thickness of the SiO$_2$ dielectric spacer layer is d_2= 70nm. The thickness of the top Au layer before annealing was 10 nm which is similar to a film shown in fig. 4.4.a with area fraction

f=0.53. After annealing at 300_0C for 24 hours, the discontinuous Au film becomes randomly oriented Au nano-discs as shown in fig. 4.14.a. ImageJ particle analysis gives f=0.39. After annealing the area fraction is reduced from 0.53 to 0.39. Where does the gold go!? This happens because of change in structure of the Au film from network structure to hemispherical Au nano-discs. Thus the thickness of the Au nano-discs can be determined from change in the area fraction as $f_{initial} \times d_{inital} = f_{final} \times d_{final}$. Hence $d_{final} = \frac{0.53 \times 10}{0.39} = 13.6$ nm. The average particle size is 71.5 nm as shown in Fig.(4.14).a. Thick lines represent reflectance spectra from samples with gold nano-islands, while dashed lines represent spectra calculated using eq. 4.1 with EMA approaximation.
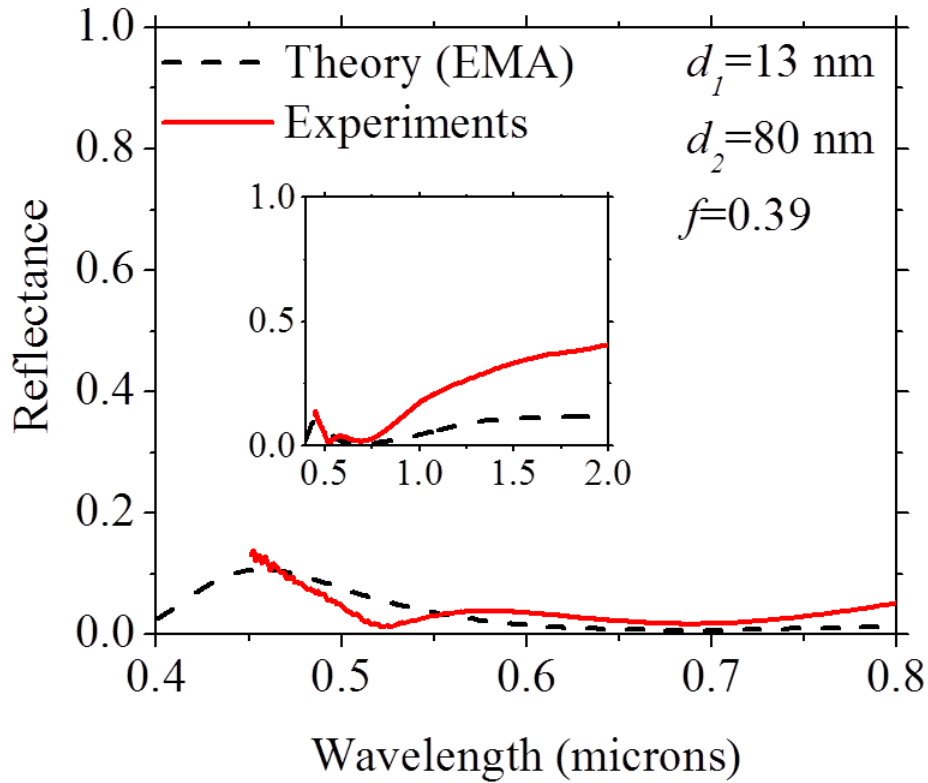
Figure 4.15: Reflectivity spectra from a 3-layer sample with Au nano-discs in the top surface. The average particle size is 71.5 nm as shown in Fig.(4.14).a. Thick lines represent reflectivity spectra from samples with gold nano-islands, while dashed lines represent spectra calculated using eq. 4.1 with EMA.

Inset in fig. 4.15 shows theoretical and experimental spectra from 0.45 to 2 microns for a sample with parameters d_1=13.6nm and d_2=70nm and f=0.39. Peak absorption of 98% is obtained at 0.7 microns for the experimental spetrum with strong wide band absorption of more than 90% from 0.45 to 0.7 microns. Thoery using EMA is able to explain such absorption pretty well in the visible. From 0.8 to 2 microns, thoery shows higher absorption than experiments. At 2 micorns, experimental absorption is 60% while theoretical absorption is 90%. This might be

because our theory is not able to consider different geometries of the nano-structures. Trial of Maxwell-Garnet approximation leads to even worse prediction due to higher volume fraction of the nano-structure. However, theory predicts resonance wavelength and line shape in the range from 0.45 to 0.7 microns pretty well.

Fig.(4.16)(left) presents reflectance spectra for the near-UV and near-IR samples. For the near UV sample (d_1=13.6 nm,d_2=30 nm,and f=0.39) absorption peaks at 95% for 360 nm wavelength. Reflectivity spectra of samples without gold nano-islands are represented by thinner lines in fig.(4.16), and both samples reveal thin film interference pattern. With the addition of the gold nano-disc films these band strength increases. Trapped light is wave-guided in the film and dissipates into heat. Despite gold being partially transparent in UV, Fabry-perot mechanism of absorption occurs in UV with gold nano-discs. Fig.(4.16)(right) present reflectivity spectra for near-UV and near-IR samples for different angles of incidence from 20 to 50 degrees. Strong absorption is sustained to wide angle of incidence and the absorption blue shifts as this angle is increased which is in agreement with our theory.
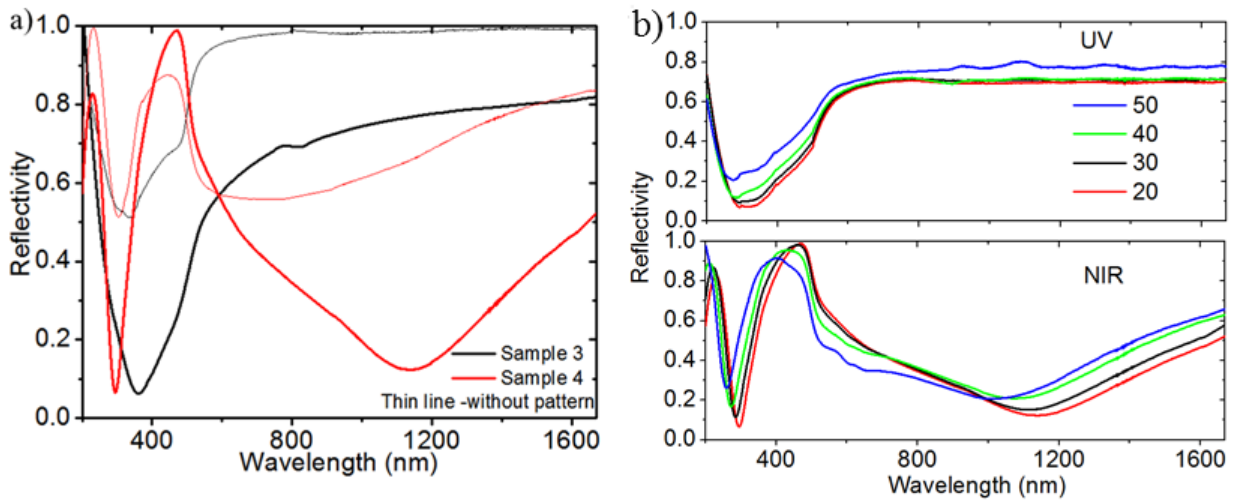
Figure 4.16: (a) Reflectivity spectra in near-UV and near-IR. Thick lines represent reflectivity spectra from samples with gold nano-islands, while thinner lines represent spectra from samples without the gold nano-islands. (b) Reflectivity spectra with varying angle of incidence, as indicated in deg in the legend.

4.5   Summary

One of the primary objectives of this work was to experimentally test the predictions of the analytic theory presented recently by Shu et al. [25]. When the deposited thickness of our top-layer metallization is at least 20 nm, the film is more or less continuous, and theory agrees fairly well with experiment. On the other hand, for thicknesses much below 20 nm, the discontinuities in our films become significant, such that the theory of [25] is inapplicable. In fact, experiment then differs very strongly from that theory.

A second objective of this work was to extend the theory of [25] to the case of discontinuous top metal films. Our hypothesis is that the theory will work if the discontinuities are smaller than the wavelength, such that macroscopic electrodynamics still applies, with suitable optical constants. We find that use of permittivity values obtained from effective medium approximation (EMA) [53–55] restores the substantial agreement with experiment, especially with respect to the wavelengths of the resonances, their widths, and their peak absorption.

It would be very interesting and useful for applications to extrapolate the optical Salisbury screen to mid- and long-wave infrared wavelengths. Such might use (e.g.) dielectric films of infrared-transparent glass such as AsSe [95]. Such an IR effort would be timely, as suggested by the recent demonstrations of the two-dimensional thin-film total absorbers n^+ Si on sapphire [96], heated VO_2 on sapphire [97], and Ge on n^+ Si [98].

In summary, a strongly absorbing optical Salisbury screen, based on metal-dielectric-metal resonator, has been experimentally demonstrated at visible and near-IR wavelengths. Maximum absorption was in the range 93 to 97% for all resonances. Experiments confirm the theory of Shu et al. [25], which we have successfully extended to the case of discontinuous top metal films by using permittivity values from effective medium approximation with input from microscopy. These absorbers require no in-plane patterning, yet give performance and design-tuning of resonance position and width comparable to much more sophisticated metamaterial absorbers. Hence, low cost fabrication over arbitrarily large areas may be achieved by wet chemical methods, in principle, i.e. as a wavelength-selective, ultra-black paint. Potential applications include cloaking of (e.g.) military targets that might otherwise be susceptible to laser-marked guided munitions.

CHAPTER 5: WIDE-BAND LONG-WAVE INFRA-RED (LWIR) METAL-DIELCTRIC-METAL THIN FILM ABSORBER

In this chapter, we discuss experimental result of a CMOS compatible thin metamaterial broadband absorber in the range from 8-14 microns (long-wave infrared, LWIR) with bands up to 98% absorption. The thickness of the absorber is only 1.3 microns which is 10 times smaller than the highest wavelength. LWIR range is important in IR detectors because IR radiation can travel greater distance without being absorbed by the atmosphere. The absorber has a 3 layer metal-dielectric-metal structure which is fabricated using vacuum deposition methods and standard photo-lithography. SiO_2 is used as the dielectric spacer which provide strong dispersion in the refractive index at ~ 10 microns to achieve multiple absorption bands. MDM cavity theory explains observed resonances. FDTD simulations are used to optimize design parameters for the absorber. Angle dependent reflectivity measurements confirm wide-angle absorption bands which weakly depends on polarization.

5.1   Introduction

Uncooled bolometers are resistive IR detectors which detect change in resistivity due to heat generation by IR radiation. Uncooled infrared detectors have recently gained wide attention for infrared imaging application, due to their several advantages such as low costs of fabrication, low weight, low power consumption, extended spectral response, and long-lasting operating capacity [47–49]. Microbolometers are most extensively used in uncooled infrared detectors because of their CMOS compatible processing. They are easy to be monolithically integrated with CMOS circuitry which has advantage of lower manufacturing costs. Highly efficient thin film IR absorbing coating is required for such absorbers. Thin metamaterial absorbers are studied for potential use in such

bolometers [11, 41, 50].
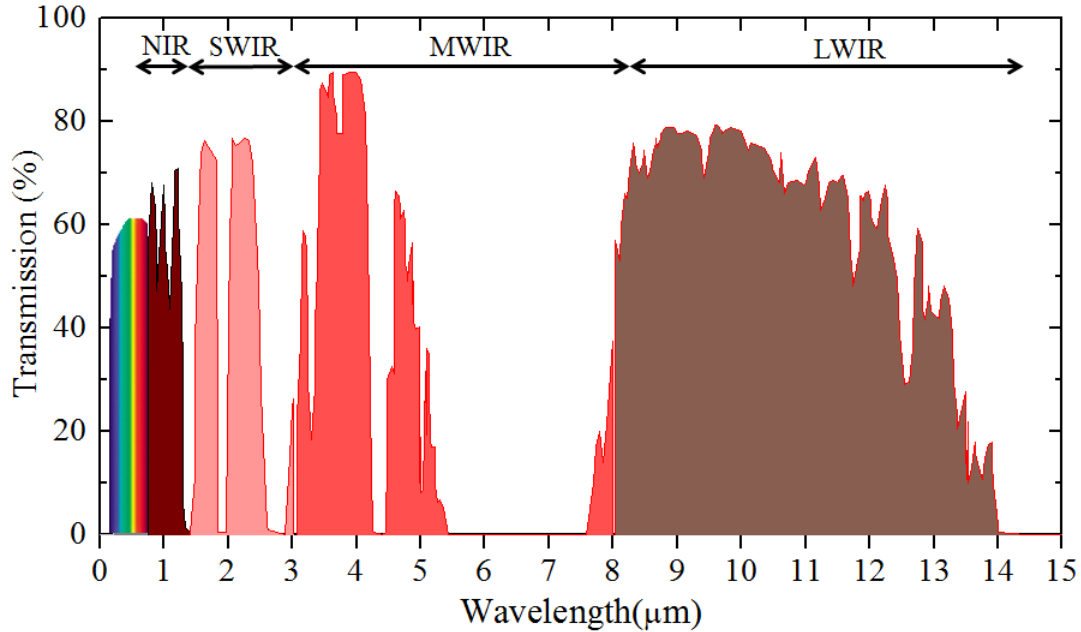
Figure 5.1: Atmospheric transmission of electromagnetic radiation from visible to infra-red.(Redrawn and modified from Wikipedia.org: Infrared Window.)

Atmospheric absorptions from molecules such as H_2O, CO_2, O_2, O_3 and NO allow only some parts of the electro-magnetic radiation to transmit. Fig. 5.1 represents atmospheric transmission measured from earth as a function of wavelength from 0.2 to 15 microns [99, 100]. There exist small transmission windows in the spectrum such as visible (0.4-0.7 microns), near-IR (1.5-1.55 microns), mid-IR (3-4 mcirons), and LWIR (8-14 microns) where electromagnetic radiation can travel longer distances. IR detectors aim to collect light in these windows.

LWIR from 8-14 microns is an important band in IR spectrum. First of all, atmosphere transmits very well in this range. Hence, the detectors in the this range have long distance vision.

Secondly, the peak of black body radiation spectrum of room temperature (298K) falls in this range. Earth is emitting IR radiation in this range which is useful for hyper-spectral imaging of earth and environmental monitoring [101]. In figure 5.2, the blue line represents black-body radiation at 298K. Red line in figure 5.2 is black-body radiation spectrum at 310K, the temperature of human body. For a 4% change in temperature (298K to 310K), there is 23% change in intensity in the black-body radiation spectrum. Because of the nature of black-body radiation, slight change in temperature above room temperature can be detected in this range.
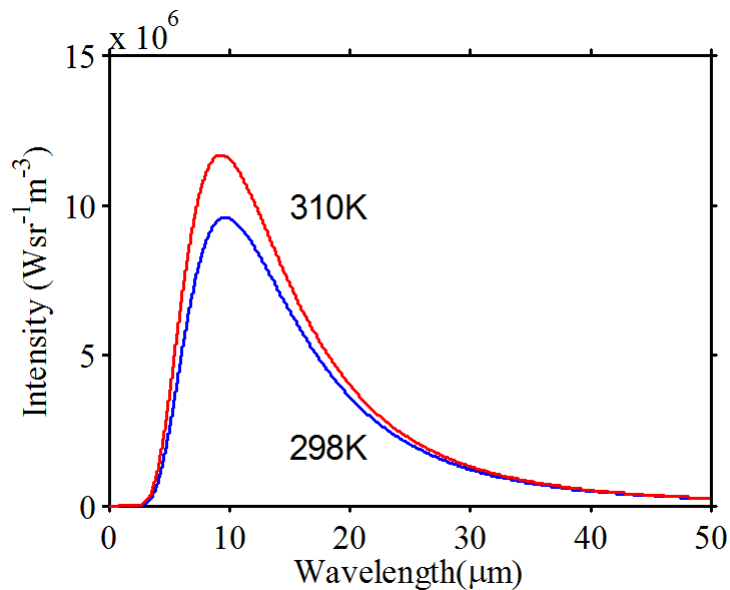
Figure 5.2: Black-body radiation at 298 and 300K temperatures according to Planck's radiation law.)

Metamaterial absorbers with thin layers of metal-dielectric-metal structure have been reported to produce polarization insensitive strong absorption with sharp bands over wide angles. However, obtaining broadband absorption for applications with such absorber has been a challenge so far. There are several intrinsically lossy materials which strongly absorbs IR light in broad-

band such as graphite, metal-black, carbon nanotubes etc. However, the deposited thickness of these materials to achieve strong absorption is very high such as 10-100 microns in the longer IR regions [13]. Such thick films become problematic to be used in detector pixel because of difficulty in patterning. Also, these materials are not design tunable and mechanically stable. Thin film wavelength-selective metamaterial absorbers have been studies widely for applications in such detectors [35, 41, 44]. Typically, metamaterial absorbers consists of a periodic metallic squares, a dielectric spacer layer and a metal ground plane as shown in figure 1.3. The resonance frequency depends on the size of the surface structures, thickness and refractive index of the dielectric [33, 60]. The resonant absorption typically has bandwidth less than 12% of the center frequency [50].

There has been several reports trying to achieve absorption in resonant metamaterial and plasmonic nano-structures in the near and mid IR [41, 61, 87]. However, most of the works has complicated structures which need electron beam lithography and only offers bandwith of upto 800nm [61, 87]. Such bandwidth can hardly be useful for real commercial detectors. Salisbury absorbers without photolithography for broadband absorption bands are reported in [63]. However, these type of absorbers show strong polarization and angle dependent properties. Also, for LWIR range, the thickness of the absorber has to be more than 2.5 microns which is much thicker for detectors [9, 33, 50].

We experimentally demonstrate a wide-band IR metamaterial absorber absorbing up to 98% of the incident radiation with a bandwidth from 8-14 microns. The absorber is a 3 layer structure of periodic squares of gold, SiO_2 dielectric spacer and a gold ground mirror. The absorber is 1.3 micron thick which is 10 times thinner than the operating wavelength. We show that the absorption bands are weakly dependent on polarization. Strong absorption is obtained up to 70 degrees of angle of incidence. No complicated structures are necessary for the absorber. Fabrication is done by standard photolithography which is also compatible with CMOS/MEMS processing.
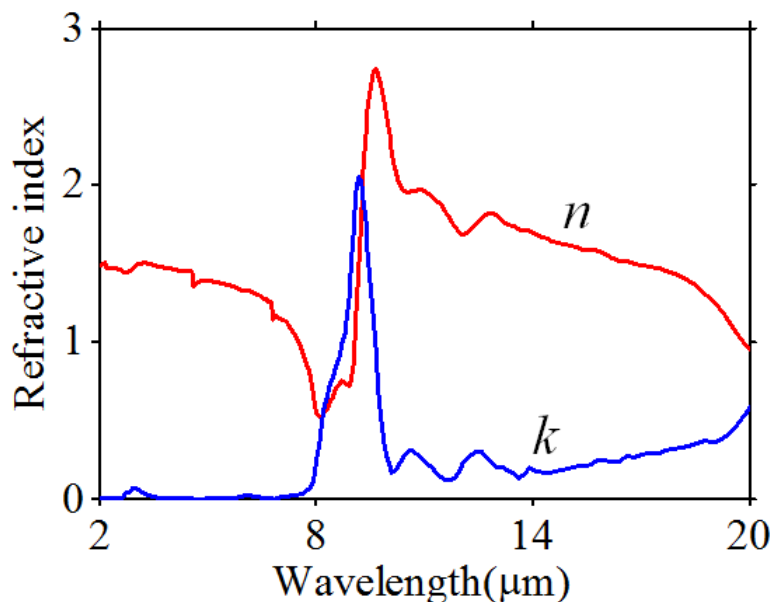
Figure 5.3: Black and red curves represent experimentally measured refractive index, n and absorption coefficient, k respectively as a function of wavelength for SiO_2 using a VASE IR ellipsometer.

Figure 1.3 presents a schematic of the considered structure. Gold is used as metal and silicon dioxide as the dielectric spacer. The absorber is designed according to the MDM cavity theory of far IR absorber presented in chapter 3. We use the same design principles but in the LWIR region. According to the theory, the absorption in such absorber occurs because of absorption of light in forms of standing waves in MDM cavities. The cavities can absorption in multiple bands. We showed that resonance wavelength depends on cavity size and the refractive index of the dielectric spacer. For the absorber in chapter 3, the operating wavelength was 20-80 microns. Two strong absorption bands were obtained which were identified as the $\lambda(1,0)$ at 53.5 microns and $\lambda(3,0)$ at 27.4 microns. For most of the operating wavelength region, the refractive index

of the dielectric spacer (SiO$_2$) remain more or less constant $n \approx 2$, except 20-25 microns region where SiO$_2$ dispersive. We showed that because of dispersive behavior of the dielectric there can be secondary absorption related to a mode. That is, one resonance mode can produce more than one absorption bands (fig. 3.2).
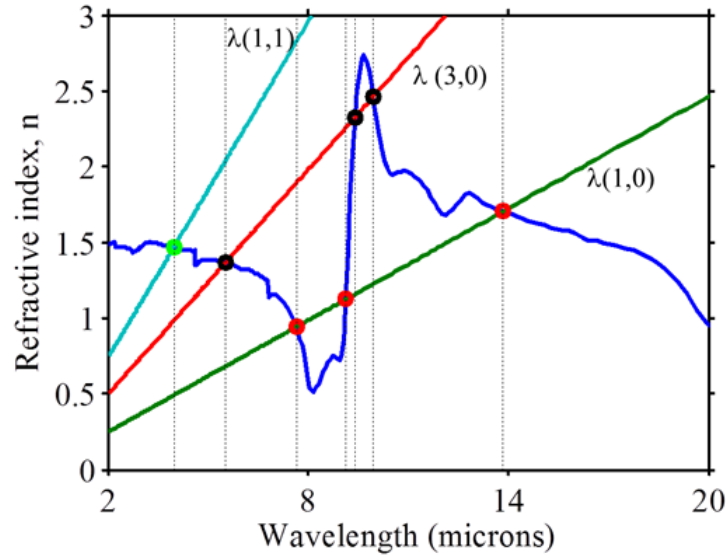
Figure 5.4: Graphical solutions for resonance wavelength for $\lambda(1,0)$, $\lambda(3,0)$ and $\lambda(1,1)$ as indicated for a sample with parameters t=1.3 microns and l=3.2 microns.

Fig. 5.3 represents experimental refractive index of SiO$_2$ used in our experiments. The complex refractive index was measured using a IR-VASE ellipsometer for a 1.4 microns thick e-beam evaporated SiO$_2$ film on a 200nm smooth gold film. Red and blue lines represent real part of the refractive index (n) and absorption coefficient (k), respectively.

In chapter 3, we have derived the resonance wavelengths for metamaterial absorption bands based on MDM cavity model. Eq. 3.3 calculates resonance wavelengths for a cavity with parameters square size (l), thickness (t) and refractive index $n(\lambda)$ of the SiO$_2$ dielctric spacer.

Multiple resonances are obtained for different values of (b, m) where m is the order of resonance, and b is the possible odd number of reflections from top and bottom metal layers (see fig. 3.1). In chapter 3, we showed that the resonance wavelengths can be calculated graphically. To find the resonance wavelength for a mode, refractive index of SiO_2 is plotted with calculated $n(\lambda)$ according to eq. 3.3 for corresponding mode. Intersection of the SiO_2 refractive index with calculated $n(\lambda)$ gives the solutions for the corresponding modes. Same approach is applied for finding the resonance wavelengths in the LWIR region where the absorber parameters are l=3.2 microns and t=1.3 microns.

Fig. 5.4 represents graphical solutions of resonance wavelengths for modes $\lambda(1,0)$, $\lambda(3,0)$ and $\lambda(1,1)$. Blue line represents the wavelength dependent refractive index $n(\lambda)$ of SiO_2 dielectric and straight lines indicated by legends of corresponding mode represents calculated function $n(\lambda)$ according to eq 3.3. It can be seen that because of the presence of strong dispersion of SiO_2 refractive index there are several solutions for a single resonance mode. Thus, modes $\lambda(1,0)$, $\lambda(3,0)$ and $\lambda(1,1)$ have 3, 3 and 1 solutions for the resonance wavelength, respectively. If we carefully choose the thickness and the size of the squares, these multiple bands can be merged together to obtain broadband absorption.
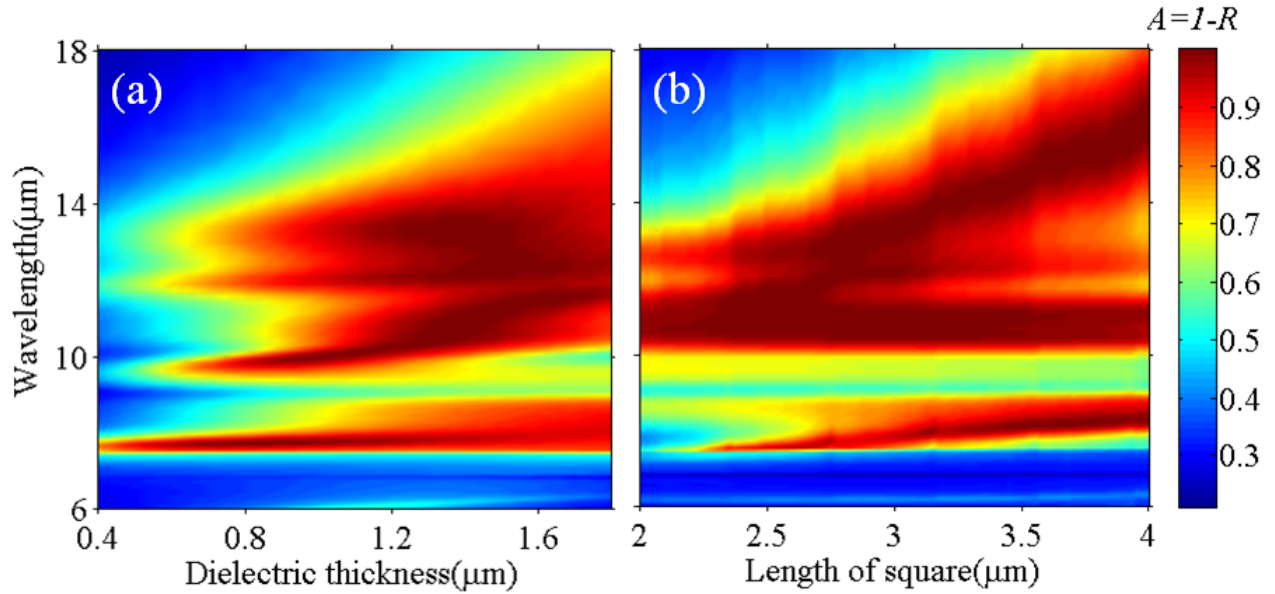
Figure 5.5: Colormap of absorptance as a function of wavelength and (a) dielectric thickness for l=3.5 microns and (b) length of the squares for t=1.4 microns.

5.3   FDTD Simulation Results

Fig. 5.4 represents graphical solutions for the resonance wavelengths of $\lambda(1,0)$, $\lambda(3,0)$ and $\lambda(1,1)$ modes. However, MDM cavity theory does not give information about the line-shape and strengths of absorption bands. FDTD simulations can provide information of strengths and band-widths for the absorption. To find optimum parameters for the highest and wide-band absorption FDTD simulations are performed for the structure using commercially available lumerical FDTD solutions (v9.1). Permittivity for gold is used from Drude model presented in chapter 3. Permittivity for SiO$_2$ is used from experimentally measured data (fig. 5.3). The details of the simulation method is

explain in chapter 3, sec.3.4.1. Fig. 5.5.a represents numerically simulated absorptance spectra as a function of wavelength and dielectric thickness while size of the squares, l= 3.5 microns remains constant. As predicted by theory, several absorption bands appear in the simulated spectra. With increase in dielectric thickness the resonances shift towards longer wavelength. The strength and width of the absorption band increase with increase in t. When the dielectric thickness is from 1.2-1.6 microns maximum absorption of more than 90% is obtained for several bands in the range 8-15 microns.

Fig. 5.5.b represents colormap of absorptance as a function of size of squares (l). The thickness of the dielectric is 1.4 microns which is determined from fig 5.5.a for the condition of strongest absorption. With increase in l, the resonances red-shift. For l=3-3.5 microns, the overall absorption covers a wide region from 8-14 microns. However there is a region of width of 1 microns from 9-10 microns where there is no absorption bands. This gap appears because of absence of strong resonance modes which is also predicted by theory (fig. 5.4).
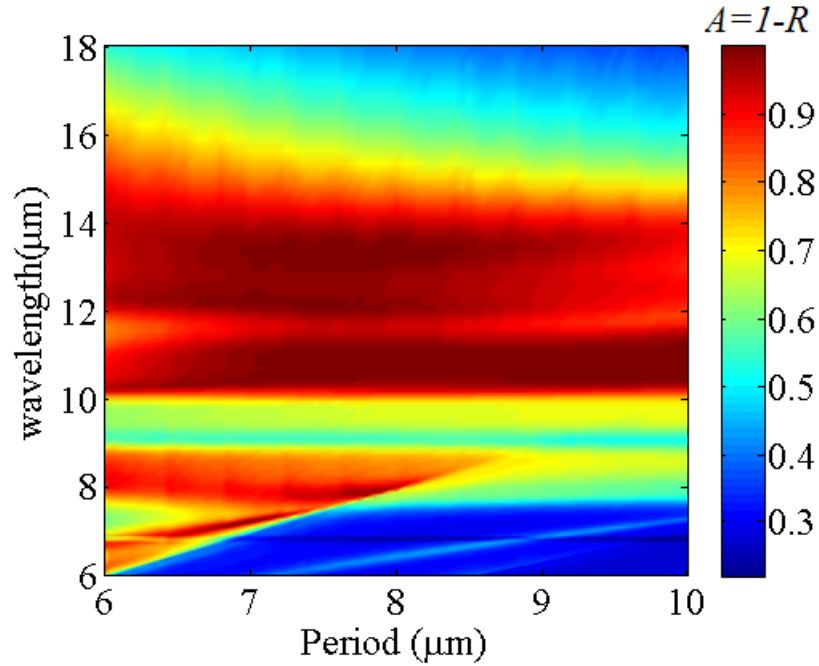
Figure 5.6: Colormap of absorptance as a function of periodicity of the squares arrays. The parameters for the sample are l=3.5 microns and t=1.4 microns.

Fig. 5.6 represents colormap of absorptance as a function of periodicity of the square arrays while the other parameters for the sample are l=3.5 microns and t=1.4 microns. Fig. 5.6 shows that for range of periods from 7-8 microns maximum absorptions are obtained. Again, as predicted by our theory there is little dependence of periodicity on the resonance wavelengths for such absorbers. From simulation results, the optimum parameters for the absorbers are determined as l=3.5 microns, t=1.4 microns and periodicity, p= 7.5 microns.

5.4   Experimental Details

We fabricated absorbers using standard photolithography and deposition of metal and SiO_2 by e-beam evaporation. A 150 nm thick layer of gold was deposited by electron beam evaporation on a glass or Si substrate. Then, SiO_2 was deposited as dielectric spacer by electron beam evaporation. For the sample with evaporated SiO_2, a 10 nm layer of Cr was also deposited before deposition of SiO_2 as a sticking layer. Thicknesses of the e-beam evaporated films are controlled by a thickness monitor followed by cross-checking of step profilometry. Surface squares are patterned by photolithography. Metalization for the square arrays are done using DC sputtered gold. The gold thickness is 200nm which is determined from sputtering time. Dimension of the squares and their period were determined by confocal microscopy. Samples were similarly prepared without the surface squares for comparison.
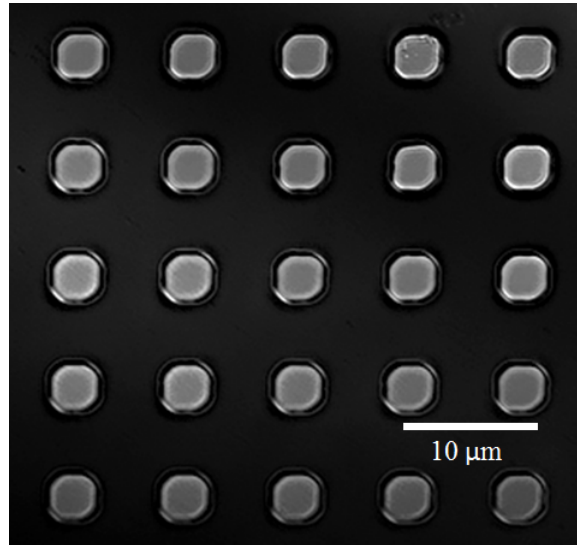
Figure 5.7: Confocal microscope image of the sample surface. Measured sample parameters are given by l=3.2 microns, t=1.3 microns and periodicity,a=7.5 microns.

Reflectance measurement was performed using BOMEM DA8 FTIR spectrometer. The setups for the normal incidence and angle dependent reflectance are the same ones used in far-IR measurements in chapter 3. For measure the reflectance in the LWIR region a liquid nitrogen cooled MCT detector. A globar source with KBr beamsplitter is used to illuminate the sample. Optically thick smooth gold film was used as the reference spectrum. Absorptance, A of the is calculated using the relation $A = 1 - R$, assuming scattering to be negligible because the particle size is much smaller than the wavelength of incident light. There is no transmission through the sample because the gold ground plane is optically thick.

5.5   Results and Discussion

Fig. 5.8 represents experimental reflectance spectra with and without gold squares on the top surface. Blue solid and dashed lines represent reflectance of samples with square surface patterns and without patterns, respectivley. The sample without squares (dashed line) shows prominent absorption bands at 3, 6.2, 8.5, 10 and 12.34 microns and some unresolved bands $\sim$10 microns. These absorptions are because of phonon vibrations in SiO_2. Strongest absorption from SiO_2 appear at 10 microns with 98%.

In fig. 5.8 solid blue line represent experimental reflectance spectrum for a sample with parameters t=1.3 microns and l=3.2 microns with surface square patterns as shown in fig. 5.7. Several strong absorption bands appear other than the SiO_2 bands. Dashed vertical lines represents the resonance wavelengths calculated according to eq. 3.3 as shown in fig. 5.4.
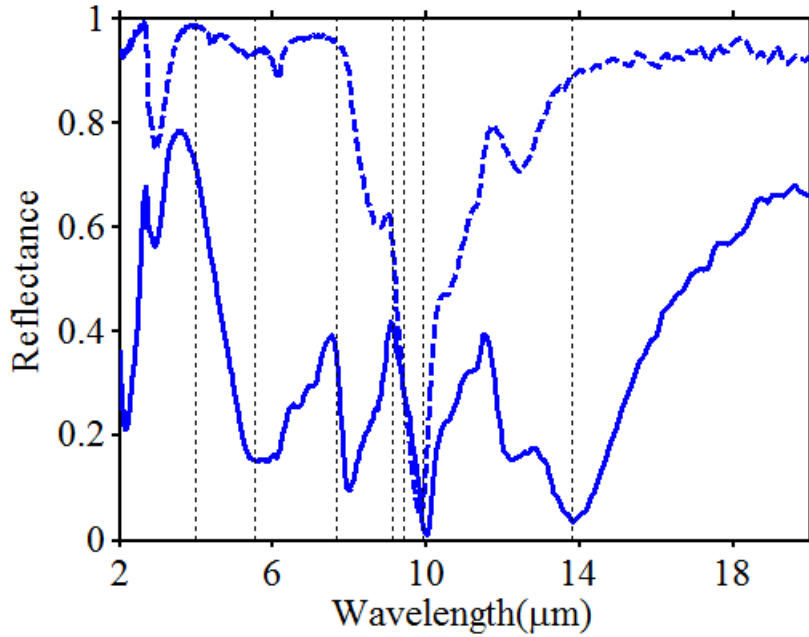
Figure 5.8: Dashed and solid lines are spectra from samples without squares and with squares, respectively. Dashed vertical lines represent theoretically calculated resonance wavelengths. The sample parameters, as determined from SEM images, are t=1.3 microns, l=3.2 microns and a=7.5 microns.

Table 5.1 represents calculated and experimentally measured resonance wavelengths for modes $\lambda(1,0)$, $\lambda(3,0)$, and $\lambda(1,1)$. Theory shows excellent match with experiments. The fundamental resonance wavelength for $\lambda(1,0)$ is obtained at 13.8 microns which is also predicted by theory at same wavelength. The absorption strength for this mode is 97%. Secondary resonance for $\lambda(1,0)$ at 9.1 microns is not distinctly seen in the experiment. This is because of overlapping of the resonance band with the native absorption band of SiO_2 at ~10 microns. The third resonance for $\lambda(1,0)$ at 7.6 microns is present in the experimental spectrum which appears slightly towards the longer wavelength by 0.5%.

For mode $\lambda(3,0)$, theoretical resonances are obtained at 9.95, 9.4, and 5.5 microns. Resonances at 9.95 and 9.4 microns overlap with SiO_2 native absorption at 9.5 microns and are not resolvable in the experimental spectrum. Experimental spectrum shows resonance at 5.5 microns with 85% absorption which is also predicted by theory at same wavelength.

For mode $\lambda(1,1)$ theoretical resonance occurs at 4 microns wavelength. Experimental spectrum however does not show any absorption band at 4 microns. There is a weak band with 60% absorption strength at 2.8 microns.

Table 5.1: Resonance wavelengths

Sample parameters		$\lambda(1,0)$	$\lambda(3,0)$	$\lambda(1,1)$
Theory	l=3.2, t=1.3	13.8, 9.1, 7.6	9.9, 9.4, 5.5	4.0
Experiments	l=3.1, t=1.3	13.8,—, 7.6	9.9,—, 5.5	3.0

(Unit= microns)

There is a strong absorption band in the experimental spectrum of samples with squares at 12.34 microns with 85% absorption strength which is not predicted by theory. This band is a native SiO_2 band which is seen in SiO_2 reflectance spectrum however with much weaker strength. According to MDM cavity theory, the MDM cavity only allows light at specific wavelengths to form standing waves. The native absorption bands due to SiO_2 increases with thickness of the dielectric according to by Beer Lambarts law. When the squares are present, light takes a longer path though the cavity $2\sqrt{t^2 + l^2/4}$ as compared to $2t$ for sample without squares. This produces enhanced absorption from SiO_2. This effect will show only when the resonance is close to the SiO_2 absorption band. 12.34 microns is close to the fundamental resonance mode at 13.8 mcrons, so some light is allowed at this wavelength to form standing waves and trapped. Since SiO_2 is highly absorbing in this range, because of increased path length in the cavity as compared to

without cavity (without squares), the absorption is enhanced. This effect is also seen for the band at 8.7 microns. SiO_2 shows an absorption band at 8.7 microns wavelength (fig. 5.8(dashed line)). Because of the cavity, this band is also enhanced and shows up as a shoulder with 75% absorption with the resonance at 7.6 microns in the experimental spectrum for the sample with squares. The absorption band at 5.5 microns also shows same effect. The weak bands present in the SiO_2 show up with enhanced absorption which make the absorption band at 5.5 microns look more flat and rippled (fig 5.8, solid line).
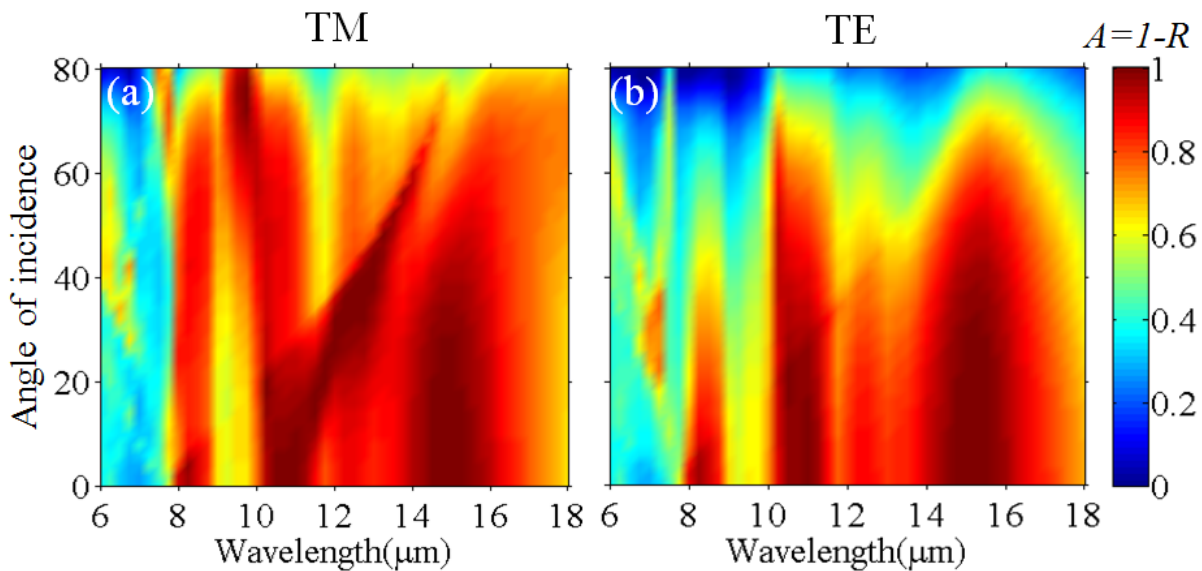
Figure 5.9: Colormap of numerically simulated absorptance as a function of incident angle for a sample parameters of t=1.4 microns, l=3.5 microns and a=7.5 microns for (a) TM polarization, (b) TE polarization.

Fig. 5.9 represent experimental reflectance spectra as a function of incident angle for a sample with t=1.4 microns, l=3.5 microns and a=7.5 microns. For TM polarized light (fig.

92

5.9.a), the absorber maintains strong absorption up to 80 degrees. For most of the absorption bands there is little shift in the resonance wavelength with increase in angle of incidence from 0-80 degrees but one at ~7.5 microns for which the resonance wavelengths increases linearly with angle. This band can be identified as a diffraction mode similar to the Wood's anomaly obtained for the far IR absorber. For the first order diffraction mode Wood's anomaly of Rayleigh type gives $\lambda = a(1 - sin\theta)$. For 0 degree incidence the diffraction order is seen at 7.5 microns which is almost the same as seen in the simulations.

For TE polarization strong absorption is sustained up to 70 degrees of angle of incidence (fig. 5.9). The resonance wavelength does not change with increase in angle of incidence. Wood's anomaly of first order is seen at ~7.5 microns for TE polarization too, however, with much weaker strength.
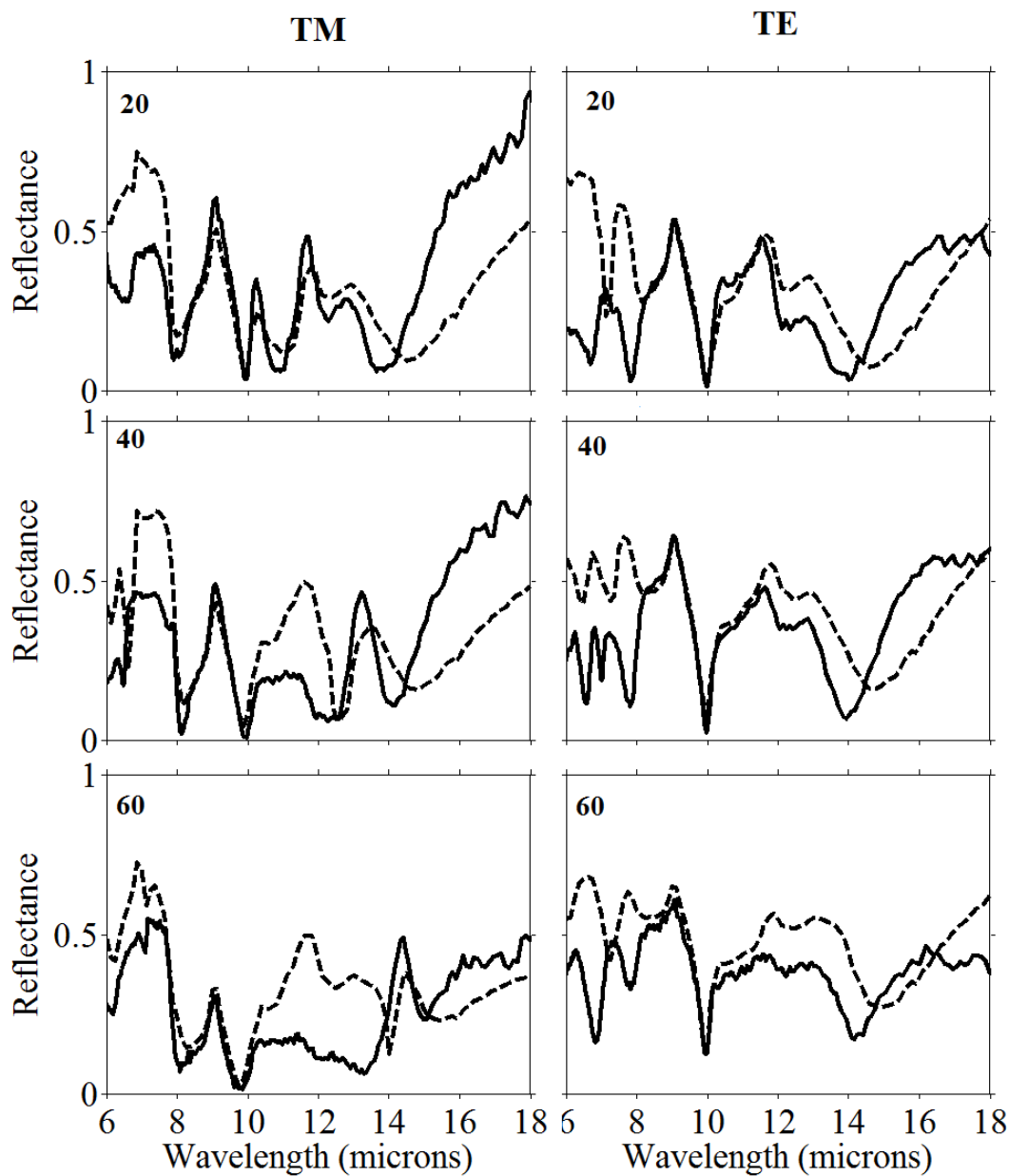
Figure 5.10: Experimental reflectance spectra (solid lines) as a function of incident angle for a sample with t=1.3 microns and l=3.2 microns. (a) TM polarization, (b) TE polarization. Dashed lines represent numerically calculated spectrum.

Fig. 5.10a and b represents experimental reflectance spectra for a sample with t=1.3 microns, l=3.2 microns and a=7.5 microns for TM and TE polarization, respectively. The angle of incidence are 20, 40 and 60 degrees as indicated in the legends in the respective plots. Dashed lines represent numerically calculated spectra for the same sample parameters. At 60 degree angle of incidence, the resonance strength reduces for both the polarization by $\sim$20%. Also, the fundamental resonance wavelength red-shift by $\sim$7%. For the angle dependent reflectance measurements, a bigger sample of area 1 inch x 1 inch is used. Such big samples show non-uniform size of squares. The non-uniformity is because of limitation of our mask aligner non-uniform intensity UV radiation which creates a gradient in the size of the squares. In the angle dependent measurement, the beam illuminates different areas of the samples with change in the angle. This might be a possible explanation for the red-shift and mismatch of simulated and measured reflectance.

5.6   Summary

We have experimentally demonstrated strong design-tunable absorption bands in the LWIR wavelength regions for a surface composed of gold squares separated from a gold plane by a SiO2 dielectric layer. The positions of the resonances are predicted with reasonable accuracy using a simple analytic model. Optimum thickness of the dielectric is required for the perfect absorption to occur. This absorption is sustained to wide angle of incidence up to 80 degrees. More than 80% of absorption is achieved in the range of 8-14 microns which includes the LWIR atmospheric transmission window. This can be useful for thermal detectors working in this range.

CHAPTER 6: SYNCHROTRON INFRA-RED SPECTRAL MICROSCOPY OF METAL-DIELECTRIC-METAL CAVITY METAMATERIAL ABSORBERS

In this chapter, we present experimental results of synchrotron IR micro-spectroscopy on thin MDM absorbers in the mid-IR region. We fabricate absorber with a single isolated surface square and compared reflectance with periodic array of surface squares of same size. IR micro-spectroscopy was used to collect hyper-spectral data with diffracted limited spatial resolution using the Infrared Environmental Imaging (IRENI) beam line at the Synchrotron Radiation Center (SRC), University of Wisconsin, Madison [102, 103] . This is the first time measurement of absorption from a single unit cell of such an absorber. It shows that there is no need of any periodic structure for such absorption. We show that there is negligible interaction among the unit cells which affects the resonances.

6.1   Introduction

A sychrotron is a cyclic particle accelerator where magnetic fields are synchronized with with the increasing kinetic energy of the particles to account for relativistic increase in mass when the speed reaches close to that of light. This way charged particles can reach ultra-high-relativistic speed [104]. A synchrotron is a strong source of electro-magnetic radiation. These radiations are generated by highly energetic electrons which move in large circular tunnels or storage rings in a synchrotron. The main principle behind such radiation is that a moving charge emits radiation when it changes direction or accelerates. Depending up on the energy of the moving electron it can emit broad-band radiation in X-ray, visible and infra-red regions or in principle in the entire range

of electro-magnetic spectrum. In a synchrotron, electrons are accelerated to ultra-high energy and then make them change direction periodically to produce extreme high intensity, highly collimated photon beams.

Fourier transform infrared microspectroscopy and imaging have emerged as extremely useful techniques for microscopic scale, non-destructive analysis of chemical-composition of materials with wide range of applications such as analysis of graphene-based materials [105, 106], rocks, bio-minerals [107], and asteroid-rock analysis [108, 109], and pharmaceuticals [110]. Due to low intensity thermal sources, conventional FTIR microscopy has limitations in spatial resolution, signal to noise ration, image area, and acquisition time [102]. Globar is currently the most popular source of broad-band thermal source for IR spectroscopy while using point-detectors. Globar is a SiC bar which is heated to temperature of $\sim$1000-1650^{0}C which give out radiation with spectra behavior closely matched with Plancks radiation. However, the intensity obtained is low for modern Focal Plane Array (FPA) based imaging purpose. Multi-beam Synchrotron radiation is useful for such imaging which can produce highly collimated IR radiation with $\sim$1000 times higher brightness than globar [102] which enable truly diffraction limited imaging with high spectral quality and spatial resolution [102].

The main objective of this work is to test MDM cavity theory of metamaterial absorbers. In chapter 3, we showed that periodicity of the squares in metamaterial absorber does not effect the resonance mechanism. Numerical simulation in the far-IR region (fig. 3.6) showed little change of resonance wavelength with increase in periodicity of the structures while other sample parameters t and l remained constant. When the squares are far apart, the overall intensity from the sample is reduced which is because of reduced fill factor. Conventional FTIR microscopy with poit-detector can not measure absorption from isolated squares because of small size and low absorption strength of the absorber. We use synchrotron based IR micro-spectroscopy to measure absorption of a single unit cell of a metamaterial absorber.

6.2   Theory

Microscopy of sub-wavelength structure is limited by diffraction limit given by [111],

$$d = \frac{\lambda}{2nsin\theta} \tag{6.1}$$

where d is the maximum size of the radius of a spot to be resolved, and n is the refractive index of the medium through which light converges to the spot at angle of θ. And, $nsin\theta$ is called the numerical aperture (NA). Considering a NA of 1. The diffraction limit is $d = \lambda/2$. In our case of far- and LW- IR MDM absorber, the operating wavelength is 5 times higher than the structure size (square length, l). Hence, resolving an individual surface squares at the operating wavelength is beyond the diffraction limit even for highest possible NA of ~1.5 with oil immersion technology [112]. Imaging of an isolated square and comparison with periodic array can give information of effect of periodicity on the absorption mechanism.

Multibeam synchrotron Infrared Environmental Imaging (IRENI) beam line at SRC has capability of performing diffraction limited imaging using FPA detectors in the entire mid-IR range. We design and fabricate MDM absorber samples in the mid-IR range with isolated squares of size ~2 microns which shows the fundamental absorption at ~6.5 microns. 100nm thick SiO_2 was used as the dielectric spacer layer, and 200nm thick gold was used as the conductor layer both for the square and the ground plane.

Figure 6.1: SEM image of (a)3 isolated squares of varying size from 1.5, 2.1, and 2.2 microns separated by ~10 microns (b) periodic array of squares of size 2.2 microns and periodicity of 3.2 microns.

6.3   Experimental Details

At SRC multiple beams (up to 12) are combined to achieve high brightness of up to ~1000 times more than globar source [103]. A Brucker Vertex FTIR spectrometer equipped with a 128 128 pixel FPA is used to collect data over 900-3700 cm^{-1} (2.7-11.1 mcirons wavelength) with 4 cm^{-1} spectral resolution. A Hyperion 3000 infra-red microscope was used, equipped with a Schwarzschild objective with 20x, 0.65 numerical aperture (NA). With this set-up data can be collected from an area of up to 60 micron x 40 microns illuminated by the collimated beams in one scan. IRidys (Infrared Imaging and Data Analysis) software was used to extract data from different pixels. The individual pixel size in the FPA is 0.54 microns x 0.54 microns [102, 103]. According to eq. 6.1, for NA=0.65, at 2.7 microns wavelength, the diffraction limit d=2.1 microns. Hence, individual pixels of size 0.54 microns x 0.54 microns give truly diffraction limited imaging at the

lowest wavelength of 2.7 microns. Pixels are ~4 times smaller than the diffraction limit. Specular reflection was collected for the measurements. The angle of incidence is calculated from NA, using $n=1$ for air, giving $\theta=40.5$ degrees.
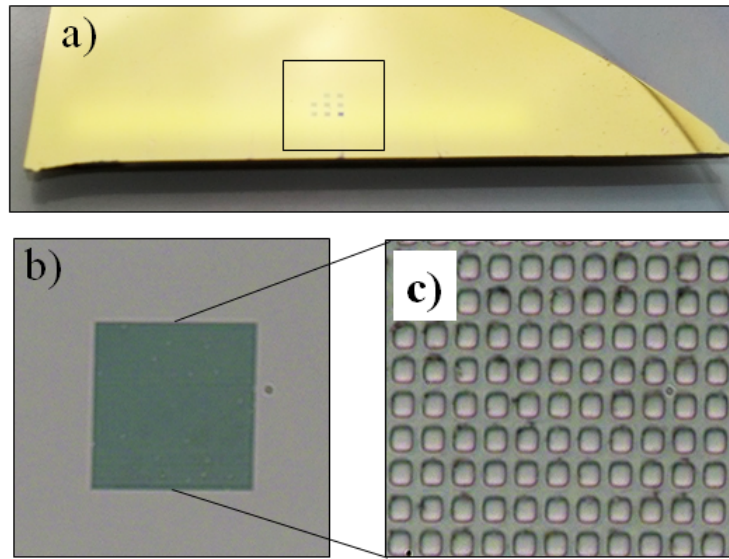
Figure 6.2: Optical images of (a)the sample surface taken by a digital camera, small dots in the in-set shows the periodic arrays. (b) optical microscope image of periodic array of squares of area 300 microns x 300 microns, c) magnified optical microscope image of the square arrays.

The absorber has a 3 layer MDM structure as shown in fig. (1.3). 10 nm of Cr is deposited on a Si wafer using electron beam lithography followed by deposition of 200nm of gold followed by another 10nm of Cr and 100nm of SiO_2 without breaking vacuum. Thickness monitor was used to control the thickness of the deposited films. Step profilometry was then used to cross-check the total thicknesses of the deposited films. Isolated squares of variable size from 1.5-2.2 microns are then patterned using electron beam lithography. The squares are isolated from each other by at least 10 microns distance. Periodic arrays of areas 300 microns x 300 microns of the

same squares are also patterned in the same sample 2 mm away from the isolated squares. 150 nm of DC sputtered gold is then deposited on the sample. Thickness of the DC sputtered gold is calculated from deposition time which was calibrated for the instrument. Then lift-off is performed u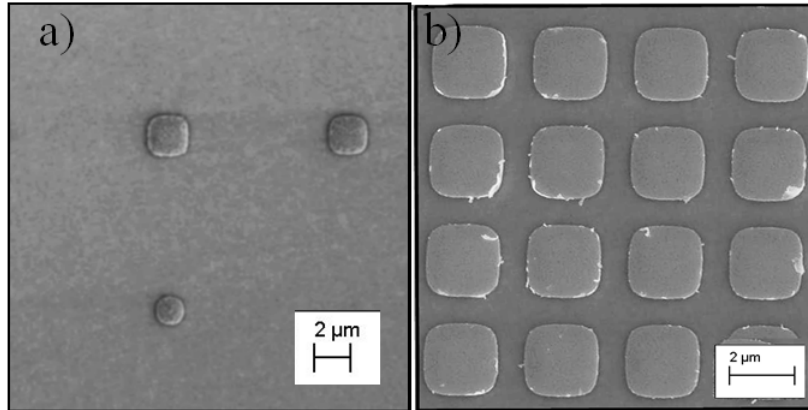sing acetone and sonication for 3 minutes. Fig. (6.1.a) shows SEM image of 3 isolated squares of varying size from 1.5, 2.1, and 2.2 microns separated by ~10 microns. Fig. (6.1.b) show periodic array of squares of size 2.2 microns and periodicity of 3.2 microns. Figs (6.2) a,b and c show optical images of the sample surface taken by a digital camera, (small dots in the in-set shows the periodic arrays), optical microscope image of periodic array of squares of area 300 microns x 300 microns, and magnified optical microscope image of the square arrays, respectively.

The absorptance of the samples can be found by using $A = 1 - R$, since transmission (T) through the sample is zero because of the optically thick ground gold film. Since the structure size is much smaller than the operating wavelength, scattering is assumed to be negligible.
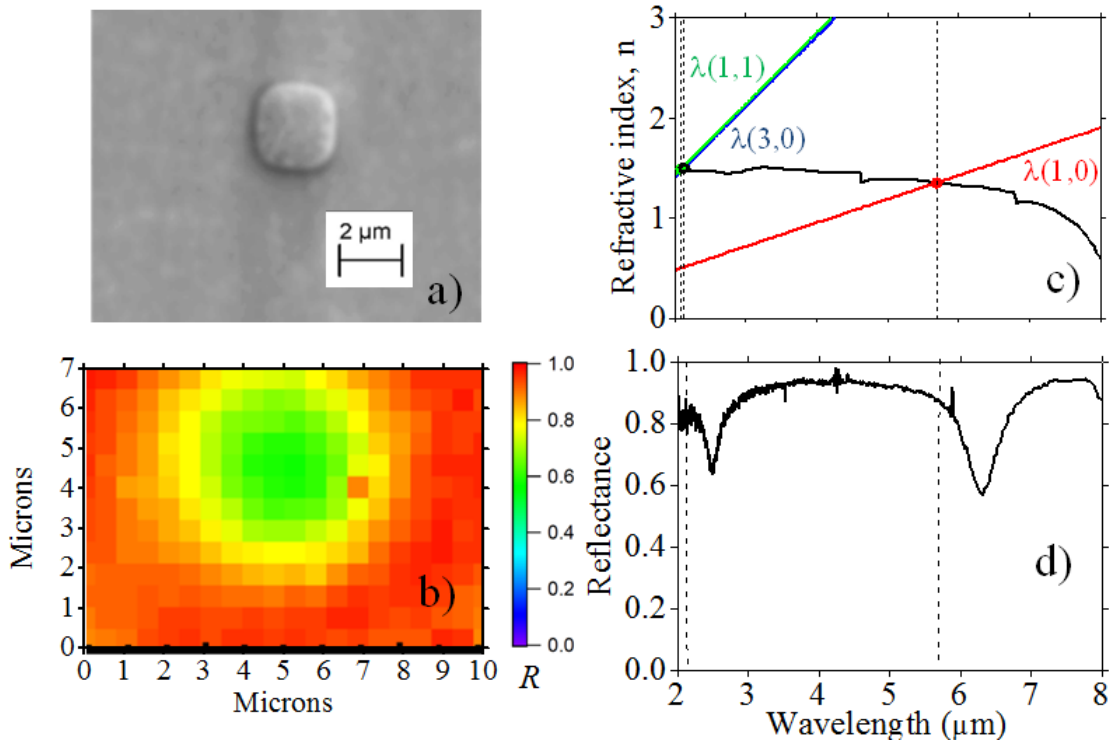
Figure 6.3: Synchrotron IR micro-spectroscopy data. a) an SEM image of the isolated square, b)IR image of the square at 6.3 microns wavelength, c) graphical calculation of resonance wavelengths for $\lambda(1,0)$,$\lambda(3,0)$ and $\lambda(1,1)$. Refractive index, n is measured by ellipsometry, sample parameters are l=2.1 microns and t=0.1 microns. For modes $\lambda(3,0)$ and $\lambda(1,1)$, resonance solutions overlap each other. d) reflectance spectrum of a pixel at the middle of the square in the IR image for highest absorption.

6.4   Results and Discussion

Fig. (6.3) shows synchrotron IR micro-spectroscopy data for a single isolated square absorber with parameters of l=2.1 microns and t=0.1 microns. Fig. (6.3.a) shows a SEM image of the

square. Fig. (6.3.b) represnts a IR image of the isolated square at 6.3 microns. In the IR image, the aquare is more than 2 times bigger than the actual square shown in fig. (6.3.a). The IR image is constructed of reflectance values as a function of x and y distance at 6.3 microns wavelength. According to eq. (6.1), the diffraction limit at 6.3 microns wavelength is d=4.8 microns. Since the square is smaller than the diffraction limit the IR image is not resolved, looks diffuse and as big as 4.8 microns.

fig. (6.3.c) represents graphical solution of resonance wavelengths for $\lambda(1,0)$,$\lambda(3,0)$ and $\lambda(1,1)$ according to eq. (3.3). Black line represnts refractive index, n of SiO_2 dielectric layer which is measured using a IR-VASE ellipsometer for 1.4 microns thick e-beam evaporated SiO_2 on 200nm smooth gold film. Sample parameters are l=2.1 microns and t=0.1 microns. Red, blue and green straight lines represent theoretically calculated $n(\lambda)$ using eq. (3.4-6) for $\lambda(1,0)$,$\lambda(3,0)$ and $\lambda(1,1)$ modes. Intersection of these staight lines with the experimental refractive index give solutions for the resonance wavelengths for the corresponding modes. Fundamental resonance $\lambda(1,0)$ is obtained at 5.7 microns. For modes $\lambda(3,0)$ and $\lambda(1,1)$, resonance solutions overlap each other, and is obtained at 2.1 microns.

Fig. 6.3.d represents reflectance spectrum for which data was extracted at a pixel in the middle of the IR image of the square which shows strongest absorption. Reflectance spectra shows two prominent dips at 6.3 microns and 2.5 microns which are identified as $\lambda(1,0)$ and $\lambda(3,0)$ resonance modes, respectively. Dashed vertical lines represent theoretically calculated resonances wavelengths for $\lambda(1,0)$ and $\lambda(3,0)$. Theory predicts experimental spectra at slightly smaller wavelength. Theory is off by 10% towards the shorter wavelength. No $\lambda(1,1)$ mode is observed in the reflectance spectrum as theory shows that resonance wavelength for mode $\lambda(1,1)$ overlaps with that of $\lambda(3,0)$.
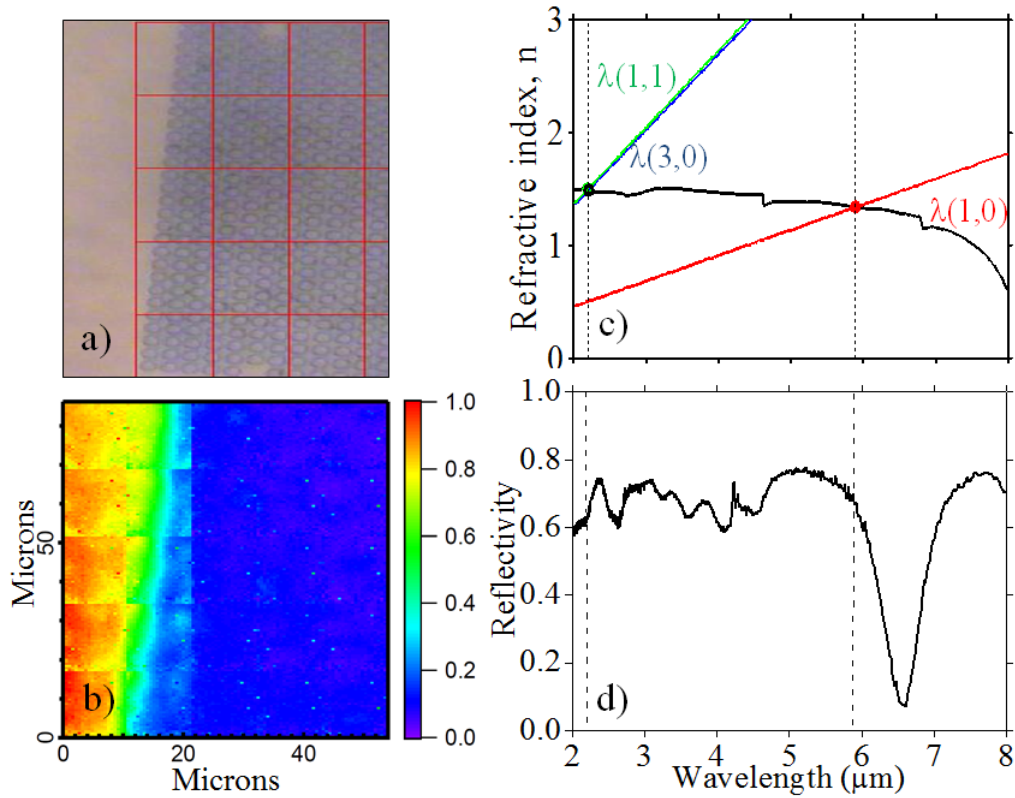
Figure 6.4: Synchrotron IR micro-spectroscopy imaging data. a) an optical image of the square arrays with square size l=2.2 microns and periodicity of 3.2 microns, b) IR image of the periodic structure at 6.6 microns wavelength, c) graphical solution of resonance wavelengths for $\lambda(1,0)$,$\lambda(3,0)$ and $\lambda(1,1)$ according to eq. (3.3), (d) reflectance spectrum at a pixel with highest absorption of 93% for the fundamental absorption band. Dashed horizontal lines represent theoretical resonances.

Fig. (6.4) represents IR micro-spectroscopy imaging data for periodic array of the squares. Fig. (6.4.a) represents an optical image of the sample used for alignment. IR imaging for the sample is done in several area scans as shown in the image with red boxes. Area of

104

each scan is around 20 microns x 10 microns. Fig. (6.4.b) represents IR image of the sample at 6.6 microns wavelengths. Figs (6.4.a) and b can be compared and identified to be same sample. Area without the squares looks red in the IR image, and area with squares looks blue showing strong absorption. When the collimated beam moves from one scan to the other, there is slihgt shift in reflectance base line. Because of this off-set in reflectance with change in scanning area a mosaic structure is seen in the image.

fig. (6.4.c) represents graphical solution of resonance wavelengths for $\lambda(1,0)$,$\lambda(3,0)$ and $\lambda(1,1)$ according to eq. (3.3)with sample parameters l=2.2 microns and t=0.1 microns. Fundamental resonance $\lambda(1,0)$ is obtained at 5.9 microns. For modes $\lambda(3,0)$ and $\lambda(1,1)$, resonance solutions overlap each other, and is obtained at 2.2 microns.

Fig. 6.4.d represents reflectance spectrum for which data was extracted at a pixel from the most absorbing part of the absorber in the IR image (blue part in the right). Reflectance spectrum shows one prominent dip at 6.7 microns and several low absorption bands at 4.5, 4.1, 3.6, 3.3 and 2.6 microns. Dashed vertical lines represent theoretically calculated resonances for $\lambda(1,0)$ and $\lambda(3,0)$. Absorption band at 6.7 with 93% absorption can be identified as $\lambda(1,0)$. Similarly, absorption band at 2.6 microns with 48% absorption is close to theoretical mode $\lambda(3,0)$.

Table 6.1: Comparison of resonance wavelengths

	Sample parameters	Theory	Experiments
Single square	l=2.1, t=0.1	$\lambda(1,0)$=5.7	$\lambda(1,0)$=6.3
		$\lambda(3,0)$=2.1	$\lambda(3,0)$=2.5
Periodic array	l=2.2, t=0.1	$\lambda(1,0)$=5.9	$\lambda(1,0)$=6.7
		$\lambda(3,0)$=2.2	$\lambda(3,0)$=2.6

(Unit= microns)

105

Table 6.1 compares resonance wavelengths for single and periodic arrays. SEM imaging reveals that the size of the single square is smaller than the periodic square by 5% which can be considered negligible. The experimental resonance wavelength for the fundamental mode is 6.3 microns and 6.7 microns for single isolated square and the periodic square, respectively. For the periodic squares, the experimental fundamental mode appear at 6% higher than the isolated square. For theoretical calculations, this difference is 4%. The theoretical difference comes from difference in size of the isolated square (l=2.1 mcirons) and the size of the periodic squares (l=2.2 mcirons). Adjusting for this 4% difference in the we can say that there in only 2% difference in experimental fundamental resonance wavelength difference between isolated square and periodic squares. This proves our assumption in standing wave based MDM cavity thoery of metamaterial absorbers that the squares are weakly interacting.

The slight redshift in fundamental resonance for periodic square arrays can be explained by interaction of oppositely oriented dipoles. In chapter 3, it was seen that the polarity of the top square edge for two adjacent squares are opposite. When they come too close, both dipoles at the adjacent squares tend to cancel each other. Because of this effect, the energy needed to drive these coupled dipoles is smaller. Hence, the resonance wavelength red-shifts.

Similarly for experimental $\lambda(3,0)$ mode, resonance is redshifted by 4% for the periodic arrays as compared to isolated square. For theoretical calculations resonance wavelength for $\lambda(3,0)$ is 5% redshifted for the periodic arrays as compared to isolated square.

Calculated resonance wavelengths for $\lambda(1,0)$ and $\lambda(3,0)$ modes are off by $\sim$10% towards the shorter wavelength. MDM cavity theory is not in good agreement in calculating the resonance wavelength. However, it did predict number of resonance orders correctly for the isolated squares. The red-sift in the experimental spectrum can be because of plasmon resonances as seen in [82, 83, 85, 96]. With decrease in thickness, the plasmon modes on the top square and ground plane

tend to cancel each other resulting in red-shift in absorption. Also, one significant difference of this absorber from the far-IR absorber in chapter 3 is that, the thickess of the dielectric is 67 times thinner than the wavelength as compared to 18 times for the far-IR absorbers. This case is similar to ref [33]. Hao *et al.*, shows that for ultra-thin absorbers in the visible with decease in thickness of the dielectric spacer the resonance red-shifts [33]. Which might be the case for these mid-IR absorbers.

MDM cavity theory can not explain the multiple resonance orders seen between modes $\lambda(1,0)$ and $\lambda(1,0)$ in the experimental spectrum. These bands might be arising because of the weak interaction between adjacent squares which is neglected in our calculations.

One prominent difference in experimental spectrum of isolated square and periodic squares is that, the absorption for periodic squares is more than 2 times higher for the fundamental than the isolated square. This can be explained by the diffraction limit. At 6.3 microns wavelength the calculated diffraction limit is 4.8 microns. Anything smaller than 4.8 microns is not resolvable and appears diffuse. Hence, the 2.1 micros size square is seen as the a bigger square of more than twice its actual size. The reflectance is distributed over a larger area which reduces the reflectance at individual pixels although data is collected from a pixel at the center.

6.5   Summary

Standing wave based MDM cavity theory of metamaterial absorber works excellent in the far- and LW- IR regions for absorbers with dielectric thickness ∼15 times thinner than the resonance wavelength whcih was presented in chapter 3. For the first time we perform IR micro-spectroscopy on absorber with isolated squares and tested MDM cavity theory in the mid-IR region. Theory predicts number of resonances correctly for an isolated square. Reflectance spectrum of single

isolated square and periodic arrays produce similar absorption bands and resonance wavelengths. Periodicity has negligible effect on the resonance wavelengths of the absorber. Predicted resonance wavelength is blue-shifted by 10% from the experimental resonances. The absorber is $\sim$67 tjmes thinner than the wavelength. For such thin absorbers coupling of surface plasmon modes from the top square and the bottom ground might be a possible explanation for the observed blue-shift for theoretical resonance wavelengths.

CHAPTER 7: CONCLUSION

We have experimentally demonstrated thin-film triple layer metal-dielectric-metal (MDM) structures for absorption of electromagnetic radiation in the UV, visible, near-, mid-, LW- and far-IR regions with absorbption of up to 97%. All the absorbers were fabricated with CMOS compatible processing. We have also developed a novel theoretical model of such absorbers based on standing wave resonances in MDM cavity. Theory successfully explains experimental results for the absorbs we fabricated.

We have experimentally demonstrated a thin far IR absorber with up to ~95% absorption for the fundamental band at 53.5 m wavelength (5.6 THz). The thickness of the absorber is only 3 microns which is 18 times smaller than the resonance wavelength. Absorption bands depend weakly on polarization and angle of incident. FDTD simulation results and theory show excellent agreement with experimental results.

We have also experimentally demonstrated an triple layer MDM absorber in the visible and near IR range with large band-widths up to ~1 microns which does not need any lithographic patterning. Observed fundamental-resonance absorption strengths are in the range 93 to 97%. A theoretical model based on effective medium approximation was developed to explain such absorbers with thin discontinuous metal films on the top surface.

We also succeed in achieving strong wide-band absorption up to 97% in the range from 8-14 microns using simple 3 layer MDM structures with periodic squares as surface pattern. Multiple overlapping aborption bands cover the entire range of LWIR band important for thermal imaging. The absorber is 10 times thinner than the operating wavelength and absorption bands are weakly dependent on polarization and angle of incidence.

To farther test the MDM cavity theory experimentally, we measured the spatial distribution of absorption for a single unit cell of a MPA, using diffraction-limited synchrotron-based infrared spectral microscopy in the 2-8 micron wavelength range. Our theoretical model was successful in prediction of periodicity independent nature of the resonances.

In summary, we demonstrated fabrication of thin CMOS compatible perfect absorbers useful for commercial detectors in the IR regions. We also developed a theoretical model of MPA based on standing wave resonances in MDM cavity. MDM cavity model can calculate resonance wavelengths for experiments with excellent agreement in the mid- to far-IR regions. However, resonance wavelengths for MPAs in the visible obtained by MDM cavity model occur at much higher frequency than reported simulation results. Future work in this field will be modification of MDM cavity to explain absorption of MPAs in the visible, and application of fabricated MPA coating to IR bolometers for enhancement of performance.

LIST OF REFERENCES

[1] A. Vora, J. Gwamuri, N. Pala, A. Kulkarni, J. M. Pearce, and D. Ö. Güney, "Exchanging ohmic losses in metamaterial absorbers with useful optical absorption for photovoltaics," *Scientific reports*, vol. 4, 2014.

[2] Y. Wang, T. Sun, T. Paudel, Y. Zhang, Z. Ren, and K. Kempa, "Metamaterial-plasmonic absorber structure for high efficiency amorphous silicon solar cells," *Nano letters*, vol. 12, no. 1, pp. 440–445, 2011.

[3] C. Wu, B. Neuner III, J. John, A. Milder, B. Zollars, S. Savoy, and G. Shvets, "Metamaterial-based integrated plasmonic absorber/emitter for solar thermo-photovoltaic systems," *Journal of Optics*, vol. 14, no. 2, p. 024005, 2012.

[4] C. Simovski, S. Maslovski, I. Nefedov, and S. Tretyakov, "Optimization of radiative heat transfer in hyperbolic metamaterials for thermophotovoltaic applications," *Optics express*, vol. 21, no. 12, pp. 14988–15013, 2013.

[5] H. Tao, N. I. Landy, C. M. Bingham, X. Zhang, R. D. Averitt, and W. J. Padilla, "A metamaterial absorber for the terahertz regime: Design, fabrication and characterization," *Optics express*, vol. 16, no. 10, pp. 7181–7188, 2008.

[6] T. Maier and H. Brückl, "Wavelength-tunable microbolometers with metamaterial absorbers," *Optics letters*, vol. 34, no. 19, pp. 3012–3014, 2009.

[7] Q. Gao, Y. Yin, D.-B. Yan, and N.-C. Yuan, "Application of metamaterials to ultra-thin radar-absorbing material design," *Electronics Letters*, vol. 41, no. 17, pp. 936–937, 2005.

[8] A. K. Zadeh and A. Karlsson, "Capacitive circuit method for fast and efficient design of wideband radar absorbers," *Antennas and Propagation, IEEE Transactions on*, vol. 57, no. 8, pp. 2307–2314, 2009.

[9] N. Liu, M. Mesch, T. Weiss, M. Hentschel, and H. Giessen, "Infrared perfect absorber and its application as plasmonic sensor," *Nano letters*, vol. 10, no. 7, pp. 2342–2348, 2010.

[10] F. Alves, D. Grbovic, B. Kearney, and G. Karunasiri, "Microelectromechanical systems bimaterial terahertz sensor with integrated metamaterial absorber," *Optics letters*, vol. 37, no. 11, pp. 1886–1888, 2012.

[11] M. Diem, T. Koschny, and C. M. Soukoulis, "Wide-angle perfect absorber/thermal emitter in the terahertz regime," *Physical Review B*, vol. 79, no. 3, p. 033101, 2009.

[12] X. Liu, T. Tyler, T. Starr, A. F. Starr, N. M. Jokerst, and W. J. Padilla, "Taming the blackbody with infrared metamaterials as selective thermal emitters," *Physical review letters*, vol. 107, no. 4, p. 045901, 2011.

[13] D. Panjwani, M. Yesiltas, J. Nath, D. Maukonen, I. Rezadad, E. M. Smith, R. Peale, C. Hirschmugl, J. Sedlmair, R. Wehlitz, *et al.*, "Patterning of oxide-hardened gold black by photolithography and metal lift-off," *Infrared Physics & Technology*, vol. 62, pp. 94–99, 2014.

[14] R. W. Wood, "On a remarkable case of uneven distribution of light in a diffraction grating spectrum," *Proceedings of the Physical Society of London*, 1902.

[15] H. Raether, *Surface plasmons on smooth surfaces*. Springer, 1988.

[16] S. A. Maier, *Plasmonics: fundamentals and applications*. Springer Science & Business Media, 2007.

[17] M. Hutley and D. Maystre, "The total absorption of light by a diffraction grating," *Optics communications*, vol. 19, no. 3, pp. 431–436, 1976.

[18] N. Bonod, G. Tayeb, D. Maystre, S. Enoch, and E. Popov, "Total absorption of light by lamellar metallic gratings," *Optics express*, vol. 16, no. 20, pp. 15431–15438, 2008.

[19] A. Christ, T. Zentgraf, S. Tikhodeev, N. Gippius, O. Martin, J. Kuhl, and H. Giessen, "Interaction between localized and delocalized surface plasmon polariton modes in a metallic photonic crystal," *physica status solidi (b)*, vol. 243, no. 10, pp. 2344–2348, 2006.

[20] A. Christ, G. Lévêque, O. Martin, T. Zentgraf, J. Kuhl, C. Bauer, H. Giessen, and S. Tikhodeev, "Near-field–induced tunability of surface plasmon polaritons in composite metallic nanostructures," *Journal of microscopy*, vol. 229, no. 2, pp. 344–353, 2008.

[21] A. P. Hibbins, W. A. Murray, J. Tyler, S. Wedge, W. L. Barnes, and J. R. Sambles, "Resonant absorption of electromagnetic fields by surface plasmons buried in a multilayered plasmonic nanostructure," *Physical Review B*, vol. 74, no. 7, p. 073408, 2006.

[22] W. W. Salisbury, "Absorbent body for electromagnetic waves," June 10 1952. US Patent 2,599,944.

[23] B. A. Munk, *Frequency selective surfaces: theory and design*. John Wiley & Sons, 2005.

[24] E. Lifshitz, L. Pitaevskii, and L. Landau, *Electrodynamics of Continuous Media: Volume 8*. Butterworth-Heinemann, 1984.

[25] S. Shu, Z. Li, and Y. Y. Li, "Triple-layer fabry-perot absorber with near-perfect absorption in visible and near-infrared regime," *Optics express*, vol. 21, no. 21, pp. 25307–25315, 2013.

[26] V. G. Veselago, "The electrodynamics of substances with simultaneously negative values of ε and μ," *Physics-Uspekhi*, vol. 10, no. 4, pp. 509–514, 1968.

[27] J. B. Pendry, A. J. Holden, D. Robbins, and W. Stewart, "Magnetism from conductors and enhanced nonlinear phenomena," *Microwave Theory and Techniques, IEEE Transactions on*, vol. 47, no. 11, pp. 2075–2084, 1999.

[28] D. R. Smith, W. J. Padilla, D. Vier, S. C. Nemat-Nasser, and S. Schultz, "Composite medium with simultaneously negative permeability and permittivity," *Physical review letters*, vol. 84, no. 18, p. 4184, 2000.

[29] R. Shelby, D. Smith, S. Nemat-Nasser, and S. Schultz, "Microwave transmission through a two-dimensional, isotropic, left-handed metamaterial," *Applied Physics Letters*, vol. 78, no. 4, pp. 489–491, 2001.

[30] J. B. Pendry, "Negative refraction," *Contemporary Physics*, vol. 45, no. 3, pp. 191–202, 2004.

[31] J. B. Pendry, "Negative refraction makes a perfect lens," *Physical review letters*, vol. 85, no. 18, p. 3966, 2000.

[32] J. Pendry, A. Holden, W. Stewart, and I. Youngs, "Extremely low frequency plasmons in metallic mesostructures," *Physical review letters*, vol. 76, no. 25, p. 4773, 1996.

[33] J. Hao, L. Zhou, and M. Qiu, "Nearly total absorption of light and heat generation by plasmonic metamaterials," *Physical Review B*, vol. 83, no. 16, p. 165107, 2011.

[34] B.-I. Wu, W. Wang, J. Pacheco, X. Chen, T. M. Grzegorczyk, and J. A. Kong, "A study of using metamaterials as antenna substrate to enhance gain," *Progress In Electromagnetics Research*, vol. 51, pp. 295–328, 2005.

[35] N. Landy, S. Sajuyigbe, J. Mock, D. Smith, and W. Padilla, "Perfect metamaterial absorber," *Physical review letters*, vol. 100, no. 20, p. 207402, 2008.

[36] D. Schurig, J. Mock, B. Justice, S. A. Cummer, J. Pendry, A. Starr, and D. Smith, "Metamaterial electromagnetic cloak at microwave frequencies," *Science*, vol. 314, no. 5801, pp. 977–980, 2006.

[37] A. Alù and N. Engheta, "Achieving transparency with plasmonic and metamaterial coatings," *Physical Review E*, vol. 72, no. 1, p. 016623, 2005.

[38] M. Navarro-Cía, M. Beruete, S. Agrafiotis, F. Falcone, M. Sorolla, and S. A. Maier, "Broadband spoof plasmons and subwavelength electromagnetic energy confinement on ultrathin metafilms," *Optics express*, vol. 17, no. 20, pp. 18184–18195, 2009.

[39] M. J. Lockyear, A. P. Hibbins, and J. R. Sambles, "Microwave surface-plasmon-like modes on thin metamaterials," *Physical review letters*, vol. 102, no. 7, p. 073901, 2009.

[40] J. Nath, D. Maukonen, E. Smith, P. Figueiredo, G. Zummo, D. Panjwani, R. E. Peale, G. Boreman, J. W. Cleary, and K. Eyink, "Thin-film, wide-angle, design-tunable, selective absorber from near uv to far infrared," in *SPIE Defense, Security, and Sensing*, pp. 87041D–87041D, International Society for Optics and Photonics, 2013.

[41] J. Hendrickson, J. Guo, B. Zhang, W. Buchwald, and R. Soref, "Wideband perfect light absorber at midwave infrared using multiplexed metal structures," *Optics letters*, vol. 37, no. 3, pp. 371–373, 2012.

[42] J. Wang, Y. Chen, J. Hao, M. Yan, and M. Qiu, "Shape-dependent absorption characteristics of three-layered metamaterial absorbers at near-infrared," *Journal of Applied Physics*, vol. 109, no. 7, p. 074510, 2011.

[43] J. Nath, D. Panjwani, M. Yesiltas, C. Hirschmugl, F. Rezaie, and R. E. Peale, "Synchrotron infra-red spectral microscopy of metal-dielectric-metal cavity metamaterial absorbers," *Proc. SPIE*, vol. OP101-57, 2015.

[44] H. Tao, C. Bingham, A. Strikwerda, D. Pilon, D. Shrekenhamer, N. Landy, K. Fan, X. Zhang, W. Padilla, and R. Averitt, "Highly flexible wide angle of incidence terahertz metamaterial absorber: Design, fabrication, and characterization," *physical review B*, vol. 78, no. 24, p. 241103, 2008.

[45] H. Li, L. H. Yuan, B. Zhou, X. P. Shen, Q. Cheng, and T. J. Cui, "Ultrathin multiband gigahertz metamaterial absorbers," *Journal of Applied Physics*, vol. 110, no. 1, p. 014909, 2011.

[46] L. Li, Y. Yang, and C. Liang, "A wide-angle polarization-insensitive ultra-thin metamaterial absorber with three resonant modes," *Journal of Applied Physics*, vol. 110, no. 6, p. 063702, 2011.

[47] P. W. Kruse *et al.*, *Uncooled thermal imaging: Arrays, systems, and applications*, vol. 2003. SPIE press Bellingham, WA, 2001.

[48] E. Smith, J. Boroumand, I. Rezadad, P. Figueiredo, J. Nath, D. Panjwani, R. Peale, and O. Edwards, "Mems clocking-cantilever thermal detector," in *SPIE Defense, Security, and Sensing*, pp. 87043B–87043B, International Society for Optics and Photonics, 2013.

[49] A. R. Jha, *Infrared technology: applications to electro-optics, photonic devices, and sensors*, vol. 125. Wiley-Interscience, 2000.

[50] J. Hao, J. Wang, X. Liu, W. J. Padilla, L. Zhou, and M. Qiu, "High performance optical absorber based on a plasmonic metamaterial," *Applied Physics Letters*, vol. 96, no. 25, p. 251104, 2010.

[51] H.-T. Chen, "Interference theory of metamaterial perfect absorbers," *Optics express*, vol. 20, no. 7, pp. 7165–7172, 2012.

[52] X.-Y. Peng, B. Wang, S. Lai, D. H. Zhang, and J.-H. Teng, "Ultrathin multi-band planar metamaterial absorber based on standing wave resonances," *Optics express*, vol. 20, no. 25, pp. 27756–27765, 2012.

[53] J. C. M. Garnett, "Colours in metal glasses and in metallic films," *Philos. Trans. R. Soc. London Ser*, vol. A, no. 203, pp. 385–420, 1904.

[54] D. Bruggeman, "Dielectric constant and conductivity of mixtures of isotropic materials," *Ann. Phys.(Leipzig)*, vol. 24, pp. 636–679, 1935.

[55] X. Zeng, D. Bergman, P. Hui, and D. Stroud, "Effective-medium theory for weakly nonlinear composites," *Physical Review B*, vol. 38, no. 15, p. 10970, 1988.

[56] D. Prot, D. Stout, J. Lafait, N. Pinçon, B. Palpant, and S. Debrus, "Local electric field enhancements and large third-order optical nonlinearity in nanocomposite materials," *Journal of Optics A: Pure and Applied Optics*, vol. 4, no. 5, p. S99, 2002.

[57] N. Landy, C. Bingham, T. Tyler, N. Jokerst, D. Smith, and W. Padilla, "Design, theory, and measurement of a polarization-insensitive absorber for terahertz imaging," *physical review B*, vol. 79, no. 12, p. 125104, 2009.

[58] Y. Ma, Q. Chen, J. Grant, S. C. Saha, A. Khalid, and D. R. Cumming, "A terahertz polarization insensitive dual band metamaterial absorber," *Optics letters*, vol. 36, no. 6, pp. 945–947, 2011.

[59] J. Grant, Y. Ma, S. Saha, A. Khalid, and D. R. Cumming, "Polarization insensitive, broadband terahertz metamaterial absorber," *Optics letters*, vol. 36, no. 17, pp. 3476–3478, 2011.

[60] Y. Q. Ye, Y. Jin, and S. He, "Omnidirectional, polarization-insensitive and broadband thin absorber in the terahertz regime," *JOSA B*, vol. 27, no. 3, pp. 498–504, 2010.

[61] M. P. Hokmabadi, D. S. Wilbert, P. Kung, and S. M. Kim, "Design and analysis of perfect terahertz metamaterial absorber by a novel dynamic circuit model," *Optics express*, vol. 21, no. 14, pp. 16455–16465, 2013.

[62] Q.-Y. Wen, H.-W. Zhang, Y.-S. Xie, Q.-H. Yang, and Y.-L. Liu, "Dual band terahertz metamaterial absorber: Design, fabrication, and characterization," *Applied Physics Letters*, vol. 95, no. 24, p. 241111, 2009.

[63] J. Nath, E. Smith, D. Maukonen, and R. E. Peale, "Optical salisbury screen with design-tunable resonant absorption bands," *Journal of Applied Physics*, vol. 115, p. 193103, 2014.

[64] K. S. Yee *et al.*, "Numerical solution of initial boundary value problems involving maxwells equations in isotropic media," *IEEE Trans. Antennas Propag*, vol. 14, no. 3, pp. 302–307, 1966.

[65] A. Taflove and S. C. Hagness, *Computational electrodynamics*. Artech house, 2005.

[66] R. M. Woodward, B. E. Cole, V. P. Wallace, R. J. Pye, D. D. Arnone, E. H. Linfield, and M. Pepper, "Terahertz pulse imaging in reflection geometry of human skin cancer and skin tissue," *Physics in medicine and biology*, vol. 47, no. 21, p. 3853, 2002.

[67] J. W. Waters, L. Froidevaux, R. S. Harwood, R. F. Jarnot, H. M. Pickett, W. G. Read, P. H. Siegel, R. E. Cofield, M. J. Filipiak, D. A. Flower, *et al.*, "The earth observing system microwave limb sounder (eos mls) on the aura satellite," *Geoscience and Remote Sensing, IEEE Transactions on*, vol. 44, no. 5, pp. 1075–1092, 2006.

[68] R. Appleby and H. B. Wallace, "Standoff detection of weapons and contraband in the 100 ghz to 1 thz region," *IEEE transactions on antennas and propagation*, vol. 55, no. 11, pp. 2944–2956, 2007.

[69] N. Nagai, M. Sumitomo, M. Imaizumi, and R. Fukasawa, "Characterization of electron- or proton-irradiated si space solar cells by thz spectroscopy," *Semiconductor science and technology*, vol. 21, no. 2, p. 201, 2006.

[70] M. Tonouchi, "Cutting-edge terahertz technology," *Nature photonics*, vol. 1, no. 2, pp. 97–105, 2007.

[71] G. Pilbratt, J. Riedinger, T. Passvogel, G. Crone, D. Doyle, U. Gageur, A. Heras, C. Jewell, L. Metcalfe, S. Ott, *et al.*, "Herschel space observatory-an esa facility for far-infrared and submillimetre astronomy," *Astronomy & Astrophysics*, vol. 518, p. L1, 2010.

[72] Q.-Y. Wen, Y.-S. Xie, H.-W. Zhang, Q.-H. Yang, Y.-X. Li, and Y.-L. Liu, "Transmission line model and fields analysis of metamaterial absorber in the terahertz band," *Optics express*, vol. 17, no. 22, pp. 20256–20265, 2009.

[73] T. W. Ebbesen, H. Lezec, H. Ghaemi, T. Thio, and P. Wolff, "Extraordinary optical transmission through sub-wavelength hole arrays," *Nature*, vol. 391, no. 6668, pp. 667–669, 1998.

[74] F. G. De Abajo, "Colloquium: Light scattering by particle and hole arrays," *Reviews of Modern Physics*, vol. 79, no. 4, p. 1267, 2007.

[75] B. Ung and Y. Sheng, "Optical surface waves over metallo-dielectric nanostructures: Sommerfeld integrals revisited," *Optics express*, vol. 16, no. 12, pp. 9073–9086, 2008.

[76] M. Maqsood, R. Mehfuz, and K. Chau, "High-throughput diffraction-assisted surface-plasmon-polariton coupling by a super-wavelength slit," *Optics express*, vol. 18, no. 21, pp. 21669–21677, 2010.

[77] G. L. Pollack and D. R. Stump, *Electromagnetism*. Addison-Wesley, 2002.

[78] R. Kitamura, L. Pilon, and M. Jonasz, "Optical constants of silica glass from extreme ultraviolet to far infrared at near room temperature," *Applied optics*, vol. 46, no. 33, pp. 8118–8133, 2007.

[79] P. B. Johnson and R.-W. Christy, "Optical constants of the noble metals," *Physical Review B*, vol. 6, no. 12, p. 4370, 1972.

[80] J.-P. Bérenger, "Perfectly matched layer (pml) for computational electromagnetics," *Synthesis Lectures on Computational Electromagnetics*, vol. 2, no. 1, pp. 1–117, 2007.

[81] A. Hessel and A. Oliner, "A new theory of woods anomalies on optical gratings," *Applied Optics*, vol. 4, no. 10, pp. 1275–1297, 1965.

[82] R. Peale, H. Saxena, W. Buchwald, G. Aizin, A. Muravjov, D. Veksler, N. Pala, X. Hu, R. Gaska, and M. Shur, "Grating-gate tunable plasmon absorption in inp and gan based hemts," in *SPIE Optical Engineering+ Applications*, pp. 74670Q–74670Q, International Society for Optics and Photonics, 2009.

[83] H. Saxena, R. Peale, and W. Buchwald, "Tunable two-dimensional plasmon resonances in an ingaas/inp high electron mobility transistor," *Journal of Applied Physics*, vol. 105, no. 11, p. 113101, 2009.

[84] N. N. Esfahani, C. J. Fredricksen, G. Medhi, R. Peale, J. W. Cleary, W. R. Buchwald, H. Saxena, and O. J. Edwards, "Plasmon resonance response to millimeter-waves of grating-gated ingaas/inp hemt," in *SPIE Defense, Security, and Sensing*, pp. 80230R–80230R, International Society for Optics and Photonics, 2011.

[85] N. N. Esfahani, R. Peale, W. Buchwald, C. Fredricksen, J. Hendrickson, and J. Cleary, "Millimeter-wave photoresponse due to excitation of two-dimensional plasmons in in-

gaas/inp high-electron-mobility transistors," *Journal of Applied Physics*, vol. 114, no. 3, p. 033105, 2013.

[86] K. Aydin, V. E. Ferry, R. M. Briggs, and H. A. Atwater, "Broadband polarization-independent resonant light absorption using ultrathin plasmonic super absorbers," *Nature communications*, vol. 2, p. 517, 2011.

[87] K. B. Alici, A. B. Turhan, C. M. Soukoulis, and E. Ozbay, "Optically thin composite resonant absorber at the near-infrared band: a polarization independent and spectrally broadband configuration," *Optics express*, vol. 19, no. 15, pp. 14260–14267, 2011.

[88] M. K. Hedayati, M. Javaherirahim, B. Mozooni, R. Abdelaziz, A. Tavassolizadeh, V. S. K. Chakravadhanula, V. Zaporojtchenko, T. Strunkus, F. Faupel, and M. Elbahri, "Design of a perfect black absorber at visible frequencies using plasmonic metamaterials," *Advanced Materials*, vol. 23, no. 45, pp. 5410–5414, 2011.

[89] L. D. Landau, J. Bell, M. Kearsley, L. Pitaevskii, E. Lifshitz, and J. Sykes, *Electrodynamics of continuous media*, vol. 8. elsevier, 1984.

[90] E. D. Palik, *Handbook of optical constants of solids*, vol. 3. Academic press, 1998.

[91] T. J. Collins *et al.*, "Imagej for microscopy," *Biotechniques*, vol. 43, no. 1 Suppl, pp. 25–30, 2007.

[92] R. E. Peale, O. Lopatiuk, J. Cleary, S. Santos, J. Henderson, D. Clark, L. Chernyak, T. A. Winningham, E. D. Barco, H. Heinrich, *et al.*, "Propagation of high-frequency surface plasmons on gold," *JOSA B*, vol. 25, no. 10, pp. 1708–1713, 2008.

[93] M. Yan, J. Dai, and M. Qiu, "Lithography-free broadband visible light absorber based on a mono-layer of gold nanoparticles," *Journal of Optics*, vol. 16, no. 2, p. 025002, 2014.

[94] Y. Zhang, T. Wei, W. Dong, K. Zhang, Y. Sun, X. Chen, and N. Dai, "Vapor-deposited amorphous metamaterials as visible near-perfect absorbers with random non-prefabricated metal nanoparticles," *Scientific reports*, vol. 4, 2014.

[95] J. Nath, D. Panjwani, R. Peale, J. Musgraves, P. Wachtel, and J. McKinley, "Chalcogenide glass thin-film optics for infrared applications," in *SPIE Defense+ Security*, pp. 908507–908507, International Society for Optics and Photonics, 2014.

[96] J. W. Cleary, R. Soref, and J. R. Hendrickson, "Long-wave infrared tunable thin-film perfect absorber utilizing highly doped silicon-on-sapphire," *Optics express*, vol. 21, no. 16, pp. 19363–19374, 2013.

[97] M. A. Kats, D. Sharma, J. Lin, P. Genevet, R. Blanchard, Z. Yang, M. M. Qazilbash, D. Basov, S. Ramanathan, and F. Capasso, "Ultra-thin perfect absorber employing a tunable phase change material," *Applied Physics Letters*, vol. 101, no. 22, p. 221101, 2012.

[98] W. Streyer, S. Law, G. Rooney, T. Jacobs, and D. Wasserman, "Strong absorption and selective emission from engineered metals with dielectric coatings," *Optics express*, vol. 21, no. 7, pp. 9113–9122, 2013.

[99] L. L. Gordley, B. T. Marshall, and D. A. Chu, "Linepak: Algorithms for modeling spectral transmittance and radiance," *Journal of Quantitative Spectroscopy and Radiative Transfer*, vol. 52, no. 5, pp. 563–580, 1994.

[100] L. S. Rothman, D. Jacquemart, A. Barbe, D. C. Benner, M. Birk, L. Brown, M. Carleer, C. Chackerian, K. Chance, L. e. a. Coudert, *et al.*, "The hitran 2004 molecular spectroscopic database," *Journal of Quantitative Spectroscopy and Radiative Transfer*, vol. 96, no. 2, pp. 139–204, 2005.

[101] P. Loubere, "The global climate system," *Nature Education Knowledge*, vol. 3, no. 10, p. 24, 2012.

[102] M. J. Nasse, M. J. Walsh, E. C. Mattson, R. Reininger, A. Kajdacsy-Balla, V. Macias, R. Bhargava, and C. J. Hirschmugl, "High-resolution fourier-transform infrared chemical imaging with multiple synchrotron beams," *Nature methods*, vol. 8, no. 5, pp. 413–416, 2011.

[103] M. J. Nasse, B. Bellehumeur, S. Ratti, C. Olivieri, D. Buschke, J. Squirrell, K. Eliceiri, B. Ogle, C. S. Patterson, M. Giordano, *et al.*, "Opportunities for multiple-beam synchrotron-based mid-infrared imaging at ireni," *Vibrational Spectroscopy*, vol. 60, pp. 10–15, 2012.

[104] V. I. Veksler, "A new method of acceleration of relativistic particles," *J. Phys.*, vol. 9, pp. 153–158, 1945.

[105] Z. Li, E. A. Henriksen, Z. Jiang, Z. Hao, M. C. Martin, P. Kim, H. Stormer, and D. N. Basov, "Dirac charge dynamics in graphene by infrared spectroscopy," *Nature Physics*, vol. 4, no. 7, pp. 532–535, 2008.

[106] D. L. Wetzel and S. M. LeVine, "Imaging molecular chemistry with infrared microscopy," *Science*, vol. 285, no. 5431, pp. 1224–1225, 1999.

[107] L. M. Miller and R. J. Smith, "Synchrotrons versus globars, point-detectors versus focal plane arrays: Selecting the best source and detector for specific infrared microspectroscopy and imaging applications," *Vibrational spectroscopy*, vol. 38, no. 1, pp. 237–240, 2005.

[108] M. Yesiltas, Y. Kebukawa, R. E. Peale, E. Mattson, C. J. Hirschmugl, and P. Jenniskens, "Infrared imaging spectroscopy with micron resolution of sutter's mill meteorite grains," *Meteoritics & Planetary Science*, vol. 49, no. 11, pp. 2027–2037, 2014.

[109] M. Yesiltas, J. Sedlmair, C. Hirschmugl, and R. Peale, "Three dimensional ftir spectro-microtomography of carbonaceous chondrites," in *Lunar and Planetary Science Conference*, vol. 46, p. 1445, 2015.

[110] J. P. Pezacki, J. A. Blake, D. C. Danielson, D. C. Kennedy, R. K. Lyn, and R. Singaravelu, "Chemical contrast for imaging living systems: molecular vibrations drive cars microscopy," *Nature chemical biology*, vol. 7, no. 3, pp. 137–145, 2011.

[111] A. Lipson, S. G. Lipson, and H. Lipson, *Optical physics*. Cambridge University Press, 2010.

[112] J. J. Cargille, "Immersion oil and the microscope," 2008.